SYNTHESIS AND GAS SENSING PROPERTIES OF SINGLE CRYSTALLINE METAL-OXIDE NANOSTRUCTURES

Sergio Roso Casares

ADVERTIMENT. L'accés als continguts d'aquesta tesi doctoral i la seva utilització ha de respectar els drets de la persona autora. Pot ser utilitzada per a consulta o estudi personal, així com en activitats o materials d'investigació i docència en els termes establerts a l'art. 32 del Text Refós de la Llei de Propietat Intel·lectual (RDL 1/1996). Per altres utilitzacions es requereix l'autorització prèvia i expressa de la persona autora. En qualsevol cas, en la utilització dels seus continguts caldrà indicar de forma clara el nom i cognoms de la persona autora i el títol de la tesi doctoral. No s'autoritza la seva reproducció o altres formes d'explotació efectuades amb finalitats de lucre ni la seva comunicació pública des d'un lloc aliè al servei TDX. Tampoc s'autoritza la presentació del seu contingut en una finestra o marc aliè a TDX (framing). Aquesta reserva de drets afecta tant als continguts de la tesi com als seus resums i índexs.

ADVERTENCIA. El acceso a los contenidos de esta tesis doctoral y su utilización debe respetar los derechos de la persona autora. Puede ser utilizada para consulta o estudio personal, así como en actividades o materiales de investigación y docencia en los términos establecidos en el art. 32 del Texto Refundido de la Ley de Propiedad Intelectual (RDL 1/1996). Para otros usos se requiere la autorización previa y expresa de la persona autora. En cualquier caso, en la utilización de sus contenidos se deberá indicar de forma clara el nombre y apellidos de la persona autora y el título de la tesis doctoral. No se autoriza su reproducción u otras formas de explotación efectuadas con fines lucrativos ni su comunicación pública desde un sitio ajeno al servicio TDR. Tampoco se autoriza la presentación de su contenido en una ventana o marco ajeno a TDR (framing). Esta reserva de derechos afecta tanto al contenido de la tesis como a sus resúmenes e índices.

WARNING. Access to the contents of this doctoral thesis and its use must respect the rights of the author. It can be used for reference or private study, as well as research and learning activities or materials in the terms established by the 32nd article of the Spanish Consolidated Copyright Act (RDL 1/1996). Express and previous authorization of the author is required for any other uses. In any case, when using its content, full name of the author and title of the thesis must be clearly indicated. Reproduction or other forms of for profit use or public communication from outside TDX service is not allowed. Presentation of its content in a window or frame external to TDX (framing) is not authorized either. These rights affect both the content of the thesis and its abstracts and indexes.

UNIVERSITAT ROVIRA i VIRGILI

Synthesis and Gas Sensing Properties of Single Crystalline Metal-Oxide Nanostructures

Sergio Roso Casares

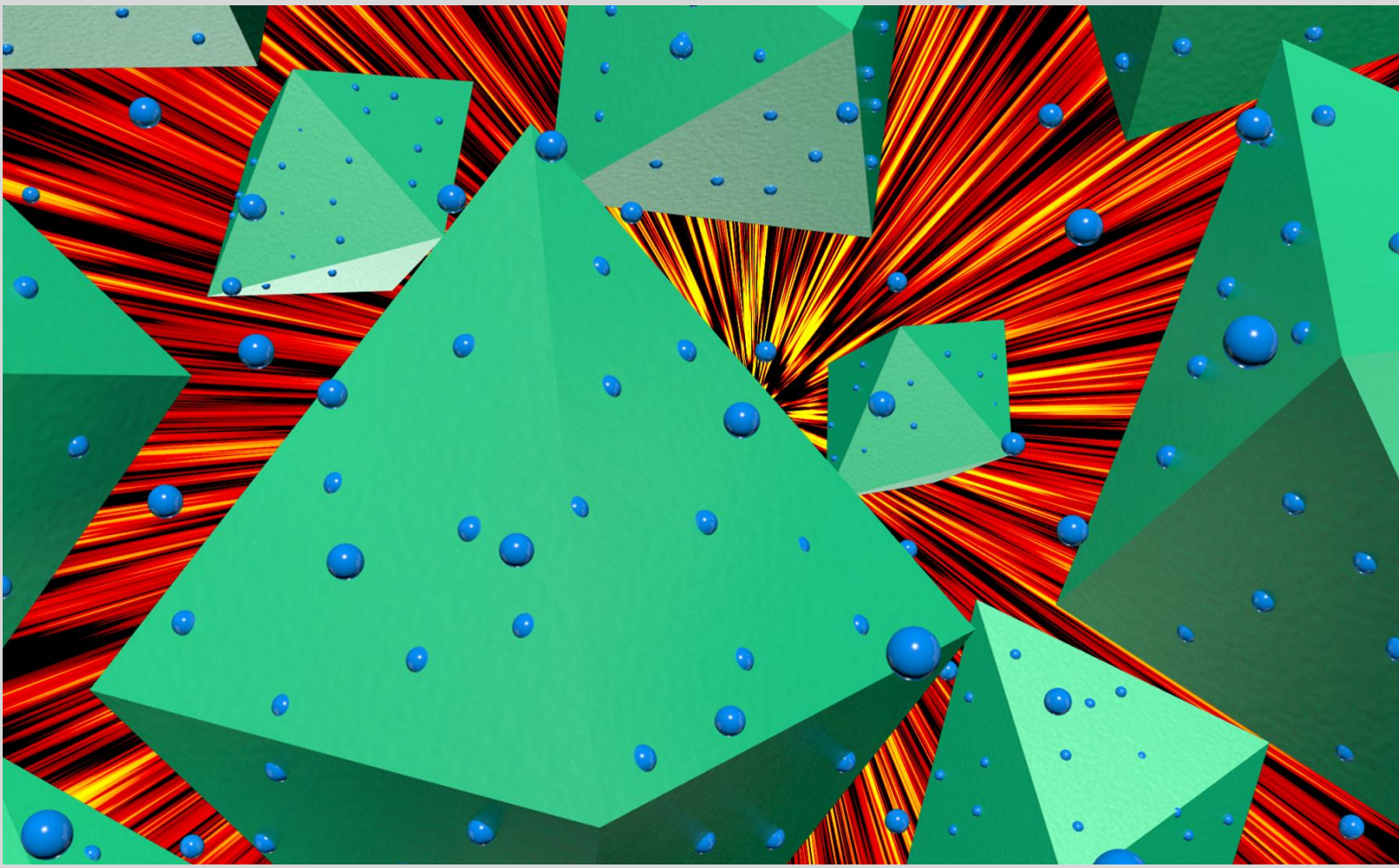

Doctoral Thesis

2017

UNIVERSITAT ROVIRA I VIRGILI
SYNTHESIS AND GAS SENSING PROPERTIES OF SINGLE CRYSTALLINE METAL-OXIDE NANOSTRUCTURES
Sergio Roso Casares

UNIVERSITAT ROVIRA I VIRGILI
SYNTHESIS AND GAS SENSING PROPERTIES OF SINGLE CRYSTALLINE METAL-OXIDE NANOSTRUCTURES
Sergio Roso Casares

UNIVERSITAT ROVIRA I VIRGILI
SYNTHESIS AND GAS SENSING PROPERTIES OF SINGLE CRYSTALLINE METAL-OXIDE NANOSTRUCTURES
Sergio Roso Casares

DOCTORAL THESIS

Synthesis and Gas Sensing Properties of Single Crystalline Metal-Oxide Nanostructures

Sergio Roso Casares

Supervised by:

Prof. Eduard Llobet Valero

Prof. Atsushi Urakawa

UNIVERSITAT ROVIRA I VIRGILI

Tarragona

2017

UNIVERSITAT ROVIRA I VIRGILI
SYNTHESIS AND GAS SENSING PROPERTIES OF SINGLE CRYSTALLINE METAL-OXIDE NANOSTRUCTURES
Sergio Roso Casares

UNIVERSITAT ROVIRA I VIRGILI

FAIG CONSTAR que aquest treball, titulat "Synthesis and gas sensing properties of single crystalline metal-oxide nanostructures", que presenta Sergio Roso Casares per a l'obtenció del títol de Doctor, ha estat realitzat sota la meva direcció al Departament d'Enginyeria Electrònica, Elèctrica i Automàtica d'aquesta universitat.

HAGO CONSTAR que el presente trabajo, titulado "Synthesis and gas sensing properties of single crystalline metal-oxide nanostructures", que presenta Sergio Roso Casares, ha sido realizado bajo mi dirección en el Departamento de Ingeniería Electrónica, Eléctrica y Automática de esta universidad.

I STATE that the present study, entitled "Synthesis and gas sensing properties of single crystalline metal-oxide nanostructures", presented by Sergio Roso Casares for the award of the degree of Doctor, has been carried out under our supervision at the Universitat Rovira i Virgili and at the Institute of Chemical Research of Catalonia.

Tarragona, 19th January, 2017

El/s director/s de la tesi doctoral

El/los director/es de la tesis doctoral

Doctoral thesis supervisor/s

Eduard Llobet Valero

Atsushi Urakawa

UNIVERSITAT ROVIRA I VIRGILI
SYNTHESIS AND GAS SENSING PROPERTIES OF SINGLE CRYSTALLINE METAL-OXIDE NANOSTRUCTURES
Sergio Roso Casares

Acknowledgements

First of all, I would like to express my sincere gratitude and appreciation to my supervisors Prof. Eduard Llobet Valero and Prof. Atsushi Urakawa for giving me the opportunity to make my doctoral thesis in their respective research groups. Also, I am deeply grateful for their excellent guidance and support in this entire journey. The realization of this thesis would not have been possible without their respective knowledge and collaboration. Thank you for your invaluable help and motivation during the scientific discussions and also for giving me the opportunity to enrich my scientific and communication skills by sending me to several national and international conferences.

I would also like to thank Universitat Rovira i Virgili and Institute of Chemical Research of Catalonia (ICIQ) for the economic support.

Additonally, I would like to thank Prof. Nicolae Barsan and Eberhard Karls University of Tübingen (Germany) for allowing me to spend three wonderful months in their laboratory and helping me achieving the last results of my thesis.

Because a doctoral thesis cannot be performed without the appropriate technical support I would like to thank mechanical workshops of Universitat Rovira i Virgili (Ernest Arce) and ICIQ (José Luis León) as well as, the glass workshop from ICIQ (Xavi Asensio) and Serveis the Resursos Científics i Tècnics from Universitat Rovira i Virgili (Lukasz, Marianna, Mercé, Rita...) for their patience, encouragement and support.

I would like to give my special thanks to Dr. Raúl Calavia for his unconditional support and encouragement during these years. Without your help we would not have gone that far. I really enjoyed our crazy scientific (and also not so

scientific) discussions in order to solve the different problems and also the different point of views (physicist-engineer) of several things.

Furthermore, a doctoral thesis cannot be completed without the support of the different group members. It is difficult to imagine having spent a better time with the company of all the lab members. So, I sincerely thank Minos group members (and also former members) Pierrick, Miriam, Eric, Tesfalem, Giovanni, Juán, Oriol, Fatima, Ariadna, Marc and Angel. I really enjoyed spending all these munchkin and citadel games we played together with all the friendly arguments that came as a result. Also, I would like to deeply thank ICIQ group members Jordi, Marta, Dragos, Juanjo, Rohit, Atul, Ling-jun, Shunsaku, Andrea, Damien, Rui Tsuyoshi, Murli, Antonio, Dina and Yi for making my time at ICIQ as comfortable as possible. However, now that I think about it, it was me who brought joy and happiness to the group, right?

Also thanks to Annie Green for coming to class on Saturdays for her English lessons

Por último, pero no por ello menos importante, me gustaría dar las gracias a mis padres Manuel y Mª del Pilar por el apoyo y el cariño brindado siempre, pero en especial estos años de doctorado. Se me hace muy difícil expresar con tan pocas palabras el amor y la admiración que siento hacia vosotros. Simplemente, gracias.

UNIVERSITAT ROVIRA I VIRGILI
SYNTHESIS AND GAS SENSING PROPERTIES OF SINGLE CRYSTALLINE METAL-OXIDE NANOSTRUCTURES
Sergio Roso Casares

UNIVERSITAT ROVIRA I VIRGILI
SYNTHESIS AND GAS SENSING PROPERTIES OF SINGLE CRYSTALLINE METAL-OXIDE NANOSTRUCTURES
Sergio Roso Casares

Table of Contents

UNIVERSITAT ROVIRA I VIRGILI
SYNTHESIS AND GAS SENSING PROPERTIES OF SINGLE CRYSTALLINE METAL-OXIDE NANOSTRUCTURES
Sergio Roso Casares

UNIVERSITAT ROVIRA I VIRGILI
SYNTHESIS AND GAS SENSING PROPERTIES OF SINGLE CRYSTALLINE METAL-OXIDE NANOSTRUCTURES
Sergio Roso Casares

CHAPTER 1

General Introduction

1.1 Nitrogen Dioxide and its Effects

It goes without saying that nowadays the detection of hazardous chemical species and gases is of paramount importance. Even though the rapid development of the industrial processes (petro chemistry, aeronautical, transport and so forth) has brought great benefits to humanity, they have also had unwanted effects such as negative influence on human health and the deterioration of the environment due to the release of toxic and pollutant gases to the atmosphere. Among them, nitrogen dioxide (NO_2) is one of the most relevant agents as it is recognized both for its high toxicity and its effects on the planet's environment.

Nitrogen dioxide is a paramagnetic, bent molecule with C_{2v} point group symmetry. It is a reddish-brown gas at room temperature and atmospheric pressure with a pungent, acrid odour. Unlike ozone, the ground electronic state of NO_2 is a doublet state, since nitrogen has one unpaired electron and it is a free radical, so the formula is often written as $^{\cdot}NO_2$.

Although NO_2 can be introduced into the environment by natural causes i. e. entry from the stratosphere, volcanoes, bacterial respiration and lightning to mention but a few, their main presence in the atmosphere is due to motor vehicle exhaust, combustion processes of carbon, petroleum and natural gas, as well as industrial treatments (i. e. arc welding, electroplating and metal etching). It is also produced commercially in making nitric acid react with metals and it is used in industrial production of lacquers, inks and several other chemical products. Finally, it is an essential component in rocket fuels, in the nitrification of chemical compounds and in the production of explosives.

As a consequence, general population is exposed to NO_2 mainly by breathing it in the air, especially people who live near combustion sources, power plants and highly congested high roads. Effects of NO_2 exposure on human health are focused on the respiratory tract. Prolonged exposure to NO_2 gas can damage the pulmonary parenchyma. Additionally, it determines the inhibition of the immunologic response of the lungs, dangerously increasing the probability of lung infection. It is also particularly hazardous against asthmatic people.

Exposure to low levels of NO_2 concentration can also irritate eyes, nose, throat, lungs and can possibly cause coughing. However, exposure to high levels of can cause burns, spasms and it can reduce the oxygenation of the tissues causing the accumulation of liquids in the lungs and ultimately, death.

For this reason, the European Commission as well as the World Health Organisation (WHO) has elaborated an extensive body of legislation which establishes health base standards and objectives for a number of pollutants in the air such as NO_2. According to the Directive 2008/50/EC of the European Parliament and the Council of May 2008, the limit value for one hour average exposure to NO_2 is 200 $\mu g \cdot m^{-3}$ (not to be exceeded more than 18 times per year) and the limit value for the annual average exposure to 40 $\mu g \cdot m^{-3}$.

1.2 Current Techniques for NO_2 Detection

Due to all these harmful effects over human health, there is a strong and industry-driven need to successfully and precisely detect NO_2 gas both at low and high concentrations. Until now, the methodologies used for the detection of

this gas consist of two main techniques: chemiluminiscence and optical absorption. The former, involves the emission of light due to a chemical reaction. In case of NO_2 detection, NO_2 gas is reduced to NO by means of a heated catalyst, usually Mo [eq. 1], followed by a gas-phase reaction with O_3 [eq. 2] forming an electronic active NO_2 molecule that emits light, which is proportional to the NO concentration [eq. 3].

$$Mo + 3NO_2 \rightarrow MoO_3 + 3NO \quad \text{(Eq.1)}$$

$$NO + O_3 \rightarrow NO_2^* + O_2 \quad \text{(Eq.2)}$$

$$NO_2^* \rightarrow NO_2 + \not{h} \quad \text{(Eq.3)}$$

On the other hand, traces of NO_2 can also be detected via Differential Optical Absorption Spectroscopy (DOAS). This technique is based on the Beer's law, which gives the change in the intensity of a beam of radiation as it travels through a medium that is not emitting light

$$I = I_0 exp\left(\sum_i \int \rho_i \beta_i ds\right)$$

where I is the intensity of the radiation, ρ is the density of the substance, β is the absorption and scattering cross section and s is the path.

There are two types of DOAS measurements: passive and active ones. While the active DOAS system uses their own light source, the passive ones use the sun as a light source.

A great amount of species can be detected with the methods stated before,even at low concentrations, however, they are bulky and they do not

allow the implementation of continuous monitoring. Additionally, they require very sophisticated set-ups, which make them very expensive and require skilled and knowledgeable operators.

For this reason, and also because of the need of monitoring air quality not only outdoors but also inside of buildings, solid state gas sensors based on semiconductor oxide materials i.e. SnO_2, ZnO, WO_3, In_2O_3 and so forth, have attracted the attention of researchers all around the world. Devices based on these materials have been used in several applications such as domestic gas alarms, air quality monitoring devices, food quality control, etc. Their enhanced sensitivity and reliability towards the detection of several target gases, their relatively low cost and their good reproducibility make of these materials perfect candidates for the new generation of devices capable of substituting the current technology on the environment monitoring field.

Furthermore, with the development of nanotechnology, new and interesting advantages for gas sensing applications arise. The ever-decreasing size of metal oxide semiconductors has led to the production of better controlled morphologies, single crystal structures and pure chemical compositions. The large surface to volume ratio of nanostructures, which provides more surface area for chemical and physical interactions to take place, give new devices an enhanced sensitivity, with respect to their bulk counterparts, as well as low energy consumption and a fast response/recovery time. Additionally, they possess quantum confinement effects, which have a high impact on the electronic charge transfer and band structure and can also enhance the gas sensing properties.

However, nanostructured gas sensors also possess important drawbacks, for instance their low selectivity, yet this can be overcome by functionalizing the nanostructured semiconductor with metal nanoparticles that will act as catalyst, enhancing the sensitivity towards the desired target gas and eventually, enhancing the selectivity of the sensor depending on the size and density of the nanoparticles.

With this purpose on the horizon, the elaboration of this doctoral thesis is focused on the development of nanostructured semiconductor oxide materials with a characteristic morphology by means of facile and reproducible techniques for the selective detection of very low concentrations (tens of ppb) of nitrogen dioxide gas. Furthermore a full and accurate characterization of the physical, chemical and electronic properties will be carried out with the help of techniques such as ESEM, TEM, HRTEM, XRD, XPS and DRIFT spectroscopy to mention but a few.

Finally, the organization of the doctoral thesis is as follows:

- This chapter has given the reader an overview of the main motivation for realising the thesis and its objectives.
- Chapter 2 makes a general review of the state-of-the-art of the nanostructured semiconductor metal oxide gas sensors over the past few years. It will contain the main principles and characteristics of metal oxide gas sensors followed by the latest advances in the synthesis of single crystal ZnO and In_2O_3 nanostructures. Finally, it will review the gas sensing properties of such nanostructures focusing on the selective detection of gases like NO_2.
- Chapter 3, at first, will explain the different reactors used for the fabrication of the ZnO and In_2O_3 nanostructures, which were employed by the sensors developed in this thesis. This chapter includes a study for the

design and fabrication of the test chamber used in the characterisation of gas sensing properties.

- Chapter 4 will review the synthesis and deposition of the different active layers. A physical, chemical and electronic characterization of the different samples used in the thesis will be made.
- Chapter 5 will focus on the gas sensing properties of the different samples
- Chapter 6 will focus on the in-situ *operando* spectroscopy analysis of gas sensors.
- Chapter 7 contains the conclusions derived from this thesis and some suggestion for future work.

CHAPTER 2

State of the art

In this chapter, the current technology of semiconductor metal oxide gas sensors will be reviewed. Furthermore, we will show how to improve their sensitivity and selectivity by means of nanostructuring the active layer.

2.1 Solid State Gas Sensors

It can be said, that a generic chemical gas sensor is composed by an active sensitive layer which is in contact with the chemical or biological substance to be detected. Then, a transducer converts such interaction into an electrical or optical signal that can be measured. Another important characteristic of solid state gas sensors is their reversibility, that is, after the interaction with the substance is over, the sensor returns to the initial state it had before the interaction took place.

In addition to the conductivity change of the sensing material, the transduction can also be performed by measuring other parameters such as the capacitance, mass, work function or energy released upon interaction. Moreover the sensitive layer can be made of organic (polymers and complexes) and inorganic materials (semiconductor metal oxides, electrolytes...).

For the purpose of this thesis, we will focus our attention on semiconductor metal oxide as a sensitive nanomaterial, functionalising the structures with metal nanoparticles.

2.1.1 Metal Oxide Gas Sensors. Working Principle

Semiconductor metal oxide gas sensors are commonly known as chemoresistive sensors. The main characteristic of these types of sensors is

that, when they are exposed to a certain chemical compound (in the gas phase), they undergo a change in their electrical resistance. The sensing properties of metal oxides were first published by Seiyama et al. Back in 1962[1]. They developed a new gas detector based on the fact that the absorption and desorption of certain gas species induced a rapid change in the electrical conductivity of the active layer (zinc oxide thin film). When the sensitive layer is exposed to a reducing or oxidizing species, the latter provides or returns electrons to the material respectively. As a consequence, the density of charge changes and a change in the electrical resistance is produced. Based on the type of charge carriers, semiconductor metal oxides can be divided into two groups: n-type semiconductors, in which electrons are the main carriers (SnO_2, ZnO, TiO_2, In_2O_3, WO3, VaO_2, and so forth) and p-type semiconductors, in which the major carriers are holes (NiO, TeO_2, and CuO)[2]. Until now, the most studied metal oxide for gas sensing applications is SnO_2, yet recently, other metal oxides such as ZnO, WO_3, In_2O_3 are gathering importance. In this thesis, we will focus on ZnO and In_2O_3, which are two of the most promising materials for enhanced sensitivity and selectivity among all others metal oxides.

The process of gas sensing by a semiconductor metal oxide involves two key functions: the receptor function and the transduction function as shown in figure 2-1.

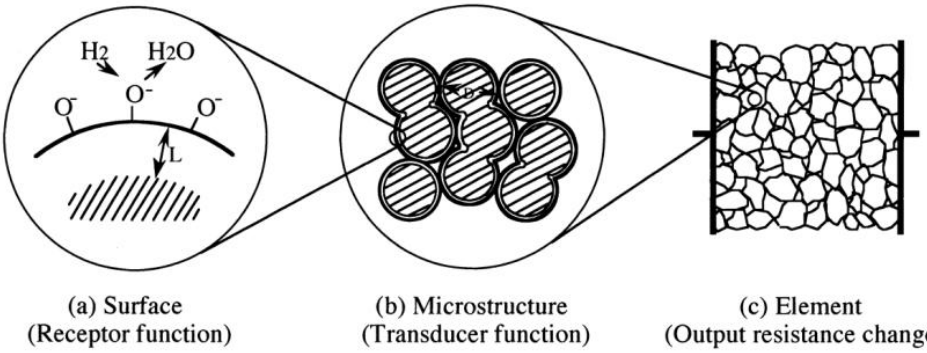

Figure 2-1: Schematic view of the receptor and transduction function[3]

The receptor function is the recognition of a certain target gas through a solid-gas interaction. Such interaction induces an electronic change in the oxide. When an oxidizing gas such as oxygen reaches the surface of the oxide, it interacts with the material, forming chemisorbed oxygen species such as O_2^-, O^- and O^{2-} and takes electrons from the conduction band of the material. The nature of the chemisorbed oxygen depends mainly on the temperature (eqs. 1-4), yet above 300ºC, the predominant oxygen species is lattice oxygen, that is, O^{2-}.

$$O_2(g) \rightarrow O_2(ads)$$
$$O_2(ads) + e^- \rightarrow O_2^-(ads) \qquad < 100℃$$
$$O_2^-(ads) + e^- \rightarrow 2O^-(ads) \qquad 100℃ < T < 300℃$$
$$O_2^- + e^- \rightarrow 2O^{2-}(lattice) \qquad > 300℃$$

This negatively charged oxygen ions adsorbed at the surface of the semiconductor oxide, generate a band bending, which generates a surface potential ($-eV_{surface}$), and a depletion layer that results in free electrons being confined in the centre of the grains as shown in figure 2-2. As a result, the electrical resistance of the material increases. Upon oxygen absorption, Shottky

barriers are formed in the boundaries of the grains that are in contact with each other, which depend on the concentration of oxygen adsorbates.

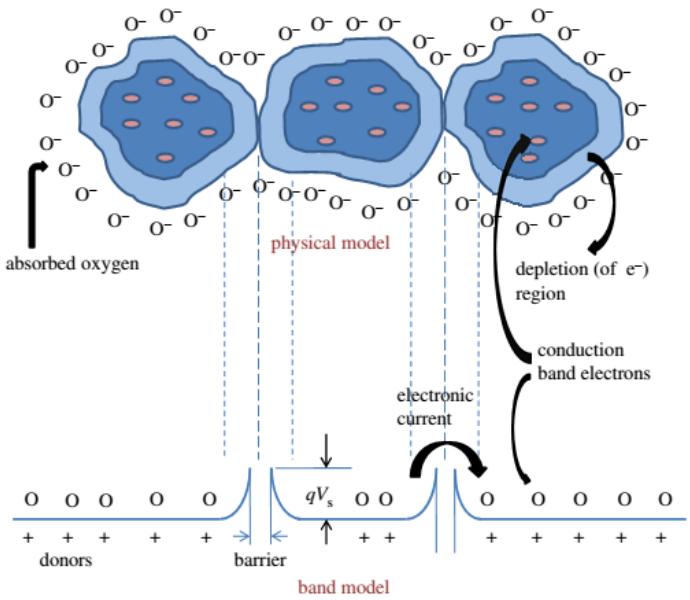

Figure 2-2: Band model for semiconductor metal oxide grains[4]

On the other hand, the transduction function involves the conversion of the surface phenomena into a measurable electrical signal, in case of a chemoresistive gas sensor, into a change in the conductivity (or resistance). In other words, changes in the width of the depletion layer induce changes in the electrical resistance. In the presence of a reducing gas, gas molecules react with chemisorbed oxygen at the surface, causing a reduction in the depletion layer and, as a result, a reduction of the electrical resistance[5]. For example, when CO reacts with chemisorbed oxygen on the metal oxide surface generating CO_2, the amount of adsorbed oxygen will decrease significantly and trapped electrons are released back to the oxide. As a result, the height of Shottky barriers is decreased, which produces an increase in the conductance (or decrease in the resistance) of the whole sensing layer.

Furthermore, there is a clear relation between the depletion layer width and the size of the metal oxide grains. It has been reported that the ratio between the grain size (D) and the Debye length (LD), which is the scale over which the charge separation happens in a semiconductor, greatly affects the magnitude of the resistance variation[6]. The Debye length is defined as follows:

$$L_D = \sqrt{\frac{\varepsilon k_B T}{q^2 N_D}}$$

where ε is the dielectric constant, kB is the Boltzmann constant, q is the elementary charge and Nd is the density of dopants (either donors or acceptors).

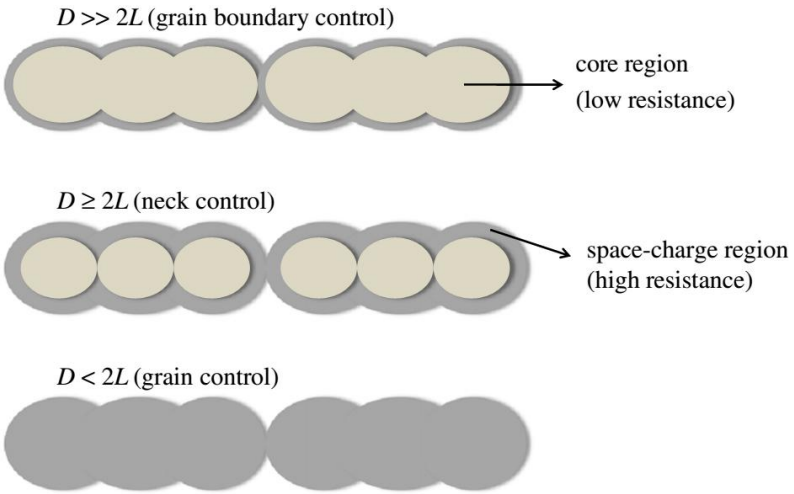

Figure 2-3: Schematic view of the grain boundary control, neck control and grain control[4].

If the grain size is larger than two times the Debye length ($D>>2L_D$), the depletion of the surface between the grain boundaries control the conductivity is really small (grain boundary control). In this case, a low response of the sensor is expected because only a small part of the semiconductor is affected by the analyte. When grain size is becoming comparable with the Debye length (but

still larger, $D \geq 2L_D$), the necks become more resistant and they start to control the gas sensitivity (neck control). Finally, when $D < 2L_D$, the whole grain is depleted, the energy bands are almost flat, changes in the oxygen concentration affects the entire semiconductor and thus, a high response is obtained[7] (grain control), as shown in figure 2-3.

2.1.2 Metal-loaded metal oxides. Working principle

As stated, catalytic oxidation of the target gas over the grain surface is responsible for the decreasing of the surface oxygen and, as a consequence, the decrease in the electrical resistance of the oxide. However, in some cases, the bare surface of the material is not active enough and the need for the deposition of foreign materials arises. Materials like platinum, palladium, gold, silver, and so on, are responsible for the enhancement of the sensitivity towards several target gases (particularly reducing gases and vapours). This effect of depositing noble metal particles over the pure metal oxide in order to enhance the sensitivity is called sensitization.

Normally, the addition of noble metal nanoparticles induces a shift of the optimum working conditions to the lower temperature side accompanied by a dramatic increase of the sensor response. In order to explain the sensitization process we will follow an example proposed by *Yamazoe et al*. [3] involving SnO_2 material decorated with Pd nanoparticles when exposed to H_2 target gas. Two types of interaction take place between the metal loading and the surface of the metal oxide: chemical and electronic sensitization.

The former involves gas molecules, in this case H_2 molecules, activated by the metal nanoparticles. The activated fragments (H) are spilt-over to the semiconductor and react with chemisorbed oxygen. This spillover effect can also be found with other metal catalysts such as Pt loaded on other oxides. In the latter the metal nanoparticle in the oxidized state act as a strong acceptor of electrons from the oxide, inducing a surface space charge layer which is strongly depletive. When the metal makes contact with the target gas, it reduces and the space charge layer is relaxed, giving back the electrons to the metal oxide. This induces a large increase in the response of the sensors decorated with noble metal nanoparticles[3]. A diagram of the chemical and electronic sensitization can be found in figure 2-4.

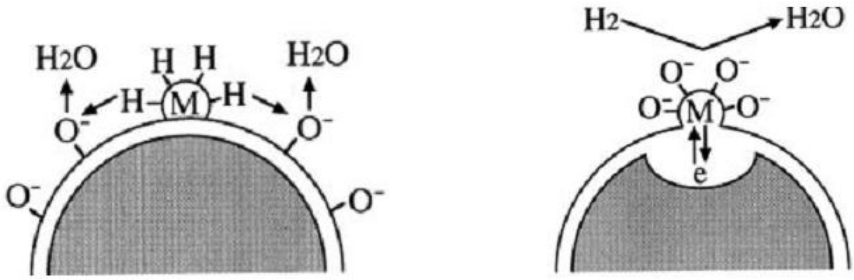

Figure 2-4: On the right, a schematic view of the chemical sensitization and on the left, a schematic view of the electronic sensitization

2.1.3 Characteristics of Metal Oxide Gas Sensors

For chemoresistive gas sensors, there are different parameters that can be useful in order to monitor output signal produced by the metal oxide. These parameters give us an idea of how good the performance of our device is:

- Resistance: it is one of the most important parameters because it is associated with the primary electrical property measured in order to analyze gases.
- Sensor response: it is defined as the change in the electrical resistance when an analyte makes contact with our metal oxide gas sensor when the sensor is at its equilibrium state. In other words, it is the ratio between the resistance of the sensor in air (R_{air}) and the resistance of the sensor after the introduction of the gas (R_{gas}). The sensor response can be calculated by different operations, however, in this thesis the sensor response will be expressed as follows:
  - $S = \frac{R_{air}}{R_{gas}}$ for reducing gases
  - $S = \frac{R_{gas}}{R_{air}}$ for oxidising gases
- Sensitivity: it is the partial derivative of the sensor response to the concentration. In other words, it is the change of the sensor response produced by the change in the concentration of the analyte. It can be obtained by calculating the slope of the calibration graph.
- Selectivity: it determines the ability of the sensor to respond to only a particular group of analytes or to even a single analyte.
- Response/recovery time: the response time is the time that the sensor takes to achieve a 90% of the total change of the resistance when exposed to a certain concentration of a target gas. The recovery time is defined as the time that the sensor takes to recover a 90% of the initial value of the resistance when exposed to clean air.

- Stability: it is defined as the ability of the sensor to maintain their properties in a long period of time. It has been reported that chemical surface reaction may produce a long-term drift (poisoning) affecting the performance of the sensor[8].
- Lower Detection Limit (LDL): it is the minimum possible concentration that a gas sensor can detect under certain conditions. It is determined by the sensitivity and the noise levels of the sensor. In gas sensor field, it is generally assumed that the limit of detection is reached when the sensor signal is three times higher than the level of noise.

It is important for gas sensors to have a high sensitivity in the area of interest as well as a good selectivity for the desired gases. Furthermore, short response and recovery times are usually needed in certain industrial applications. Also, long-term stability is required, as robust and good performing sensors would be highly demanded[9].

Apart from all these characteristics, there are other properties of the metal oxides that can make our gas sensors more sensitive, more selective or faster in their response and recovery, for instance the porosity. A highly porous material, the gas can diffuse into the material, increasing the effective surface area[10].

The thickness of the film is another important parameter if we want to improve the performance of the sensor, especially if the sensitive layer is compact. In this particular case, one can simulate the current flow as two resistances in parallel, one being equivalent to the geometric morphology of the layer and which will be affected by the gas interactions, and the other resistance which is fixed and corresponds to the bulk. The latter resistance is never affected by gas

reactions. Therefore, the thickness of the sensing layer greatly affects the sensitivity of the sensor[11].

Additionally, one last step to further improve the sensing performance of the layer is by decreasing the grain size of the semiconductor metal oxide, in other words, making a nanostructured film as a sensitive layer.

2.2 Nanostructured Gas Sensors

In the design of solid materials for gas sensing applications, the chemical environment of surface atoms is different from that of the bulk atoms. Basically, gas sensing properties are dominated by surface reactions, that is to say, surface chemistry.

In 1991 it was shown by Yamazoe that drastically reducing the crystallite size, one can dramatically enhance the sensor performance[12]. What is important is that baseline resistance of R_{air} and R_{gas} change dramatically just by a small variation in grain size d_g. When the size of the grains increases, it causes a gradual increase of both R_{air} and R_{gas}. The characteristic change in the behaviour at a critical grain size is associated with the formation of the electron depleted space charge layer, or Debye length. Because the space charge layer keeps constant, the proportion of space charge layer relatively changes when the particle size increases or decreases[3, 13]. As stated before, the critical grain size corresponds to a point where it becomes two times the Debye length ($d_m<2L_D$). As a result, the response of the sensor critically depends on the grain size of the metal oxide. Due to its reduced grain size, a

great surface-to-volume ratio can be achieved, which allows almost the whole material to be exposed to the environment.

With these characteristics, nanostructured gas sensors have been reported to have unique gas sensing properties like enhanced sensitivity due to the increased surface area, proper selectivity and reasonably fast response and recovery times[14].

One of the most common studied nanostructures are the so-called one dimensional (1-D) nanostructures such as nanowires, nanoneedles, nanotubes, nanofibers, nanobelts and so forth.

2.2.1 One Dimensional (1D) Nanostructures. Synthesis Methods

Nanostructures can be classified into different categories according to the number of dimensions they have at the nanometer scale: zero dimension for nanoparticles, one dimension for nanowire like structures and two dimension for films[15].

1D nanostructures possess several advantages with respect to thin and thick film layers due to their large surface-to-volume ratio, with a grain size similar in extension to the spacer charge layer and a high stability due to their high crystallinity.

Additionally, they can be fabricated with significant lengths that will provide a long semiconducting channel[16]. There has been a wide range of morphologies that have attracted the attention of researchers in the past years such as nanowires, nanotubes, nanorods and so on, being nanowires the most studied among them.

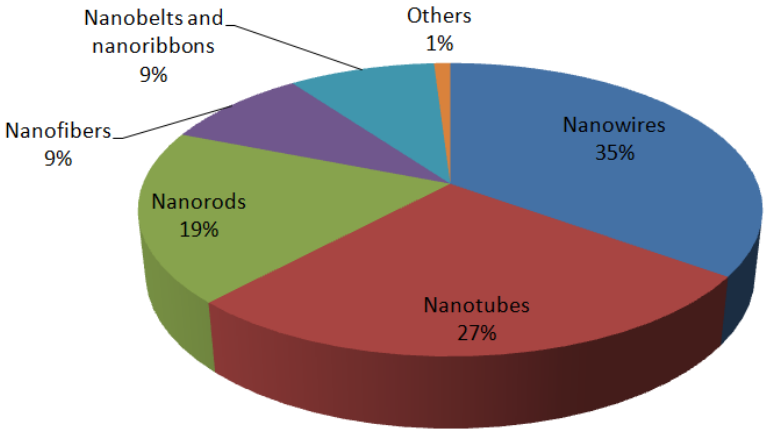

Figure 2-5: One-dimensional nanostructures based on morphology (source: Web of Knowledge)

In order to try to synthesize and develop these morphologies, one can follow several paths; we can divide them in two categories: the top-down and bottom-up techniques.

The former is based on micro fabrication with deposition, etching and ion beam milling on planar substrates in order to reduce the lateral dimensions of the film to the nanometer scale. It involves a wide range of techniques such as electron beam, X-ray lithography, focussed ion-beam to name but a few. Using top-down technology, highly ordered nanowires can be obtained, however they require elevated processing costs and preparation times[13].

The latter, consists of chemical synthesis by vapour phase transport, electrochemical deposition, solution-based techniques or template growth. It has the advantage that one can obtain high purity materials with high crystallinity, very small and controllable size and, last but not least, it has the possibility to decorate or dope the material with other metals or metal oxides for further enhancing the properties of a gas sensor.

Among all the bottom-up techniques, there is on that excels, that is chemical vapour deposition (CVD). CVD is a process where one or more volatile precursors are transported via vapour phase to a reaction chamber where they undergo a chemical reaction in a heated substrate. Generally, CVD consists of three main components: precursor supply system, CVD reactor and exhaust system[17].

The precursor system supply function is to generate precursors in the gas phase that are transported to the main reactor, usually, with the help of a carrier gas such as nitrogen or argon. Precursors can be either in solid or liquid form. There exist some variants methods which use liquid precursors like aerosol-assisted CVD that are used to produced novel doped materials or ternary/quaternary materials because of the ease in controlling the stochiometry of the liquid precursor[18].

The reactor chamber is where the deposition reaction begins. These reactions can be homogeneous or heterogeneous. In homogeneous reactions, absorption occurs first over the solid substrate and the reaction that generates the active layer takes place, while heterogeneous reactions occur between the gas species and a solid substrate. In this case, diffusion reactions of the precursor species occurs at an interfacial gas/solid boundary layer, forming nucleation sites on the substrate[17]. Subsequent reactions occur on the solid substrate to promote the formation of planar films or the desired nanostructures. All CVD techniques have several common steps[19]:

- Precursor, generation of active gaseous reactant species
- Transport, that is delivery of the vaporized precursors into the reaction chamber

- Adsorption of the precursor onto a hot surface
- Decomposition of the precursor
- Migration of atoms to a strong binding site
- Nucleation that leads to the growth of the thin film
- Desorption of unwanted products
- Removal of unwanted products

The choice of the precursor is of paramount importance. It has to be stable and during the gas phase transport it has to react only onto the heated substrate. Usually, the delivery phase is carried out with the help of an inert gas, generally argon or nitrogen. When the precursor reaches the heated substrate it undergoes a chemical reaction and the formation of the metal oxide takes place. After that, migration to stronger binding sites takes place. This is where the process changes from physisorption to chemisorption. Finally, the nucleation takes place and the formation of the nanostructure occurs.

For this reasons, CVD techniques present a wide range of advantages compared with other techniques, for example a single step fabrication of gas sensors which involves the synthesis and integration of the material in the sensor platform, production of atomically mixed homogeneous materials with very high reproducibility and the ability to influence crystal structure and morphology.

There are several growth mechanisms based on CVD technique depending on the presence or absence of a catalyst, solution-liquid precursors and so on.

2.2.1.1 Vapour-Liquid-Solid

The vapour-liquid-solid mechanism is a catalyst supported CVD. It was first proposed by Wagner and Ellis back in the 1960s for the formation of Si whiskers from silicon tetrachloride and silene[20]. They found a way to grow Si whiskers in a heated substrate covered with Au particles, and that the size of the whiskers could be determined by the size of such nanoparticles because the nanostructures tend to grow in the areas seeded by the metal catalyst. The metal catalyst can be added to the substrate by sputtering, thermal evaporation, laser ablation or agglomerate under elevate temperatures[21]. Typically, thin films of only a few nanometers are enough and at a suitable temperature, the film is expected to break into droplets that will allow the catalytic growth.

This technique involves the use of nano-size metal catalysts to form eutectic alloy-drops in order to be able to grow the oxide nanomaterial[22].

Mainly, the VLS growth process can be divided into three main steps:

1. Creation of a liquid alloy of the catalyst (typically Au) and the material to deposit,
2. Nucleation of the material in the solid-liquid interface, and
3. Growth of the nanostructure

As stated, metal clusters should change to liquid droplets for preferential absorption of vapour precursors and further nucleation of target materials. If the mixture of the vapour precursor and the metal clusters is a eutectic mixture, liquid alloy droplets form when temperature exceeds the eutectic point and thus, the melting temperature of the metal cluster is reduced[23]. As a consequence, the first step is to form the alloy between the target material and the metal

clusters. Then, precursors are easily adsorbed into the liquid droplets. Continued absorption of precursors increases the concentration of the desired materials into the liquid droplet until it reaches the supersaturation. When the concentration of the material exceeds a certain level, crystal nucleation starts at the solid-liquid interface and the growth of the nanostructure begins. Growth of the nanostructures is unidirectional because less energy is required for the nucleation at the liquid-solid interface. A schematic view of the VLS mechanism for nanowires is shown in figure 2-5.

As a result, one has to take into account several issues in order to successfully grow the desired material. For instance, a wise choice of the metal clusters and the target material is required in order to form the eutectic point which will allow forming the nanostructures. Another important characteristic of the target material is that it should have a low pressure vapour at the desired temperature[24].

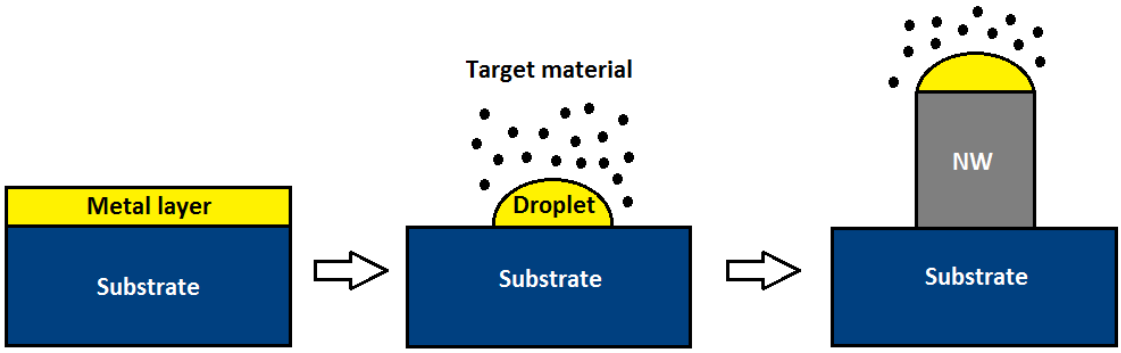

Figure 2-6: Schematic view of the VLS mechanism

Until now, VLS is one of the most powerful techniques to produce 1D nanostructures, particularly nanowires. A wide range of materials can be fabricated such as SnO_2, ZnO and In_2O_3 and so on.

However, there are other methods also suitable to grow 1D nanostructures.

2.2.1.2 Vapour-Solid

The vapour-solid method occurs when the nanostructure crystallization originates from the condensation from the vapour without the help of any catalyst. It has been proposed that the minimization of the surface energy governs the VS process[13]. Under high temperature conditions, source materials are vaporized and then directly condensed on the substrates places on a lower temperature region. Once the condensation is achieved, the condensed molecules form seed crystals that will act as nucleation sites. As a consequence, they facilitate directional growth of 1D nanostructures. There are three processes involved in the synthesis of 1D nanostructures by vapour-solid technique: i) thermal sublimation of from the hot metal filament, ii), chemical vapour reaction of the sublimated metal vapour with traces of oxygen in the reactor, and iii) condensation of the metal-oxide vapour into 1D nanostructures[24]. A schematic view of the vapour-solid mechanism can be observed in figure 2-6.

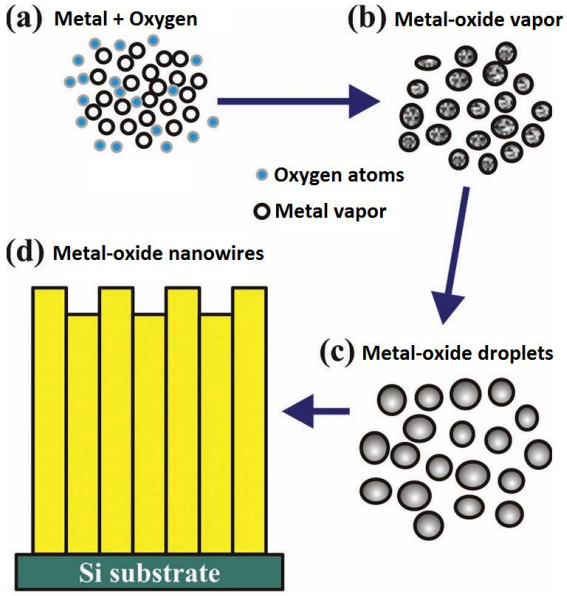

Figure 2-7: Schematic view of the vapor-solid mechanism (adapted from reference [22]).

2.2.1.3 Aerosol-Assisted CVD

Aerosol-assisted CVD usually employs temperatures that range between 350 and 600ºC, which make it suitable for producing metal-oxide nanostructures for gas sensing applications. It is also a very useful technique to functionalize metal oxide nanostructures with metal nanoparticles, which can greatly enhance the gas sensing properties of the device[25].

This technique possesses several advantages with respect with other techniques such as flexibility for deposition different metal-oxide nanoparticles[26], high deposition rate and improvements for precursor selection.

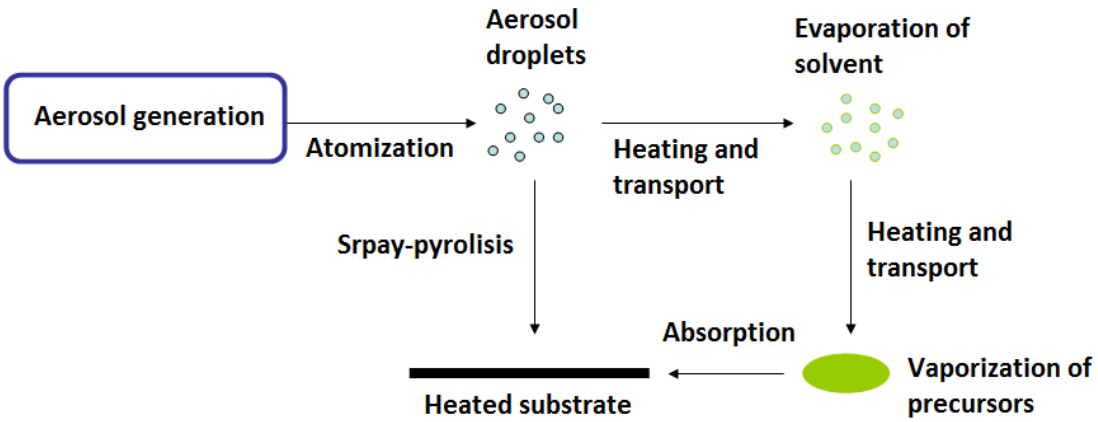

Figure 2-8: Schematic view of the working principles of the aerosol-assisted CVD method.

Aerosol-assisted CVD involves the atomization of a liquid precursor solution into sub-micrometer-sized aerosol droplets. Such droplets are transported into a heated reaction zone, where the solvent is evaporated at a certain temperature[27]. A schematic view of the aerosol-assisted CVD process is shown in figure 2-7.

After that, the precursor is transported to the heated substrate and it decomposes to form the desired product. If the precursor droplets reach the

heated substrate before the complete evaporation of the solvent, a spray-pyrolysis process will take place instead of a true CVD.

When the precursors reach the heated zone, two kind of reactions may take place: homogeneous and heterogeneous reactions. In case of heterogeneous reactions, decomposition of the vaporised precursor in gas phase followed by adsorption of these vapours onto the heated substrate. However, homogeneous reactions take place when the temperature is too high and thus, early decomposition and chemical reaction of the precursor takes place. As a result, homogeneous nucleation with fine particles are formed that can undergo heterogeneous reactions on the surface of the heated substrate.

One of the advantages of the aerosol-assisted CVD process is the choice of the precursor. It only has to be highly soluble and have low pressure vapour at room temperature.

2.3 Nanostructured Semiconductor Metal Oxide Materials for Gas Sensing Applications

A wide range of nanostructured metal oxides can be produced by means of these types of CVD techniques such as SnO_2 [28], ZnO[29], WO_3 [30], In_2O_3 [31] and so forth. These metal oxide materials can be of great interest for gas sensing applications due to their excellent electrical and optical properties.

2.3.1 Zinc Oxide

Zinc oxide is an inorganic compound with the formula ZnO. It is a wide band gap (around 3.37 eV at room temperature) n-type semiconductor of the II-VI

semiconductor group, and it possess an extremely large binding energy (60 meV), much higher than those of widely used metal oxide such as GaN (25 meV), which provides ZnO to have a very efficient excitonic emission at room temperature and higher. Also it has a large piezoelectric constant, which makes ZnO highly suitable to be used in sensors, transducers and actuators. Another important property of ZnO is its strong sensitivity of surface conductivity to the presence of adsorbed species, particularly gases. Additionally, ZnO has a strong luminescence in the white-green region of the spectrum. The n-type conductivity makes it appropriate also for applications in vacuum fluorescent displays and field emission displays[32].

Zinc oxide can be found in nature in two main different crystalline forms: cubic zincblende or hexagonal wurzite. Under ambient conditions, the thermodynamically stable phase is that of the wurzite, whereas the zincblende ZnO structure can only be found by growing the material onto cubic substrates.

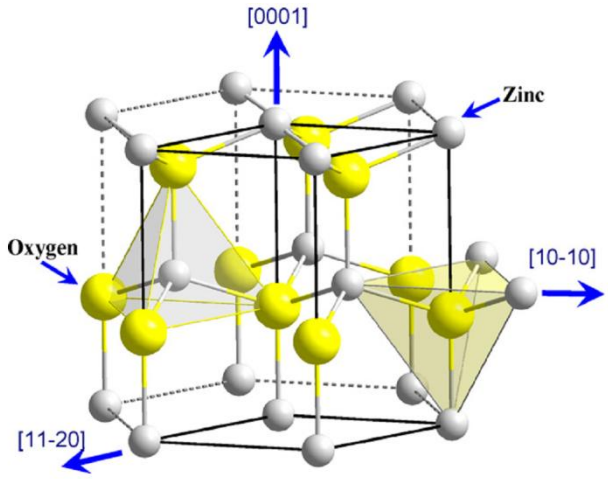

Figure 2-9: Wurzite crystalline structure of ZnO[33]

As shown in figure 2-8, ZnO wurzite has an hexagonal unit cell with two lattice parameters, *a* and *c* with a ratio of *c/a* = 1.633. The basal plane lattice

parameter, that is, the edge length of the basal plane hexagon, is named as *a,* and the axial lattice parameter perpendicular to the basal plane is depicted by *c*. Each sublattice includes four atoms per unit cell, and every atom of one kind (group II) is surrounded by four atoms of the other kind (group VI) and vice versa, which are coordinated in the form of a tetrahedron.

ZnO has three types of fast growth directions: <2 -1 -1 0>, <0 1 -1 0>, and ±[0001]. The ionic character of the material gives rise to a polar repeat unit along the c-axis. As a consequence of this symmetry, [0001] and –[0001] surfaces of the wurzite structure, exhibit different bulk terminations with the first one terminated in Zn-atoms and the latter by O-atoms. These are the most common crystal orientations of ZnO[34].

ZnO exhibits a wide range of morphologies by tuning the growth rates using these directions as observed in figure 2-9. One of the most profound factors determining the morphology involves the relative surface activities of various growth facets under given conditions.

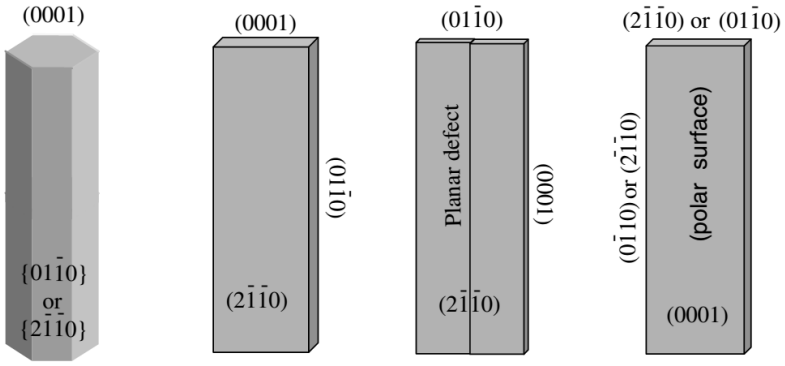

Figure 2-10: Typical growth morphologies of 1D ZnO nanostructures[33].

For these reasons, ZnO has attracted the attention for the past years as a great candidate for gas sensing applications. Among all morphologies that have

been studied, nanowires are the ones that have accumulated the highest number of publications. However, quantity and quality of 1D ZnO nanostructures vary from process to process.

Table 1 shows an overview of some of the recent advances of ZnO nanostructures for gas sensing applications.

Synthesis Method	Morphology	Features	Target Gas	Working Temperature	Response	Reference
CVD (VS)	Nanowires	-	Cl_2 (0.2-2 ppm)	150-400ºC	1.3-3.1	35
CVD (VLS)	Nanowires	-	H_2	Room Temperature	55%	36
CVD	Nanorods	-	H_2 (500 ppm)	320ºC	65%	37
CVD	Nanorods	In doped	H_2 (500 ppm)	320ºC	80%	37
CVD	Nanowires	-	NO_2 (100 ppm)	200ºC	-0.6	38
CVD (VLS)	Nanowires	-	NO_2 (5 ppm)	200ºC	45.4	39
CVD (VLS)	Nanowires	Co_3O_4 decorated	C_2H_5OH (100 ppm)	400ºC	21.9	39
CVD	Microwires	-	EtOH (40 ppm)	15ºC	25%	40

CVD	Microwires	Au decorated	EtOH (40 ppm)	15ºC	55%	[40]
CVD	Urchin-like nanowires	-	EtOH (5 ppm)	350ºC	7	[41]
CVD	Urchin-like nanowires	Mg doped	EtOH (5 ppm)	350ºC	343	[41]
Hydrothermal	Nanowires	-	EtOH (50 ppm)	325ºC	1.2	[42]
Hydrothermal	Nanowires	Au-layer	EtOH (50 ppm)	325ºC	7	[42]
Hydrothermal	Nanorods	Vertically-aligned	NO_2 (100 ppb)	50ºC	13	[43]
Hydrothermal	Nanorods	Vertically-aligned UV illuminated	NO_2 (500 ppb)	200ºC	0.740	[44]

Hydrothermal	Nanorods	-	NO_2 (1 ppm)	350ºC	1.8	[45]
Sol-Gel	Nanorods	Au decorated	NO_2 (10 ppm)	300ºC	3.4 MΩ	[46]
Filtered Cathodic Vacuum Arc	Nanorods	-	EtOH (250 ppm)	280ºC	2.3	[47]
Cathodically Induced Sol-Gel	Thin Film	Vertically aligned	NO_2 (100 ppb)	200ºC	2	[48]
ZnO Nanoparticle layer	Nanofiber-Nanoparticle	-	EtOH (10000 ppm)	300ºC	150	[49]
Microwave-Assisted Hydrolysis	Nanorod	-	CO (100 ppm)	Room temperature	81%	[50]
Electrospinning and Hydrothermal	Hierarchical	CuO decorated	H_2S (5 ppm)	200ºC	83.5	[51]

Table 2-1: Some of the recently published works based on 1D ZnO nanostructures and their gas sensing properties

As one can see from table 1, there exists a wide range of techniques to produce several 1D ZnO nanostructures. However, the most common methods are CVD (and all their sub-types such as VLS, VS and so forth) and hydrothermal method. As stated before, CVD technique allows synthesising high purity and high crystalline ZnO nanostructures. For instance, *Van Dang et al.*[35] reported the growth of highly homogeneous ZnO nanowires with the typical hexagonal wurtzite crystalline structure. Additionally, no impurities could be found when analysed by XRD. Moreover, by means of CVD technique, well oriented nanostructures can be obtained. For example, *Park et al.*[38] reported the growth of ZnO nanowires by CVD, having previously deposited a Zn thin film via e-beam evaporation. They produced a highly vertically-oriented ordered array of ZnO and CuO nanowires over SiO_2 substrates. It is also reported that the diameter and length of the nanowires strongly depends on the thickness of the previously deposited thin film, and the growth temperature[38].

An additional important feature of CVD technique is that it allows us to decorate or dope the 1D nanostructures with other materials such as metals or other metal oxides in only one step. *Babu et al.*[37] reported the growth of In doped ZnO nanowires. Simply by adding In metal precursor to the Zn powder precursor necessary to produce ZnO nanowires, they obtained a highly ordered ZnO nanorods with different wt% of In doping. They report a VS method due to the lack of metal catalyst on the substrate. However, a ZnO thin film is deposited previous to the growth and as a consequence the nanorods are vertically aligned.

Na et al.[39] also reported the growth of ZnO nanowires, this time, decorated with Co_3O_4 nanoparticles. They reported de deposition of Co_3O_4 nanoparticles by thermal evaporation of $CoCl_2$ powders at 500ºC. They obtained Co_3O_4

nanoparticles, whose diameter ranges from 2 to 10 nm, uniformly deposited on the surface of the ZnO nanowires.

Hydrothermal method is also reported to be one of the most common techniques to produce 1D ZnO nanostructures. *Ramgir et al.*[42] reported the growth of ZnO nanorods by a hydrothermal method over ZnO nanoparticles deposited by a chemical route and that will act as a seed. After that an Au-layer was deposited on top of the nanorods by sputtering. Also, hydrothermal method allows one to synthezise ZnO nanostructures with a specific orientation. *Öztürk et al.*[43] and *Sahin et al.*[44] reported the fabrication of vertically aligned ZnO nanorods over a previously deposited ZnO thin film layer that acts as a seed over glass and ITO substrate respectively.

Apart from CVD and hydrothermal method, there are a wide range of techniques used by researchers in order to easily fabricate 1D ZnO nanostructures such as sol-gel, microwave assisted hydrolysis or electrospinning. All these techniques are able to produce ZnO nanowires and decorate or dope the material with other metals or metal oxides in order to enhance their gas sensing properties.

Regarding the gas sensing properties, ZnO has been reported to detect a wide range of oxidizing and reducing gases and vapours for example NO_2, H_2 and EtOH among many others. Usually, ZnO is reported to have its optimum working temperature around 250-350ºC, although there are some works that tend to decrease this temperature towards room temperature.

Na et al.[39] reported the selective sensing of 5 ppm of NO_2 at 200ºC with a reponse (calculated as $S = R_{gas}/R_{air}$) of 45.7. The cross sensitivity to other gases like CO, H_2 and C_3H_8 resulted negligible. Also if they decorate the sensor

with Co_3O_4 nanoparticles and they increase the sensing temperature to 400ºC the sensor becomes selective to 100 ppm C_2H_5OH with a response of 22 being negligible the cross sensitivity to NO_2. Furthermore, *Cho et al.*[41] reported the selective sensing of 1 ppm of NO_2 at 350ºC, without cross sensitivity to CO.

Also, lower concentrations of NO_2 gas can be detected with 1D ZnO nanostructures. *Öztürk et al.*[43] reported the sensing of 100 ppb of NO_2 at low temperatures (i. e. 50ºC) with a response of 13 ($S = R_{gas}/R_{air}$). Additionally, *Sahin et al.*[44] reported the sensing of 500 ppb of NO_2 of ZnO nanorods grown on ITO substrates with a response of 0.740 (calculated as $S = \Delta I/I_g$). However, the latter greatly decreased the response time of the sensor by irradiating the sensor with UV light.

Ethanol is another vapour, the detection of which has been often reported using 1D ZnO nanostructures. Usually, the optimum sensing temperature for this vapour is around 300-350ºC. Despite the good sensing properties of pure 1D ZnO nanostructures towards EtOH, it has been reported that decorating the ZnO nanostructures with metal nanoparticles can greatly enhance the sensing properties as well as the response and recovery time of the sensors. Zou et al. and Ragmir et al, demonstrated that decorating the ZnO nanostructures with Au, can enhance the response of the sensor towards EtOH vapours. The former, deposited the Au nanoparticles on the surface of the ZnO nanostructures by means of sputtering. They could increase the response of the sensor at 15ºC, and simultaneously decreasing the recovery time by a factor of 3. The latter deposited a thin layer of Au also by means of RF sputtering. They could increase the sensor response by a factor of 4 only with the effect of the Au thin film.

Kwak et al. decorated the 1D ZnO nanostructures with Mg nanoparticles and they achieved a response of 343 ($S = R_{air}/R_{gas}$) when using a concentration of 5 ppm of EtOH at 350ºC, almost 50 times higher than that of the pure ZnO nanostructures.

Apart from NO_2 and EtOH, good sensing properties toward other target gases like H_2, CO and H_2S have been reported.

2.3.2 Indium Oxide

Another important metal oxide that has attracted the attention in the past years is indium oxide (In_2O_3). In_2O_3 is an n-type semiconductor with a wide direct bandgap (around 3.6 eV at room temperature). In_2O_3 is one of the so-called transparent conducting oxides (TCOs) due to its high electrical conductivity and its high optical transparency. In_2O_3 has also a very interesting superconductor-insulator transition behaviour at low temperatures and low dimensions[52].

Crystalline form of In_2O_3 can be found in two ways: cubic (bixbyite type) and rhombohedral (corundrum type). The rohombohedral phase can only be found when the material is produced at high temperatures and high pressure or when using non-equilibrium growth methods. The most common phase type of In_2O_3 is the cubic one. The lattice is body-centered cubic with a lattice parameter of a=1.011 nm and it belongs to the space group Ia3 No. 206. Every In atom is six-fold coordinated to neighboring oxygen atoms (In(6c)). In figure 2-10, there is a representation of the unit cell of cubic In_2O_3[53].

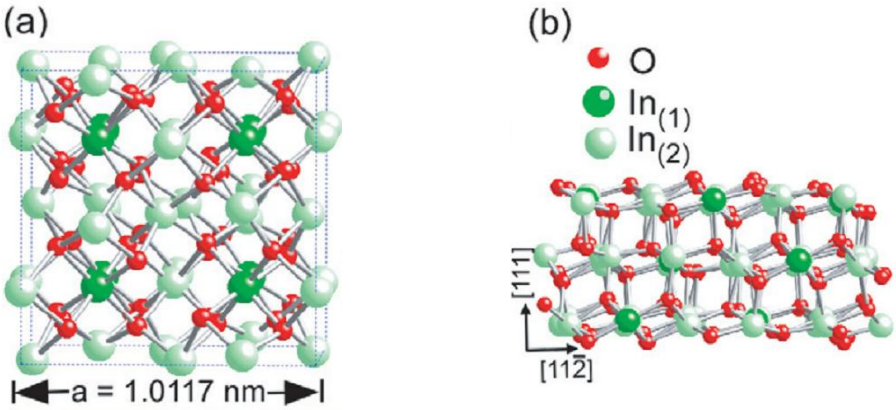

Figure 2-11: (a) unit cell of the In_2O_3 bixbyite structure and (b) side view of the unit cell with the (111) orientation.

Possible surface terminations contain either exclusive In or O atoms, which we can classify it as a polar surface. However, polar surfaces are usually unstable. Another possible orientation can be the (111), which consist of stacks of In-O-In trilayers with a zero dipole moment. These surfaces normally have low surface energy and they tend to produce themselves very thin films and a well-ordered structure. The fact that some reports have shown unusual adsorption of gases like CO on the In_2O_3 (111) motivates the research towards this particular surface orientation[54].

This particular feature has made of In_2O_3, and especially In_2O_3 oriented in the (111) direction, an excellent candidate for gas sensing applications. In the past years, not only 1D In_2O_3 nanostructures with many different morphologies such as nanowires, nanobelts, nanotubes but also 3D In_2O_3 nanostructures like octahedra, cubes and nanospheres of In_2O_3 have been studied for gas sensing purposes. Table 2-2 summarizes some of the most important and recent works on In_2O_3 nanostructures.

Synthesis Method	Morphology	Features	Target Gas	Working Temperature	Response	Reference
CVD	Nanowires	-	H_2 (400 ppm)	200ºC	0.60	31
MO-CVD	Thin Film	Low pressure measurements	NO_2	150ºC	3	55
CVD	Nanotowers	-	H_2 (2-1000 ppm)	240ºC	85%	56
AA-CVD	Thin Film	Ta doped	NO_2 (80 ppb)	400ºC	3.01	57
AA-CVD	Thin Film	Ti doped	NO_2 (80 ppb)	400ºC	1.80	57
Template CVD and Sputtuering	Nanotubes	-	EtOH (250 ppm)	300ºC	135.26%	58
Template CVD and Sputtuering	Nanotubes	Au-doped	EtOH (250 ppm)	300ºC	1219%	58

Hydrothermal	Flower-like	-	NO2 (200 ppb)	140ºC	40	59
Hydrothermal	Nanostructures	-	NO_2 (50 ppb)	125ºC	19.4	60
Hydrothermal	Nanocubes	-	H_2 (5 ppm)	150ºC	25	61
UV-Assisted Hydrothermal	Hollow Nanostructures	-	CH_2O (50 ppm)	200ºC	43	62
Solvothermal	Nanospheres	-	Nitropropane (100 ppm)	170ºC	≈340	63
Electrospinning	Hollow Nanofibers	-	Acetone (5 ppm)	300ºC	151	64
Electrospinnig	Micro/Nanotubes	-	HCHO (50 ppm)	240ºC	14.1	65
Ionic Layer Deposition	Thin Film	Au-doped	H_2	450ºC	8.5	66

			(1000 ppm)			
Sol-Gel	Octahedra	-	NO_2 (100 ppm)	200ºC	43	67
Ammonolysis and Re-oxidation	Octahedra Strings	-	HCHO (100 ppm)	420ºC	1.8	68
Ammonolysis and Re-oxidation	Crystal Chains	-	CH_3OH (100 ppm)	260ºC	3.2	69
Co-Precipitation	Nanoparticles	-	EtOH (1250 ppm)	350ºC	95	70
Co-Precipitation	Nanoparticles	Mn-doped	EtOH (1250 ppm)	350ºC	140	70
Colloidal Crystal Templating	Thin Film	-	EtOH (100 ppm)	175ºC	20	71
Colloidal Crystal Templating	Thin Film	Tm-doped	EtOH (100 ppm)	175ºC	122	71

Table 2-2: Overview of the most recent works based on In_2O_3 nanostructure gas sensors.

As we can see from table 2-2, a really wide range of techniques are being used to produce different morphologies of In_2O_3 nanostructures. As in ZnO nanostructures, CVD techniques are the most common for producing In_2O_3 nanostructures as well. For instance, *Qurashi et al*. [31] synthesised a wide range of 1D nanostructured In_2O_3 morphologies such as nanorods, nanowires and nanoneedles via a conventional CVD method. Depending on the temperature conditions, the resulting nanostructure will be different, that is, at 800ºC nanowires were produced and when the temperature was increased to 900ºC nanoneedles were synthesised. These results show that CVD method is able to produce several morphologies just by changing some parametes, for example the temperature.

Another similar morphology is produced by *Zheng et al*.[56], which synthesised nanotowers over Cr comb shaped interdigitated electrodes. The sides of the nanotowers are stacked up with octahedrons after another and, as a consequence, the nanostructure possesses high surface to volume ratio. However, 2D In_2O_3 nanostructures can also be produced by CVD as *Ali et al*.[55] synthesised thin films via a metal-organic CVD (MO-CVD) with a thickness of 200 nm.

Additionally, CVD techniques can also be used to produce metal doped In_2O_3 nanostructures, which are thought to enhance gas sensing properties. Bloor et al.[57] synthesised In_2O_3 thin films doped with Ta and Ti in only one step. The results showed that Ta doped thin film had a slightly smaller particle size than the pure In_2O_3 film, whereas the Ti doped had a greater particle size. This could be because of the additional Ti metal centres act as nucleation centre retardants, which leads to an increase in the particle size[57].

Apart from CVD techniques, there are other types of methods suitable to produce high quality In_2O_3 nanostructures. For example, *Xu et al.*[60] produced other kind of In_2O_3 nanostructured morphologies following this path. They reported high yield of flower-like nanostructures. Each individual nanostructured is composed of nanosheets with irregular edges which its shape is maintained even after calcination of the material. Also, nanostructures are found to be porous, which in theory is favourable for gas sensing applications, as the surface to volume ratio highly increases.

Also, *Shanmugasundaram et al.*[61] synthesised In_2O_3 nanocubes using a hydrothermal route. They also found that if the calcination is performed at temperatures higher than 400ºC, surface of the nanostructures start to become rough, slightly porous and with damaged edges.

Other In_2O_3 morphologies can also be synthesised, for instance In_2O_3 octahedra. Mu et al.[67] used a sol-gel technique in order to synthesise a high density of In_2O_3 nanostructures which had regular octahedral shape. An XRD analysis confirmed that the In_2O_3 octahedra had the typical cubic bixbyite crystal structure. Additionally, Yang et al.[68] produced a series of octahedral strings using a two step method consisting of ammonolysis and re-oxidation processes. They obtained a high agglomeration of octahedral strings deposited on a silicon wafer with no other morphologies involved. The nanostructures also possessed cubic crystal structure.

Regarding the gas sensing properties, In_2O_3 is often reported to be selective to gases like NO_2, although it has been also used to detect many other gases and vapours.

Mu et al.[67] were able to detect 100 ppm of NO2 at 400ºC with a sensor response of 43 (calculated as $S=R_g/R_a$). However, there have been other reports indicating that this material could be able to detect lower concentrations of NO_2 at relatively low temperatures. *Xu et al.*[60] synthesized flower-like In_2O_3 nanostructures and used them to selectively detect 50 ppb of NO_2 at 125ºC. Additionally, *Bloor et al.*[57] doped their In_2O_3 thin films in order to enhance the response of the sensor towards NO_2. It was found that the sensors doped with Ta were the ones that achieved the highest response to 800 ppb of NO_2 at 400ºC with a response of 3.01, whereas those doped with Ti only had a response of 1.80. Pure In_2O_3 sensors achieved a response of 1.30.

In_2O_3 nanostructures have also been used for the detection of reducing gases like H_2 or ethanol. *Qurashi et al.*[31] used their In_2O_3 nanowires synthesised by CVD for the detection of 400 ppm of H_2 at 200ºC with a response of 0.60 (calculated as $S=R_a-R_g/R_a$). However, lower concentrations of H_2 were detected by *Zheng et al.*[56]. Their nanotowers could detect as low as 2 ppm of H_2 at 240ºC with very good selectivity compared to other reducing gases and a good long term stability (30 days).

If we focus on ethanol, An et al.[58] synthesised In_2O_3 nanotubes using CVD and TeO_2 nanowires as a template and they used them for the detection of 250ºC of ethanol at 300ºC with a response of 135.26%. Also in order to improve sensor response, Au nanoparticles were used to decorate the In_2O_3 nanotubes. Under the same conditions they obtained a response of 1219%, substantially higher than that of the pure In_2O_3 nanotubes. These results show that the addition of metal nanoparticles to the metal oxide nanostructure greatly enhances the gas sensing properties.

Furthermore, Han et al.[71] successfully synthesised In_2O_3 thin films via a colloidal crystal templating method and they were doped with rare earth elements like thulium (Tm). They were able to detect 100 ppm of EtOH vapours at 175ºC. Again, the doped sensor showed a substantially higher response to EtOH vapours.

In addition to H_2 and EtOH, In_2O_3 nanostructures have been used to detect other gases like formaldehyde, acetone or other nitro compounds with good response.

2.4 Objectives

The objectives of this doctoral thesis will be defined as follows:

- ✓ First of all, the design and development of a reactor capable of easily producing high purity and high quality ZnO and In_2O_3 nanostructures with a reasonable yield via a chemical vapour deposition technique. Several depositions will be made in order to determine the optimum parameters for such purpose.
- ✓ Decorate the materials synthesised with noble metal nanoparticles such as Pt and Pd in order to improve the gas sensing properties of the material.
- ✓ Once we have obtained the desired nanostructures, structural characterization of the material will be the priority. Electronic, chemical and optical properties will be investigated with methods such as SEM, HRTEM, EDS, XRD, XPS and PL among others.

- ✓ Design of a proper gas cell in order to be able to characterize the gas sensing properties of the materials produced by CVD. Also, deposition of the materials synthesised on top of the sensors substrate, which contain an electrode on the front side and a heater on the back side.
- ✓ Characterization of the gas sensing properties of the ZnO and In_2O_3 nanostructures towards oxidising (mainly NO_2 and O_3) and reducing gases (particularly H_2, EtOH and CO among others) and vapours. Sensitivity, selectivity and response time will be investigated.
- ✓ Finally, in-situ operando techniques such as photoluminescence and DRIFT spectroscopy will be performed in order to investigate the possible sensing mechanisms of our materials

2.5 References

1. Seiyama, T.; Kato, A.; Fujiishi, K.; Nagatani, M., A New Detector for Gaseous Components Using Semiconductive Thin Films. *Analytical Chemistry* 1962, *34* (11), 1502-1503.
2. Arafat, M. M.; Dinan, B.; Akbar, S. A.; Haseeb, A. S. M. A., Gas Sensors Based on One Dimensional Nanostructured Metal-Oxides: A Review. *Sensors* 2012, *12* (6), 7207.
3. Yamazoe, N.; Sakai, G.; Shimanoe, K., Oxide Semiconductor Gas Sensors. *Catalysis Surveys from Asia* 2003, *7* (1), 63-75.
4. Sharma, S.; Madou, M., A new approach to gas sensing with nanotechnology. *Philosophical Transactions of the Royal Society of London A: Mathematical, Physical and Engineering Sciences* 2012, *370* (1967), 2448-2473.
5. Annanouch, F. E.; Haddi, Z.; Vallejos, S.; Umek, P.; Guttmann, P.; Bittencourt, C.; Llobet, E., Aerosol-Assisted CVD-Grown WO3 Nanoneedles Decorated with Copper Oxide Nanoparticles for the Selective and Humidity-Resilient Detection of H2S. *ACS Applied Materials & Interfaces* 2015, *7* (12), 6842-6851.
6. Rothschild, A.; Komem, Y., The effect of grain size on the sensitivity of nanocrystalline metal-oxide gas sensors. *Journal of Applied Physics* 2004, *95* (11), 6374-6380.
7. Franke, M. E.; Koplin, T. J.; Simon, U., Metal and Metal Oxide Nanoparticles in Chemiresistors: Does the Nanoscale Matter? *Small* 2006, *2* (1), 36-50.

8. Romain, A. C.; Nicolas, J., Long term stability of metal oxide-based gas sensors for e-nose environmental applications: An overview. *Sensors and Actuators B: Chemical* 2010, *146* (2), 502-506.
9. Choi, K. J.; Jang, H. W., One-Dimensional Oxide Nanostructures as Gas-Sensing Materials: Review and Issues. *Sensors* 2010, *10* (4), 4083.
10. Tiemann, M., Porous Metal Oxides as Gas Sensors. *Chemistry – A European Journal* 2007, *13* (30), 8376-8388.
11. Simon, I.; Bârsan, N.; Bauer, M.; Weimar, U., Micromachined metal oxide gas sensors: opportunities to improve sensor performance. *Sensors and Actuators B: Chemical* 2001, *73* (1), 1-26.
12. Yamazoe, N., New approaches for improving semiconductor gas sensors. *Sensors and Actuators B: Chemical* 1991, *5* (1), 7-19.
13. Comini, E.; Baratto, C.; Faglia, G.; Ferroni, M.; Vomiero, A.; Sberveglieri, G., Quasi-one dimensional metal oxide semiconductors: Preparation, characterization and application as chemical sensors. *Progress in Materials Science* 2009, *54* (1), 1-67.
14. Ramgir, N. S.; Yang, Y.; Zacharias, M., Nanowire-Based Sensors. *Small* 2010, *6* (16), 1705-1722.
15. Li, T.; Zeng, W.; Wang, Z., Quasi-one-dimensional metal-oxide-based heterostructural gas-sensing materials: A review. *Sensors and Actuators B: Chemical* 2015, *221*, 1570-1585.
16. Sun, Y.-F.; Liu, S.-B.; Meng, F.-L.; Liu, J.-Y.; Jin, Z.; Kong, L.-T.; Liu, J.-H., Metal Oxide Nanostructures and Their Gas Sensing Properties: A Review. *Sensors* 2012, *12* (3), 2610.
17. Vallejos, S.; Di Maggio, F.; Shujah, T.; Blackman, C., Chemical Vapour Deposition of Gas Sensitive Metal Oxides. *Chemosensors* 2016, *4* (1), 4.
18. Annanouch, F. E.; Vallejos, S.; Stoycheva, T.; Blackman, C.; Llobet, E., Aerosol assisted chemical vapour deposition of gas-sensitive nanomaterials. *Thin Solid Films* 2013, *548*, 703-709.
19. Parkin, R. B. a. I., *Novel Chemical Vapor Deposition Routes to Nanocomposite Thin Films, Advances in Nanocomposites - Synthesis, Characterization and Industrial Applications*. InTech.
20. Wagner, R. S.; Ellis, W. C., VAPOR-LIQUID-SOLID MECHANISM OF SINGLE CRYSTAL GROWTH. *Applied Physics Letters* 1964, *4* (5), 89-90.
21. Meyyappan, M., Catalyzed chemical vapor deposition of one-dimensional nanostructures and their applications. *Progress in Crystal Growth and Characterization of Materials* 2009, *55* (1–2), 1-21.
22. Gomez, J. L.; Tigli, O., Zinc oxide nanostructures: from growth to application. *Journal of Materials Science* 2013, *48* (2), 612-624.
23. Chun, J.; Lee, J., Various Synthetic Methods for One-Dimensional Semiconductor Nanowires/Nanorods and Their Applications in Photovoltaic Devices. *European Journal of Inorganic Chemistry* 2010, *2010* (27), 4251-4263.
24. Devan, R. S.; Patil, R. A.; Lin, J.-H.; Ma, Y.-R., One-Dimensional Metal-Oxide Nanostructures: Recent Developments in Synthesis, Characterization, and Applications. *Advanced Functional Materials* 2012, *22* (16), 3326-3370.

25. Walters, G.; Parkin, I. P., Aerosol assisted chemical vapour deposition of ZnO films on glass with noble metal and p-type dopants; use of dopants to influence preferred orientation. *Applied Surface Science* 2009, *255* (13–14), 6555-6560.
26. Navío, C.; Vallejos, S.; Stoycheva, T.; Llobet, E.; Correig, X.; Snyders, R.; Blackman, C.; Umek, P.; Ke, X.; Van Tendeloo, G.; Bittencourt, C., Gold clusters on WO3 nanoneedles grown via AACVD: XPS and TEM studies. *Materials Chemistry and Physics* 2012, *134* (2–3), 809-813.
27. Hou, X.; Choy, K. L., Processing and Applications of Aerosol-Assisted Chemical Vapor Deposition. *Chemical Vapor Deposition* 2006, *12* (10), 583-596.
28. Zervos, M.; Othonos, A., A systematic study of the nitridation of SnO2 nanowires grown by the vapor liquid solid mechanism. *Journal of Crystal Growth* 2012, *340* (1), 28-33.
29. Baxter, J. B.; Aydil, E. S., Epitaxial growth of ZnO nanowires on a- and c-plane sapphire. *Journal of Crystal Growth* 2005, *274* (3–4), 407-411.
30. Annanouch, F. E.; Haddi, Z.; Ling, M.; Di Maggio, F.; Vallejos, S.; Vilic, T.; Zhu, Y.; Shujah, T.; Umek, P.; Bittencourt, C.; Blackman, C.; Llobet, E., Aerosol-Assisted CVD-Grown PdO Nanoparticle-Decorated Tungsten Oxide Nanoneedles Extremely Sensitive and Selective to Hydrogen. *ACS Applied Materials & Interfaces* 2016, *8* (16), 10413-10421.
31. Qurashi, A.; El-Maghraby, E. M.; Yamazaki, T.; Kikuta, T., Catalyst supported growth of In2O3 nanostructures and their hydrogen gas sensing properties. *Sensors and Actuators B: Chemical* 2010, *147* (1), 48-54.
32. Anderson, J.; Chris, G. V. d. W., Fundamentals of zinc oxide as a semiconductor. *Reports on Progress in Physics* 2009, *72* (12), 126501.
33. Fu, Y. Q.; Luo, J. K.; Du, X. Y.; Flewitt, A. J.; Li, Y.; Markx, G. H.; Walton, A. J.; Milne, W. I., Recent developments on ZnO films for acoustic wave based bio-sensing and microfluidic applications: a review. *Sensors and Actuators B: Chemical* 2010, *143* (2), 606-619.
34. Kumar, R.; Al-Dossary, O.; Kumar, G.; Umar, A., Zinc Oxide Nanostructures for NO2 Gas–Sensor Applications: A Review. *Nano-Micro Letters* 2015, *7* (2), 97-120.
35. Van Dang, T.; Duc Hoa, N.; Van Duy, N.; Van Hieu, N., Chlorine Gas Sensing Performance of On-Chip Grown ZnO, WO3, and SnO2 Nanowire Sensors. *ACS Applied Materials & Interfaces* 2016, *8* (7), 4828-4837.
36. Yadav, K.; Gahlaut, S. K.; Mehta, B. R.; Singh, J. P., Photoluminescence based H2 and O2 gas sensing by ZnO nanowires. *Applied Physics Letters* 2016, *108* (7), 071602.
37. Babu, E. S.; Hong, S. K., Effect of indium concentration on morphology of ZnO nanostructures grown by using CVD method and their application for H2 gas sensing. *Superlattices and Microstructures* 2015, *82*, 349-356.
38. Park, W. J.; Kim, M. H.; Koo, B. H.; Choi, W. J.; Lee, J.-L.; Baik, J. M., Alternatively driven dual nanowire arrays by ZnO and CuO for selective sensing of gases. *Sensors and Actuators B: Chemical* 2013, *185*, 10-16.

39. Na, C. W.; Woo, H.-S.; Kim, I.-D.; Lee, J.-H., Selective detection of NO2 and C2H5OH using a Co3O4-decorated ZnO nanowire network sensor. *Chemical Communications* 2011, *47* (18), 5148-5150.
40. Zou, A. L.; Qiu, Y.; Yu, J. J.; Yin, B.; Cao, G. Y.; Zhang, H. Q.; Hu, L. Z., Ethanol sensing with Au-modified ZnO microwires. *Sensors and Actuators B: Chemical* 2016, *227*, 65-72.
41. Kwak, C.-H.; Woo, H.-S.; Abdel-Hady, F.; Wazzan, A. A.; Lee, J.-H., Vapor-phase growth of urchin-like Mg-doped ZnO nanowire networks and their application to highly sensitive and selective detection of ethanol. *Sensors and Actuators B: Chemical* 2016, *223*, 527-534.
42. Ramgir, N. S.; Kaur, M.; Sharma, P. K.; Datta, N.; Kailasaganapathi, S.; Bhattacharya, S.; Debnath, A. K.; Aswal, D. K.; Gupta, S. K., Ethanol sensing properties of pure and Au modified ZnO nanowires. *Sensors and Actuators B: Chemical* 2013, *187*, 313-318.
43. Öztürk, S.; Kılınç, N.; Öztürk, Z. Z., Fabrication of ZnO nanorods for NO2 sensor applications: Effect of dimensions and electrode position. *Journal of Alloys and Compounds* 2013, *581*, 196-201.
44. Şahin, Y.; Öztürk, S.; Kılınç, N.; Kösemen, A.; Erkovan, M.; Öztürk, Z. Z., Electrical conduction and NO2 gas sensing properties of ZnO nanorods. *Applied Surface Science* 2014, *303*, 90-96.
45. Cho, P.-S.; Kim, K.-W.; Lee, J.-H., NO2 sensing characteristics of ZnO nanorods prepared by hydrothermal method. *Journal of Electroceramics* 2006, *17* (2), 975-978.
46. Dilonardo, E.; Penza, M.; Alvisi, M.; Di Franco, C.; Palmisano, F.; Torsi, L.; Cioffi, N., Evaluation of gas-sensing properties of ZnO nanostructures electrochemically doped with Au nanophases. *Beilstein Journal of Nanotechnology* 2016, *7*, 22-31.
47. Ahmad, M. Z.; Sadek, A. Z.; Latham, K.; Kita, J.; Moos, R.; Wlodarski, W., Chemically synthesized one-dimensional zinc oxide nanorods for ethanol sensing. *Sensors and Actuators B: Chemical* 2013, *187*, 295-300.
48. Öztürk, S.; Kılınç, N.; Taşaltin, N.; Öztürk, Z. Z., A comparative study on the NO2 gas sensing properties of ZnO thin films, nanowires and nanorods. *Thin Solid Films* 2011, *520* (3), 932-938.
49. Wang, P.-P.; Qi, Q.; Xuan, R.-F.; Zhao, J.; Zhou, L.-J.; Li, G.-D., A facile method for enhancing the sensing performance of zinc oxide nanofibers gas sensors. *RSC Advances* 2013, *3* (43), 19853-19856.
50. Sin Tee, T.; Chun Hui, T.; Wu Yi, C.; Chi Chin, Y.; Umar, A. A.; Riski Titian, G.; Hock Beng, L.; Kok Sing, L.; Yahaya, M.; Salleh, M. M., Microwave-assisted hydrolysis preparation of highly crystalline ZnO nanorod array for room temperature photoluminescence-based CO gas sensor. *Sensors and Actuators B: Chemical* 2016, *227*, 304-312.
51. Vuong, N. M.; Chinh, N. D.; Huy, B. T.; Lee, Y.-I., CuO-Decorated ZnO Hierarchical Nanostructures as Efficient and Established Sensing Materials for H(2)S Gas Sensors. *Scientific Reports* 2016, *6*, 26736.

52. Gantmakher, V. F.; Golubkov, M. V.; Dolgopolov, V. T.; Tsydynzhapov, G. E.; Shashkin, A. A., Destruction of localized electron pairs above the magnetic-field-driven superconductor-insulator transition in amorphous In-O films. *Journal of Experimental and Theoretical Physics Letters* 1998, *68* (4), 363-369.
53. Erie, H. M.; Yunbin, H.; Mykola, V.; Bernard, D.; Ulrike, D., Surface structure of Sn-doped In 2 O 3 (111) thin films by STM. *New Journal of Physics* 2008, *10* (12), 125030.
54. Brinzari, V.; Korotcenkov, G.; Ivanov, M.; Nehasil, V.; Matolin, V.; Mašek, K.; Kamei, M., Valence band and band gap photoemission study of (1 1 1) In2O3 epitaxial films under interactions with oxygen, water and carbon monoxide. *Surface Science* 2007, *601* (23), 5585-5594.
55. Ali, M.; Wang, C. Y.; Röhlig, C. C.; Cimalla, V.; Stauden, T.; Ambacher, O., NOx sensing properties of In2O3 thin films grown by MOCVD. *Sensors and Actuators B: Chemical* 2008, *129* (1), 467-472.
56. Zheng, Z. Q.; Zhu, L. F.; Wang, B., In2O3 Nanotower Hydrogen Gas Sensors Based on Both Schottky Junction and Thermoelectronic Emission. *Nanoscale Research Letters* 2015, *10* (1), 1-14.
57. Bloor, L. G.; Manzi, J.; Binions, R.; Parkin, I. P.; Pugh, D.; Afonja, A.; Blackman, C. S.; Sathasivam, S.; Carmalt, C. J., Tantalum and Titanium doped In2O3 Thin Films by Aerosol-Assisted Chemical Vapor Deposition and their Gas Sensing Properties. *Chemistry of Materials* 2012, *24* (15), 2864-2871.
58. An, S.; Park, S.; Ko, H.; Jin, C.; Lee, W. I.; Lee, C., Enhanced ethanol sensing properties of multiple networked Au-doped In2O3 nanotube sensors. *Journal of Physics and Chemistry of Solids* 2013, *74* (7), 979-984.
59. Xu, X.; Li, X.; Zhang, H.; Feng, C.; Wang, C.; Liu, F.; Sun, Y.; Sun, P.; Lu, G., Synthesis, characterization and gas sensing properties of porous flower-like indium oxide nanostructures. *RSC Advances* 2015, *5* (38), 30297-30302.
60. Xu, X.; Wang, D.; Liu, J.; Sun, P.; Guan, Y.; Zhang, H.; Sun, Y.; Liu, F.; Liang, X.; Gao, Y.; Lu, G., Template-free synthesis of novel In2O3 nanostructures and their application to gas sensors. *Sensors and Actuators B: Chemical* 2013, *185*, 32-38.
61. Shanmugasundaram, A.; Ramireddy, B.; Basak, P.; Manorama, S. V.; Srinath, S., Hierarchical In(OH)3 as a Precursor to Mesoporous In2O3 Nanocubes: A Facile Synthesis Route, Mechanism of Self-Assembly, and Enhanced Sensing Response toward Hydrogen. *The Journal of Physical Chemistry C* 2014, *118* (13), 6909-6921.
62. Wang, X.; Meng, Y.; Li, G.-D.; Zou, Y.; Cao, Y.; Zou, X., UV-assisted, template-free synthesis of ultrathin nanosheet-assembled hollow indium oxide microstructures for effective gaseous formaldehyde detection. *Sensors and Actuators B: Chemical* 2016, *224*, 559-567.
63. He, Y.-Y.; Zhao, X.; Cao, Y.; Zou, X.-x.; Li, G.-D., Facile synthesis of In2O3 nanospheres with excellent sensitivity to trace explosive nitro-compounds. *Sensors and Actuators B: Chemical* 2016, *228*, 295-301.

64. Liang, X.; Jin, G.; Liu, F.; Zhang, X.; An, S.; Ma, J.; Lu, G., Synthesis of In2O3 hollow nanofibers and their application in highly sensitive detection of acetone. *Ceramics International* 2015, *41* (10, Part A), 13780-13787.
65. Wang, L.; Cao, J.; Qian, X.; Zhang, H., Facile synthesis and enhanced gas sensing properties of grain size-adjustable In2O3 micro/nanotubes. *Materials Letters* 2016, *171*, 30-33.
66. Korotcenkov, G.; Brinzari, V.; Han, S. H.; Cho, B. K., Gas-sensing properties of In2O3 films modified with gold nanoparticles. *Materials Chemistry and Physics* 2016, *175*, 188-199.
67. Mu, X.; Chen, C.; Han, L.; Shao, B.; Wei, Y.; Liu, Q.; Zhu, P., Indium oxide octahedrons based on sol–gel process enhance room temperature gas sensing performance. *Journal of Alloys and Compounds* 2015, *637*, 55-61.
68. Yang, W.; Wan, P.; Zhou, X.; Hu, J.; Guan, Y.; Feng, L., Self-assembled In2O3 truncated octahedron string and its sensing properties for formaldehyde. *Sensors and Actuators B: Chemical* 2014, *201*, 228-233.
69. Yang, W.; Wan, P.; Meng, H.; Hu, J.; Feng, L., Supersaturation-controlled synthesis of diverse In2O3 morphologies and their shape-dependent sensing performance. *CrystEngComm* 2015, *17* (15), 2989-2995.
70. Anand, K.; Kaur, J.; Singh, R. C.; Thangaraj, R., Structural, optical and gas sensing properties of pure and Mn-doped In2O3 nanoparticles. *Ceramics International* 2016, *42* (9), 10957-10966.
71. Han, D.; Yang, J.; Gu, F.; Wang, Z., Effects of rare earth element doping on the ethanol gas-sensing performance of three-dimensionally ordered macroporous In2O3. *RSC Advances* 2016, *6* (51), 45085-45092.

CHAPTER 3

Experimental Set-Up

In this chapter, we will describe the fabrication of the ZnO and In_2O_3 nanostructures as well as the reactors used for such purpose. Furthermore, a detailed explanation of the gas measurement system and the design and fabrication of the gas cell will be done as well as the set-ups used for the operand spectroscopy.

3.1 Growing the Nanostructures

In order to synthesise the metal oxide nanostructures, a conventional chemical vapour deposition (CVD) reactor has been used. It can be used for both catalized (VLS) and self-catalized (VS) growth.

3.1.1 CVD Reactor

When it comes to the design of a CVD reactor, one must take into account several key parameters for a successful nanostructure growth. These parameters include pressure, temperature and flow among others such as shape of the reaction chamber and inlet and outlet paths.

Needless to say that it is of paramount importance to have these parameters controlled at every moment. In our case we have turned a conventional tubular furnace into a fully operational CVD system.

First of all we designed a tubular quartz tube. It has been reported that the tube diameter is directly related with the deposition rate[1]. It was found that the optimum diameter for our quartz tube was 6 mm of internal diameter and 6.5 cm of external diameter. Such tube has a narrowing at the beginning and the end, which will fit in the inlet and outlet respectively. The quartz tube has a length of

90 cm. When the tube is introduced in the furnace, it is surrounded by circular heaters, which will provide a stable and uniform temperature in the central part of the tube. A schematic representation of the tube can be seen in figure 3-1.

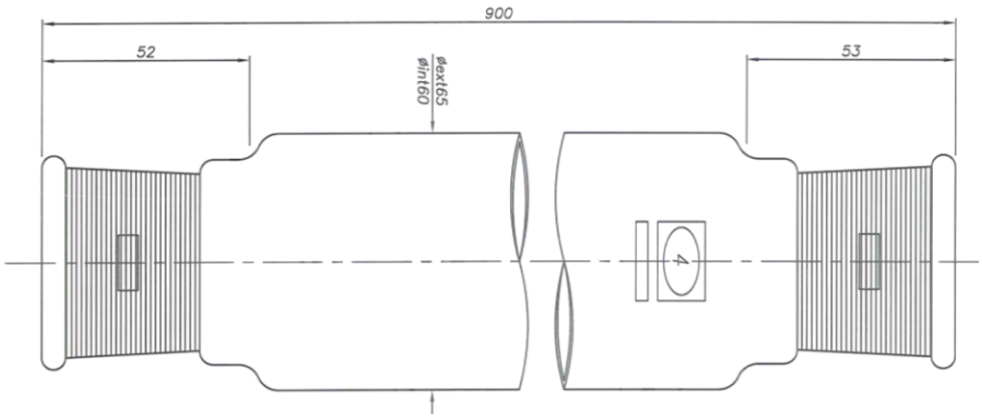

Figure 3-1: Schematic representation of quartz tube

The inlet is connected through a flow meter to a gas bottle. Many inert gases can be used as carrier gases such as N_2, He and Ar to name but a few. In our case, the carrier gas will be Ar. A scheme of the inlet and outlet pieces can be observed in figure 3-2.

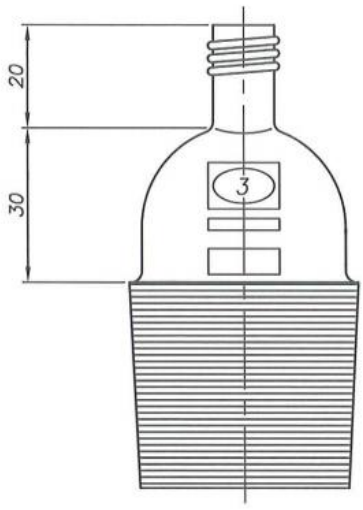

Figure 3-2: Schematic view of the inlet/outlet pieces.

At the centre of the quartz tube, an alumina bock (12x2.5x3 cm) is placed, where the substrate and the precursors will be located. The distance between the precursor and the substrate is of paramount importance. The correct growth of the nanostructures in the substrate will depend on such distance. If we put the substrate too close to the precursors we will not obtain the desired morphology, and if we put it too far, the density of the nanostructures will be really low. In our case, the optimum distance between the precursors and the substrate was found to be 1 cm.

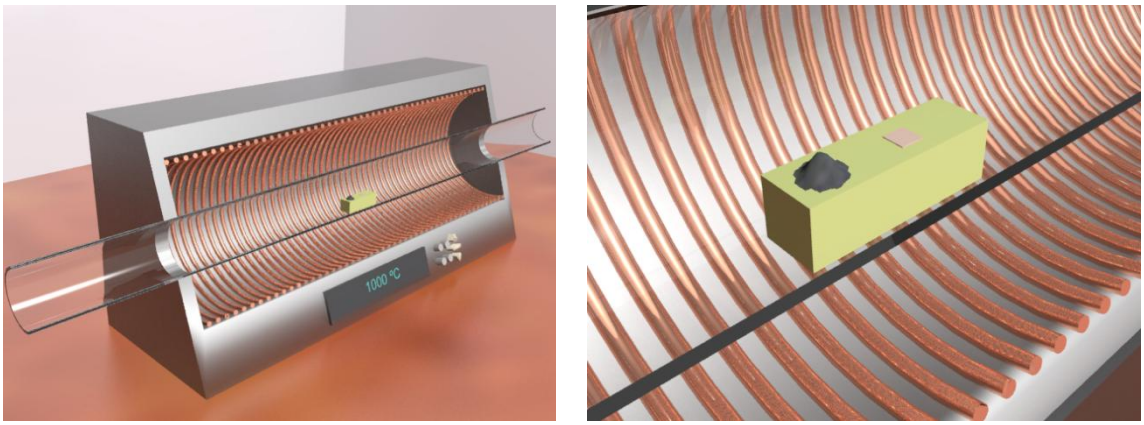

Figure 3-3: (Left) Schematic representation of the whole converted CVD and (right) schematic representation of the alumina block with the precursors and the substrate on top of it.

Finally, a calibration of the temperature is performed. It was found that our converted CVD is able to reach 1000ºC in a reasonable time (about 100 min), yet it can work at every temperature below 1000ºC.

A full calibration of the temperature is shown in figure 3-4.

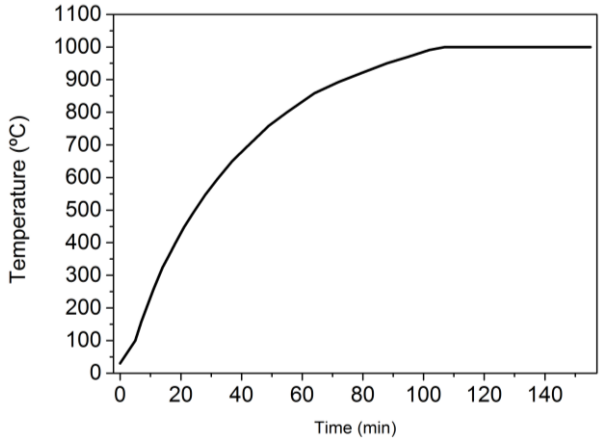

Figure 3-4: Calibration of the temperature of the CVD reactor

3.1.2 Finding the Appropriate Substrate

In order to successfully grow the metal oxide nanostructures and to be able to perform the gas sensing measurements, one has to adequately choose the substrate in which the growth is going to be carried out. This substrate must have some physical and chemical properties:

- Chemically stable
- Withstand high temperatures
- Robust
- If possible, low cost

With this purpose, we have chosen SiO_2 substrates for growing the nanostructures and alumina substrates for performing the gas sensing measurements.

3.1.2.1 SiO_2 Substrates

Silicon oxide is one of the most common substrates used in semiconductor industry. It has several properties that make it suitable for applications such as MOS transistors and substrates for CVD techniques.

It is easily deposited on various materials and growth thermally on silicon wafers. Also, it is resistant to many chemicals using during etching of other materials allowing at the same time to be selective etched with certain chemicals. In case of growing SiO_2 on top of Si, the interface has relatively few mechanical and electrical defects. Furthermore, it has a high dielectric constant and a relatively wide band gap, making it and excellent insulator. Finally, it has a high temperature stability (around 1600ºC) making it an outstanding material for process and device integration.

Usually, SiO_2 possesses an amorphous crystalline structure (yet crystalline SiO_2 is called quartz), a density of 2.0-2.3 g/cm^3 and a dielectric constant of ε_r=3.9. Also, it has a refractive index at optical wavelengths of n≈1.5 and a breakdown field larger than 10^7 C/cm. The combination of relatively good electrical properties of silicon and the excellent insulating properties of SiO_2 make it a perfect candidate for becoming a substrate for CVD processes.

There are several processes for oxidizing silicon wafers and obtaining a thin layer of SiO_2 on top of Si: thermal oxidation of Si and deposition of a SiO_2 thin film via chemical vapour deposition.

Thermal oxidation consists of introducing an oxidizing atmosphere to the surface of the silicon wafer with sufficient temperature to make the oxidation rate practical. For thermal oxidation, the process can be carried out in two ways:

- Dry oxidation
- Wet oxidation

It is worth to mention that oxides grown in dry atmospheres have a higher density, which implies less impurities and better quality oxide than that of grown in wet atmospheres.

In the reaction forming SiO_2, silicon atoms at the surface of the wafer must be converted to make the oxidized film. For a given volume of SiO_2 that is formed, a corresponding volume of the silicon substrate has to be lost. In crystalline silicon, each silicon atom corresponds to a volume of $2 \cdot 10^{-23}$ cm^3. In each SiO_2, each atom corresponds to a volume of $4.4 \cdot 10^{-23}$ cm^3, or about 2.2 times more than the volume in silicon. However, as the SiO_2 is forming, it cannot expand in all directions equally as it is constrained in the plane of the wafer. As a consequence, all of the volume difference is taken up by expansion in the vertical direction.

In our case, a 4-inch Si wafer is introduced in a furnace, where the temperature is increased at a rate of 5ºC/min until it reaches 1100ºC and it is maintained at this temperature for 6 hours. At the same time a flow of synthetic air is passed through the wafer. After this process, the wafer is cooled down to room temperature naturally resulting in the growth of around 250-300 μm of SiO_2 on top of the Si wafer.

Finally, this wafer is cut with a diamond pencil into 1 cm^2 pieces that will be used for the production of metal-oxide nanostructures via CVD techniques. However, before CVD is performed, the SiO_2 substrates should be cleaned by sonication. The cleaning process follows three steps of 5 minutes each in acetone, ethanol and deionised water, and then dried in synthetic air.

3.1.2.2 Alumina Substrates

Apart from SiO_2 substrates, there are other kind of material suitable for either performing synthesis on top of them or be used for gas sensing applications. The most common form of crystalline aluminum oxide is known as corundum, which is the thermodynamically stable form. The oxygen ions nearly form a hexagonal close-packed structure with aluminum ions filling two-thirds of the octahedral interstices.

Al_2O_3 is an insulator material; however, it has a relatively high thermal conductivity for a ceramic material, which makes it suitable for being used as a substrate in gas sensing applications.

Commercially available (CeramTec, *www.ceramtec.com/al2o3-ceramics)* alumina substrates (25.40 x 4.10 x 0.63 mm) with an interdigitated platinum electrode on the one side and a platinum heater on the back side (see Annex I) have been used for depositing the active layer and performing the gas sensing measurements. A picture of the alumina substrates is shown in figure 3-5.

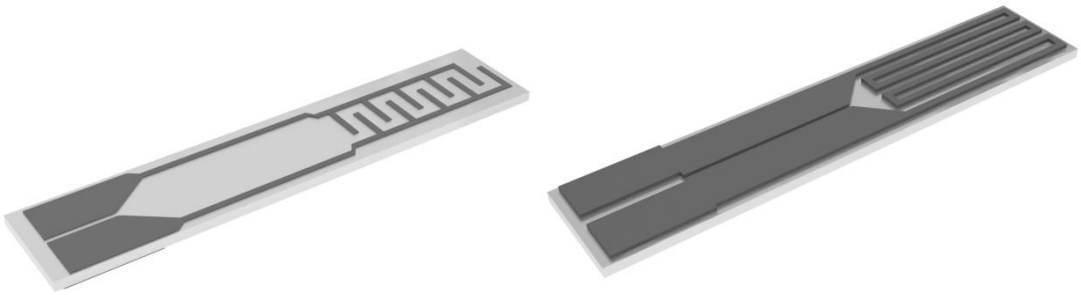

Figure 3-5: (Left) Image of the Pt electrode on the alumina substrate and (right) image of the Pt heater on the alumina substrate

The thickness of the platinum electrode and heater of the alumina substrate is around 7-8 μm.

3.2 Fabrication of the Sensor

After the synthesis of the material on top of SiO_2 substrates, it is removed from such substrate by scratching it and deposited by means of a screen printing technique on top of the alumina substrates described in the previous section.

3.2.1 Screen Printing Technique

In order to deposit the active material on top of the alumina sensors, screen printing technique has been chosen due to its several advantages to other methods such as drop coating, spin coating and spray coating.

Screen printing is a highly scalable and low cost technique for nanomaterial deposition with an extremely high reproducibility. The “standard” thick layer allows for the collective fabrication of microchips at very low cost as it enables the deposition of patterns with a controlled thickness (from 10 to few microns each deposition).

The basic principle of the screen printing technique involves forcing an ink or a paste through a screen comprising a mesh stretched over a frame. Thus, the frame is left open where is the need to print but occluded in areas where no deposit is required. Furthermore, the size of the holes in the mesh is determined by the thread diameter of the mesh material and the spacing of the threads in the weave. During the deposition, a squeegee pushes the ink or paste through the mesh. Obviously, the ink should pass freely through the holes in order to give a repeatable pattern and avoid blocking. After that, the mesh should be

peeled away immediately behind the squeegee, leaving the ink deposited on the printing surface.

A scheme of the screen printing technique can be seen in figure 3-6.

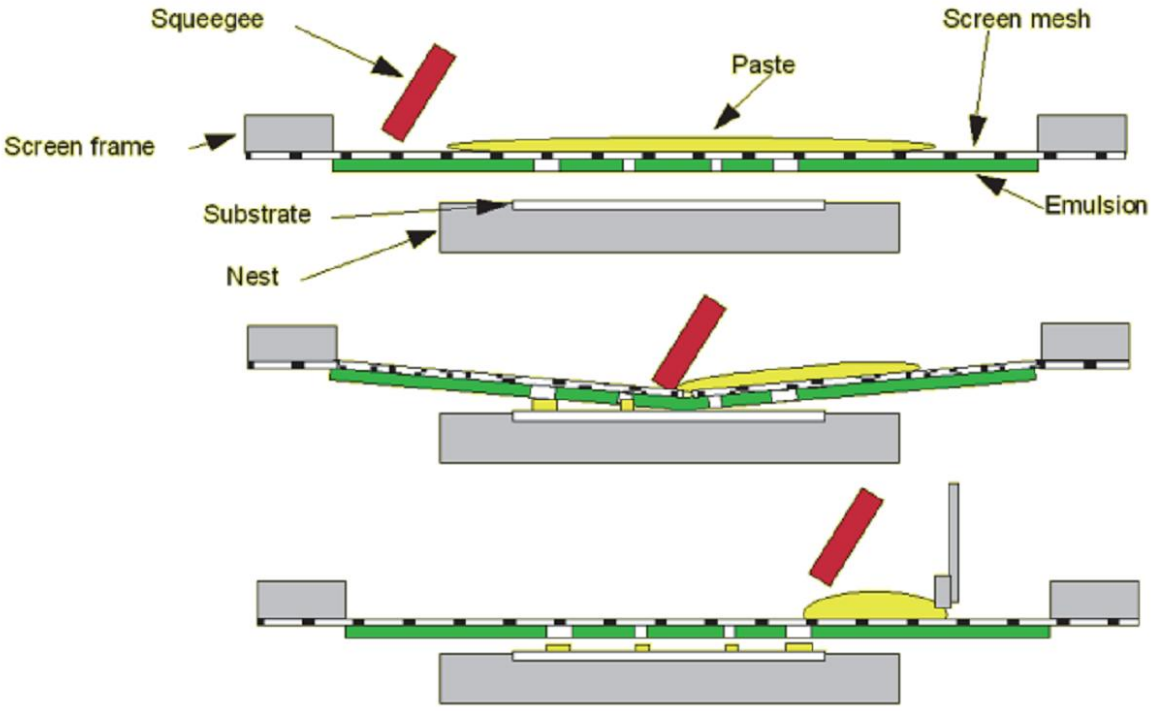

Figure 3-6: Scheme of the screen printing technique

In order to deposit our nanomaterial in the alumina substrates we have elaborated a paste, mixing our powder material with 1-2 propanediol to give the paste enough viscosity to perform the printing.

Also, a screen is made of a piece of stainless steel mesh stretched over a frame. A stencil is formed by blocking off the parts of the screen in the negative image of the design to be printed. Then, in order to deposit the layer, the screen is located over and just above the substrate. Continuously, the mesh is brought into the line contact with the squeegee scanning across the screen. At this point the paste should have deposited onto the substrate. After peeling away the

mesh, we perform an annealing of the sensor overnight, with a ramp of 5ºC/s up to 400ºC. After that, natural cool down to room temperature was performed. During the whole process, a 50 ml/min flow of synthetic air was present.

3.2.2 Deposition of Metal Nanoparticles. Sputtering Technique

As shown in chapter 2, the addition of metallic nanoparticles to the semiconductor metal oxide active layer, is a way to dramatically enhance the response of the sensor towards several target gases. Such deposition of nanoparticles can conducted by a sputtering technique[2].

This technique is commonly used in the field of gas sensors due to the possibility to deposit a great deal of pure metals, such as Au, Pt, Pd, Rh and so on, with high reproducibility and high speed.

Sputtering is a physical vapor deposition based on plasma, generally argon, which physically etches a target. As a consequence, some nanoparticles that are pulled away from it eventually get deposited on the active layer.

A 3D representation of the final sensor can be seen in figure 3-7

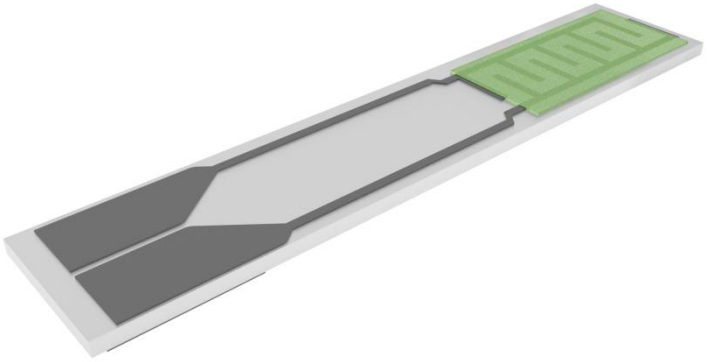

Figure 3-7: 3D representation of the final state of the sensor

3.3 Gas Sensor Measurements

The choice and the design of a suitable gas cell will be of paramount importance at the time of obtaining the response towards target gases and vapours.

3.3.1 Design of the Gas Cell

Usually, a sensor response is determined by the so-called “3s”, that is, sensitivity, selectivity and stability. However, there are other parameters that highly influence either the sensor response time to a certain target gas or the recovery time in clean air. There are certain limitations due to the sample delivery system that are specific of every experimental set-up. As a consequence, understanding the behaviour of the flow inside of the gas cell becomes of vital importance when evaluating the sensor response and recovery time among other parameters[3].

In order to optimize the geometry of the gas cell, some simulations have been carried out employing the COMSOL Multiphysics software.

The Navier-Stokes equation describes the motion of viscous fluid substances. They describe how the velocity, density and viscosity are related. As the Navier Stokes equations have no analytical solution, one has to make some approximations. For instance, we will consider and incompressible flow. In fluid dynamics, an incompressible fluid is a fluid whose density is constant. It is the same throughout space and it does not change through time. It is an idealization used to simplify analysis because in real life, all fluids are

compressible to some extent. We will also consider laminar flow. Finally, we can write the Navier Stokes equation as follows:

$$\rho \frac{\partial \boldsymbol{u}}{\partial t} + \rho(\boldsymbol{u} \cdot \nabla)\boldsymbol{u} + \nabla p - \eta \nabla^2 \boldsymbol{u} = \boldsymbol{g}$$

With $\nabla \cdot u = 0$ for an incompressible flow.

Where ρ is the fluid density, u is the flow velocity, η is the dynamic fluid viscosity, p is the pressure and g represents the body accelerations acting on the continuum from various origins (such as gravity).

The material used for the fabrication of the cell was Teflon. Teflon is a thermoplastic polymer, solid at room temperature, with a density of about 2200 kg/m^3. It maintains its strength and self-lubrication at low temperatures down to 5 K and good flexibility at temperatures above 194 K. Furthermore, it is hydrophobic, that is, water, alcohols and other polar oxygen and hydroxyl containing compounds will not adhere to, absorb on because of the high electronegativity of the fluorine atoms. This gives the material a good dielectric properties and an ideal insulator characteristic.

It is very non-reactive due to the strength of its carbon-fluorine bonds. As a matter of fact, it gains its properties from the aggregate effect of such bonds, as all fluorocarbons. The only chemicals known to affect these carbon-fluorine bonds are highly reactive metals like alkali metals, and at higher temperature also metals such as aluminum and magnesium among some others. For our applications, Teflon becomes the perfect material for the cell fabrication.

Our cell has been designed for hosting up to six sensors at the same time trying to keep the overall inner volume as small as possible. It consists of two pieces: the first one is used for plugging-in the sensors, and the second one contains the cavity for the gas to flow. A scheme of the gas cell can be seen in figure 3-8.

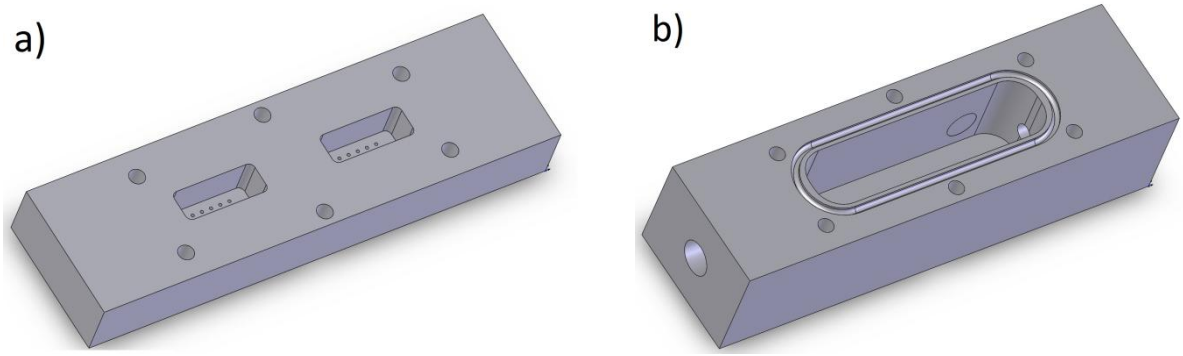

Figure 3-8: a) Base of the gas cell where the sensors are connected and b) cover of the sensor where the gas will flow

Figure 3-8 a) shows the base of the cell. It contains two cavities where a connector will be placed in order to be able to attach the sensors.

In order to know the behavior of the gas inside the gas cell, we have performed some simulations via COMSOL Multiphysics. The geometry employed for performing such simulations is shown in figure 3-9.

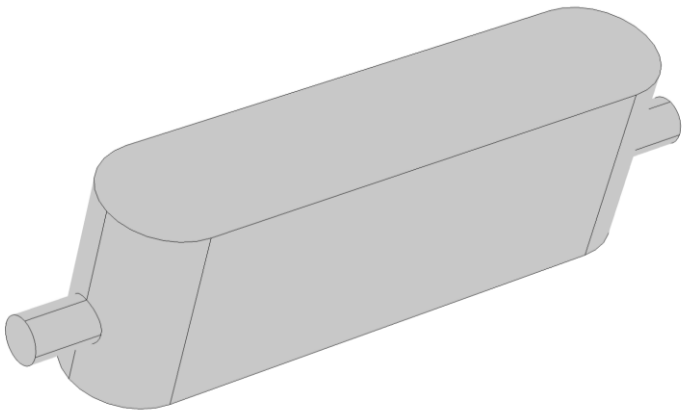

Figure 3-9: Volume used for performing COMSOL simulations

This volume corresponds to the inner volume of the gas cell. The flow enters longitudinally to the sensors from one side and exits from the other side. Results of the simulations are provided in figure 3-10.

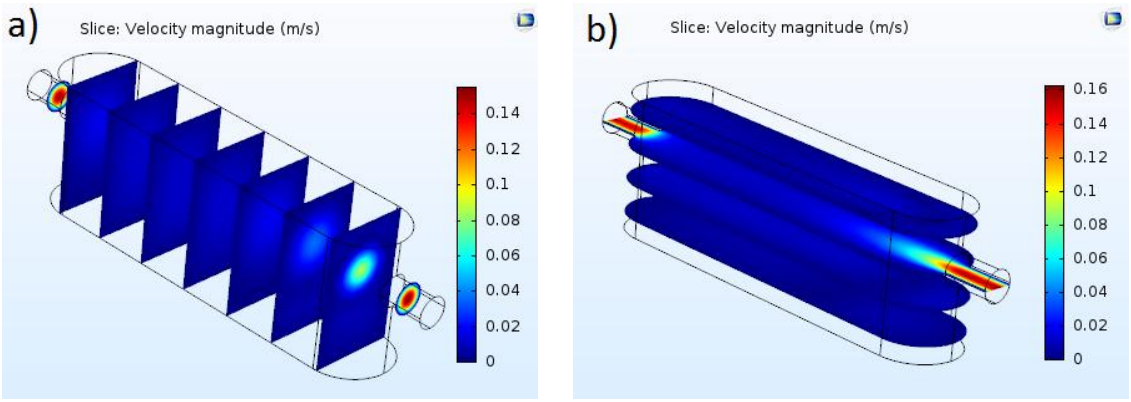

Figure 3-10: a) XZ planes and b) XY planes of the simulations performed on the gas cell

We can clearly see that the variation in the velocity magnitude at the centre of the cell, where the sensors will be located, is small enough in the whole section. As a consequence, low turbulence is observed at the entrance of the cell, and then the flow becomes laminar within the cell until it reaches the outlet. The fact that no turbulence is observed at the corners of the cell means that the change in the chemical environment of the cell (when the flow is changed from air to gas and vice versa) is really efficient.

Finally, this cell was fabricated in our mechanical workshop.

3.4 Gas Measurement System

In order to characterize the performance of the sensors a special gas line was designed and assembled for delivering the target gas concentrations in a

reproducible way. Gas sensors properties were obtained using the Teflon gas cell described in the previous section. Computer-controlled mass-flow (FIC, Flow Indicator and Controlled) meters (Bronkhorst hi-tech 7.03.241) and calibrated gas bottles were used (NO_2, H_2, benzene, CO, Ethanol and so on) all diluted in pure air. This system allows us to obtain different concentrations of the species tested. The general scheme for the gas measurement system used is presented in figure 3.11.

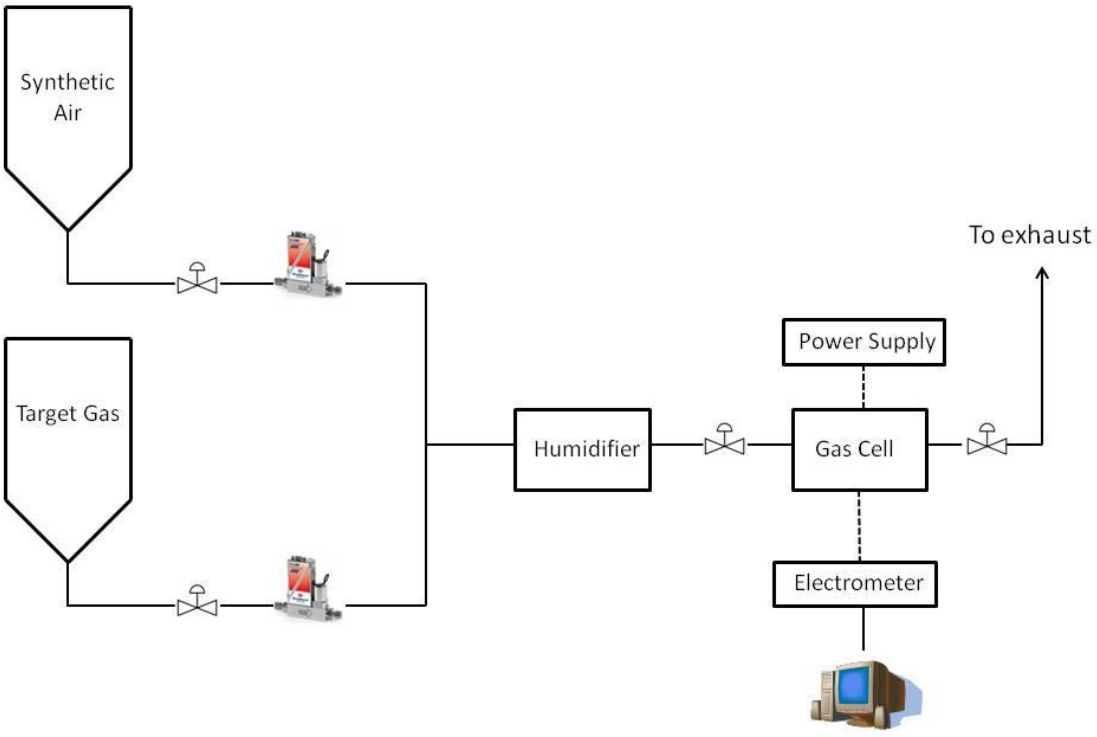

Figure 3-11: Scheme of the gas measurement system used

A continuous flow of 100 ml/min was used throughout all measurements. Furthermore, the flow could be humidified to 10-80% of relative humidity by employing an Environics Series 4000 gas mixing system (Environics Inc., Tolland, CT, USA). Once sensors were placed in the cell, they were connected

to a multimeter, which allowed real-time reading. Additionally, a power supply was connected in order to be able to measure the sensors at the desired temperature. Given the low concentration levels tested, the measurement rig was checked to rule out the presence of contaminants in mass-flow and tubing.

3.5 Operando Spectroscopy

In addition to gas measurements, some in situ operand spectroscopic measurements have been performed such as photoluminescence and DRIFTS (Diffuse Reflectance Infrared Fourier Transform Spectroscopy) in order to reach a better understanding of the sensing mechanism.

3.5.1 Photoluminescence

The phenomena which involve absorption of energy and the subsequent emission of light are classified generally under the term of luminescence. Phosphor and luminescent materials that emit light when excited by radiation are usually microcrystalline.

Luminescence can be divided into fluorescence and phosphorescence. The former is commonly used by chemists when the absorbing and emitting species are atoms or molecules, and the latter is similar except that the time between absorption and emission is much longer than that of the fluorescence. Then, photoluminescence is the term used to describe the absorption and emission of light by materials such as semiconductors and nanostructures. However, regardless of the terminology, when samples absorb photons and then emit at

different wavelengths, the resultant light can be analyzed with a spectrometer and information can be obtained about the sample.

A semiconductor is characterized by an electronic band structure in which the highest-occupied energy band, called valence band (VB), and the lowest-occupied energy band, called conduction band (CB) are separated by a band gap. Some sub-bands in the band gap region are related to surface defects and surface states. The energy band gap is the energy difference between the CB bottom and VB top. A scheme of the PL process is shown in figure 3-12.

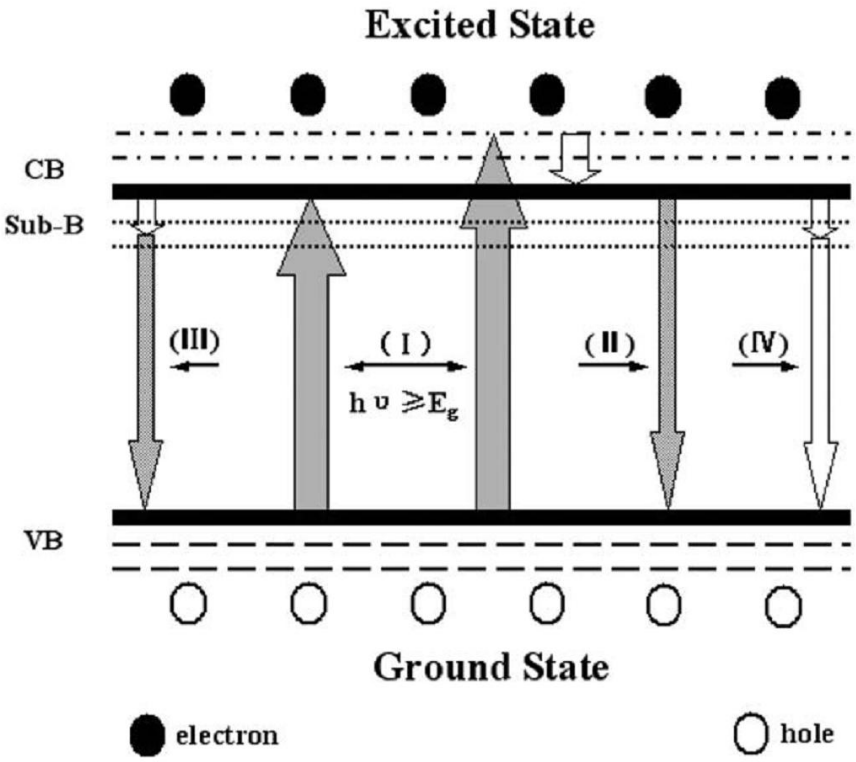

Figure 3-12: Scheme of the PL mechanism[4].

The photoluminescence mechanism is described as follows:

I. When the material is excited with light, electrons from the VB are promoted to the CB with different energy levels to become different

excited states, with the simultaneous generation of holes in the VB. In order to this to happen, energy of absorbing light has to be higher than the energy of the band gap of the material.

II. If nothing happens to the promoted electron located in the CB, most likely it will be recombined with a hole of the VB, releasing energy as radiation. In this case, the photon energy is equal to the band gap energy.

III. Excitonic PL process in which non-radiative transitions of excited electrons from the CB bottom to different sub-bands occur before the radiative transition from such sub-band to the top of the VB. In this case, the energy of the photon released is lower than that of the band gap. This process is usually originated from oxygen vacancies and other defects present in the material

IV. Finally, excited electrons in the CB can come back directly to the VB or indirectly by non-radiative transitions.

Therefore, all these possible electronic transitions make of photoluminescence technique a very interesting method in order to know the surface states of the semiconductor as well as its possible defects and impurities.

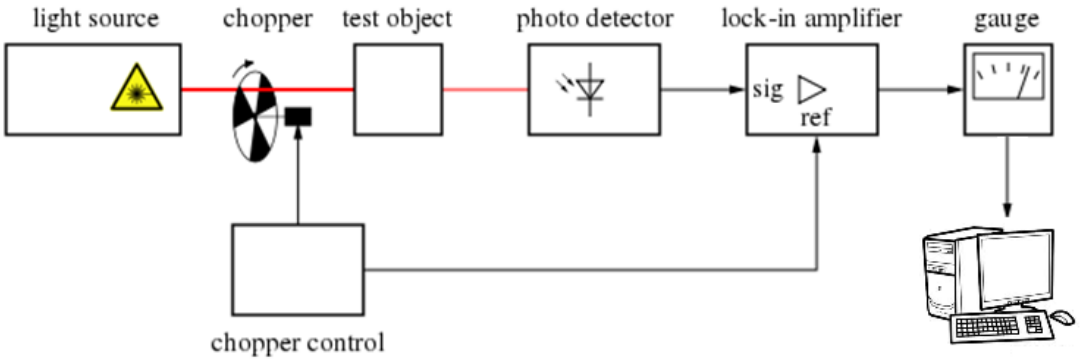

Figure 3-13: Scheme of the PL set-up used

The experimental set-up used for performing PL measurements is shown in figure 3-13. As a light source, we have used a Kimmon IK Series He-Cd CW laser which has its main line at 325 nm. After the laser beam hits the sample, the resulting luminescence reaches the photodetector that consists of a monochromator (Oriel Instruments 74000) which will separate each wavelength. After that, the beam is detected by a Hamamatsu E717-500 photomultiplier. Additionally, all sources of noise were removed with a Stanford Research System SR830 DSP lock-in amplifier connected to the chopper system. Needless to say, our sample was connected to a gas line in order to be able to perform in situ PL experiments.

3.5.2 DRIFT Spectroscopy

Diffuse reflectance spectroscopy is a really powerful technique for the study of materials. Surface states are usually important and can be altered by different mechanisms and processes.

Diffuse reflectance infrared Fourier transform (DRIFT) has been shown to be very sensitive and an excellent in situ technique. DRIFT is a surface localized FTIR spectroscopy, since it can provide both chemical and structural information for all types of solid surfaces.

When infrared light reaches the surface of the material, such light can be adsorbed, reflected from the surface or it can penetrate the sample before being scattered. If the scattering centres are randomly oriented, the phenomenon is isotropic and generates a diffuse reflectance. The scattered light is then collected and relayed to the IR detector, where the absorption by chemical groups is revealed.

DRIFT spectroscopy possesses several advantages compared to other commonly used spectroscopic techniques; it is a fast and non-destructive method, since the sample can be directly analyzed and it is better suited to the analysis of strongly absorbing materials which have a very low signal[5, 6].

In this work we have performed DRIFTS measurements simultaneously with gas sensing experiments in order to try to unravel the surface species and the sensing mechanism.

For the operando characterization of the gas sensors we used the following procedure:

In our experiments, a Vertex80v (narrow-band MTC detector, internal glowbar; 1024 scans per spectrum, 4cm^{-1} spectral resolution) FT-IR spectrometer was used for measurements in air. The sensors were placed in a homemade chamber with a KBr window, which was mounted in a diffuse reflectance spectroscopy cell (Harrick “Praying Mantis”), and were heated using the backside heater of the substrate described in this chapter. Additionally, the

resistance of the sensing layer was recorded by a digital multimeter. Gases were dosed using a homemade mixing station. Finally, all the experiments were conducted using a flow of 200 ml/min[7].

3.6 References

1. Komiyama, H.; Shimogaki, Y.; Egashira, Y., Chemical reaction engineering in the design of CVD reactors. *Chemical Engineering Science* 1999, *54* (13), 1941-1957.
2. Stankova, M.; Vilanova, X.; Calderer, J.; Llobet, E.; Brezmes, J.; Gràcia, I.; Cané, C.; Correig, X., Sensitivity and selectivity improvement of rf sputtered WO3 microhotplate gas sensors. *Sensors and Actuators B: Chemical* 2006, *113* (1), 241-248.
3. Ménil, F.; Susbielles, M.; Debéda, H.; Lucat, C.; Tardy, P., Evidence of a correlation between the non-linearity of chemical sensors and the asymmetry of their response and recovery curves. *Sensors and Actuators B: Chemical* 2005, *106* (1), 407-423.
4. Liqiang, J.; Yichun, Q.; Baiqi, W.; Shudan, L.; Baojiang, J.; Libin, Y.; Wei, F.; Honggang, F.; Jiazhong, S., Review of photoluminescence performance of nano-sized semiconductor materials and its relationships with photocatalytic activity. *Solar Energy Materials and Solar Cells* 2006, *90* (12), 1773-1787.
5. Urban, M. W.; Craver, C. D., *Structure-Property Relations in Polymers*. American Chemical Society: 1993; Vol. 236, p 852.
6. Accardo, G.; Cioffi, R.; Colangelo, F.; #039; Angelo, R.; De Stefano, L.; Paglietti, F., Diffuse Reflectance Infrared Fourier Transform Spectroscopy for the Determination of Asbestos Species in Bulk Building Materials. *Materials* 2014, *7* (1), 457.
7. Degler, D.; Wicker, S.; Weimar, U.; Barsan, N., Identifying the Active Oxygen Species in SnO2 Based Gas Sensing Materials: An Operando IR Spectrsocopy Study. *The Journal of Physical Chemistry C* 2015, *119* (21), 11792-11799.

CHAPTER 4

Synthesis and Characterization

In this chapter we will explain in detail the synthesis process and the characterization of the two materials used in this thesis. First, ZnO nanowires will be reviewed including the formation, orientation and some optical and electronic characterization. Finally, In_2O_3 octahedra will be as well reviewed including their formation and further characterization.

4.1 ZnO Nanowires

Semiconductor metal oxides have become a major technological drive in the field of gas sensing because of their low cost, high sensitivity, fast response and their relative simplicity. Among others, nanostructured zinc oxide (ZnO)[1] is an interesting material for its unique electric and optoelectronic properties. Its wide direct band gap (around 3.37 eV) at room temperature as well as its extremely large binding energy (around 60 meV), much higher than those of widely used metal oxides such as GaN (25 meV), make it suitable not only for gas sensing[2] but also for other applications such as solar cells[3], [4], lasers[5] and waveguides[6]. Moreover, it possesses high breakdown fields, large electron saturation rates, high resistance and efficient luminescence as well[7].

With the use of well aligned ZnO nanowires, several electronic problems can be solved. For instance, it is expected that with aligned nanowires a more direct conduction pathway from the point of electron-hole pair generation to the collection electrode would significantly improve the electron transport efficiency.

If one wants to produce well-aligned ZnO nanowires, the substrate becomes a parameter of paramount importance. Not every substrate is suitable for growing such nanowires. As a matter of fact, there are only a few substrates

that fulfil the conditions in order to obtain ZnO nanowires oriented in the desired directions. The matching between the lattice parameters and crystal structure of the substrate and the nanowires, will dramatically affect the crystal growth behaviour and the quality.

A variety of methodologies, such as thermal evaporation[8], and hydrothermal methods[9], have been reported for the synthesis of well-aligned ZnO nanowires (NWs). Among all these techniques, chemical vapour deposition (CVD) excels because it enables us to fabricate a wide range of single crystal nanostructures such as 1D nanowires in tens of minutes rather than in several hours. However, the multiple methods that can be envisaged to produce well-aligned nanowires, result in the properties of such nanowires being strongly dependent on the fabrication conditions and the preparation methods.

In this thesis, we have used the vapour-liquid-solid (VLS) technique to produce well-aligned nanowires on top of sapphire (Al_2O_3) substrates cut in several crystallographic directions to ensure that the ZnO nanowires are obtained in the desired directions.

4.1.1 Synthesis of ZnO Nanowires

ZnO nanowires were synthesized via the vapour-liquid-solid (VLS) process using a chemical vapour deposition (CVD) furnace[10]. It consists of three main steps: 1) Creation of the liquid alloy of the Au catalyst and the material to deposit; 2) nucleation of the material at the liquid-solid interface; and 3) growth of the nanowires. The nucleation and growth of the solid ZnO nanowires occur due to supersaturation of the liquid droplet. A schematic view of the VLS

process can be observed in figure 4-1. Previously to the growth of the metal oxide nanowires, a 3 nm Au thin layer that will act as a catalyst was deposited by sputtering onto the sapphire substrates. The precursor was a powder of ZnO and graphite (125 mg), and Ar was used as carrier gas. Both the precursor and the substrate were placed on a quartz boat into the horizontal CVD furnace. The substrate was placed 1 cm away from the precursor and samples were grown in different batches. Then, the temperature was raised to 900°C and kept constant for 30 minutes. The optimum Ar gas flow was 400 ml/min. To synthesize ZnO nanowires via VLS, it is essential to decompose the ZnO powder, and to enable this decomposition to occur at 850°C, the ZnO powder is mixed with graphite.

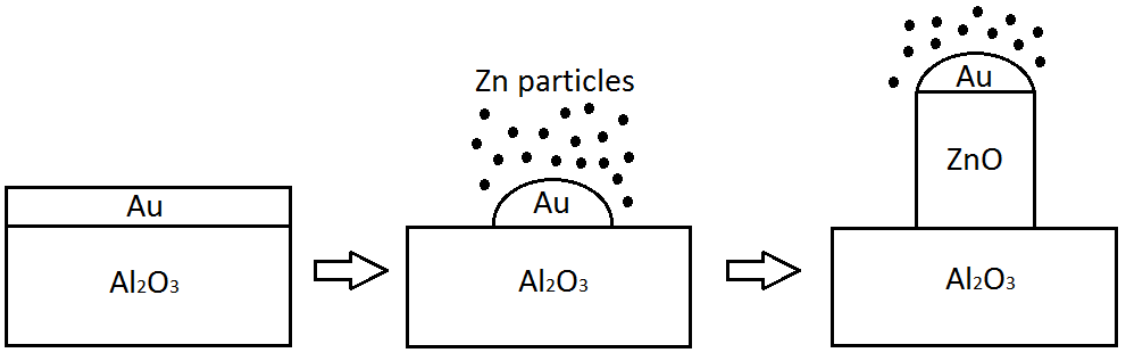

Figure 4-1: Schematic view of the VLS process for our ZnO nanowires. First, at high temperatures, the Au layer turns into droplets. Then, Zn atoms condense and attach to the Au droplet. Finally, when the Au droplet becomes supersaturated, the bottom-up growth of the ZnO nanowires takes place.

All the process was carried out under atmospheric pressure. It goes without saying that due to the specific experimental conditions, there is no relative humidity present during the process. As a result, relative humidity has no influence on the growth of the ZnO nanowires. Moreover, the temperature at which the growth takes place (900ºC) the relative humidity present can be neglected.

Three different types of sapphire (Al_2O_3) substrates were used, with different crystallographic directions in order to grow ZnO nanowires oriented along the c-plane (0001), r-plane (1-102) and a-plane (11-20). The match between the lattice parameter of the ZnO and that of the sapphire will allow us to epitaxially grow ZnO nanowires.

4.1.2 ZnO Nanowires' Characterization

FESEM images of the ZnO nanowires grown over the three sapphire substrates (c-, r-, and a-planes) are presented in figure 4-2. In all cases, the diameter of the nanowires was about 70 nm and the length was about 1 μm. The dimension of the nanowires was dependent on the deposition time and also the thickness of the Au layer, being deposited prior to the synthesis and working as a catalyst during the ZnO nanowire growth[11]. Hence, these two parameters were kept the same for the three samples. As evident from figure 4-2, distinct orientations of the ZnO nanowires were observed for the different sapphire substrates used.

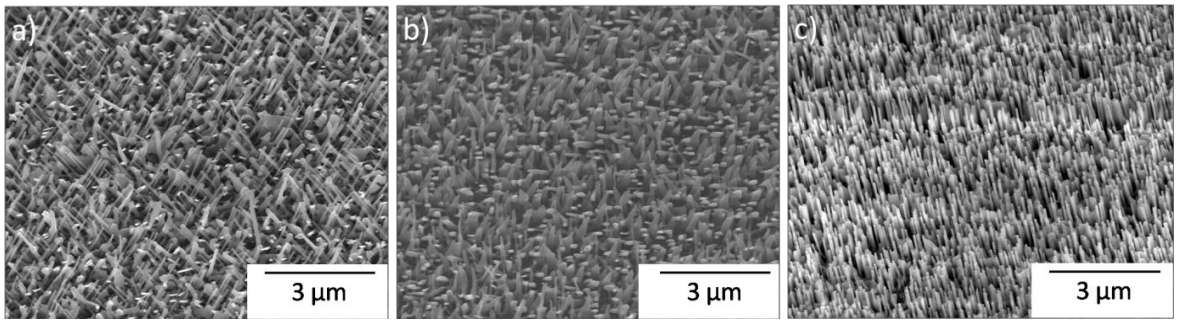

Figure 4-2: FESEM images of the ZnO nanowires grown over a) c-, b) r-, and c) a-planes

For the c-plane substrate (figure 4-2a), the nanowires grew tilted at 51 and 129°, relative to the substrate. For the r-plane (figure 4-2b), the nanowires showed a conical shape; they did not exhibit a well-defined orientation and many wire-to-wire junctions were present. This could be explained by the generation of stress during the initial stage of growth, thus joining together to make thicker structures along the growth[11]. Finally, for the a-plane (figure 4-2c), the nanowires grew vertically aligned. It is well known that nanowires grow following the exposed crystalline structure of the substrate.

Nucleation at the initial stage has a crucial role in in-plane alignment of the nanowires. It is known that ZnO nuclei grow with an epitaxial relationship with, in this case, c-, a- and r-plane sapphire due to the lattice match between them[12]. The c- a- and r-planes of sapphire and the c-plane of ZnO are related by a factor of 4, with a mismatch of less than 0.08% at room temperature. This relationship leads to vertical epitaxial growth on ZnO nanowires on top of a-plane sapphire substrates[13]. The reduced lattice mismatch between ZnO and sapphire is generally attributed to homogenous (isotropic) orientations[14]. The visual inspection shows that the lattice matching is more significant between ZnO nanowires and c- and a-plane sapphire substrates as evidenced by strong preferential orientation of the nanowire growth directions.

Further TEM and HR-TEM analysis have been performed on the ZnO nanowires as one can see in figure 4-3. HR-TEM image of the main body and boundaries of the nanowires clearly shows the lattice fringes with an interplanar spacing of around 0.52 nm which corresponds to the d-spacing (0002) crystal planes.

No dislocates or stacking can be observed as the crystalline fringes are structurally uniform.

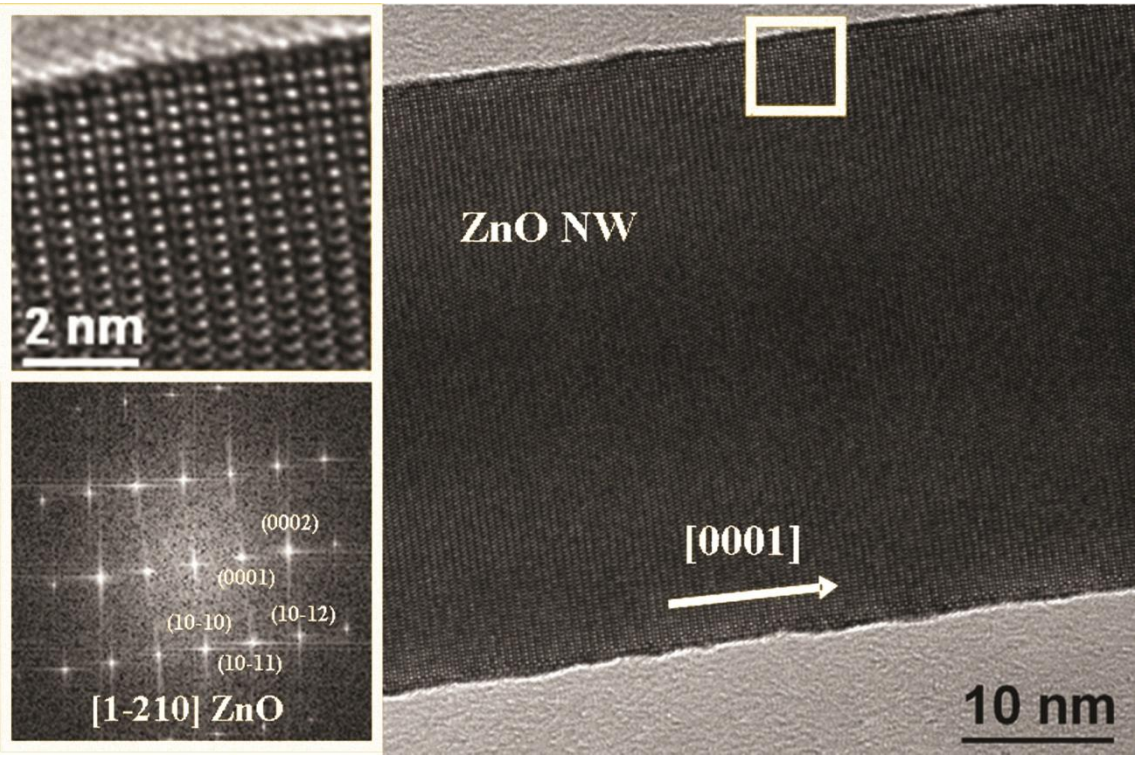

Figure 4-3: TEM and HR-TEM performed on the ZnO nanowires

XRD measurements were performed and the patterns showed ZnO nanowires with a hexagonal crystalline structure (figure 4-3) in accordance with ICDD card 00-036-1451. The major peaks can be indexed to the (002) as well as the (101) among other crystal planes. The intensities of the two peaks differ drastically, indicating strong preferential orientation of ZnO nanowires grown along specific crystal plane(s). Notably, the 101 reflection was fully diminished for nanowires grown over the r-plane. This implies preferable orientation in the <001> direction of nanowires. Also, it should be noticed that the peak at 33º in the r-plane XRD pattern (see figure 4-3) is originated from the substrate.

HR-TEM images joint with XRD pattern confirm the wurtzite-hexagonal structure and the single crystal character of our ZnO nanowires.

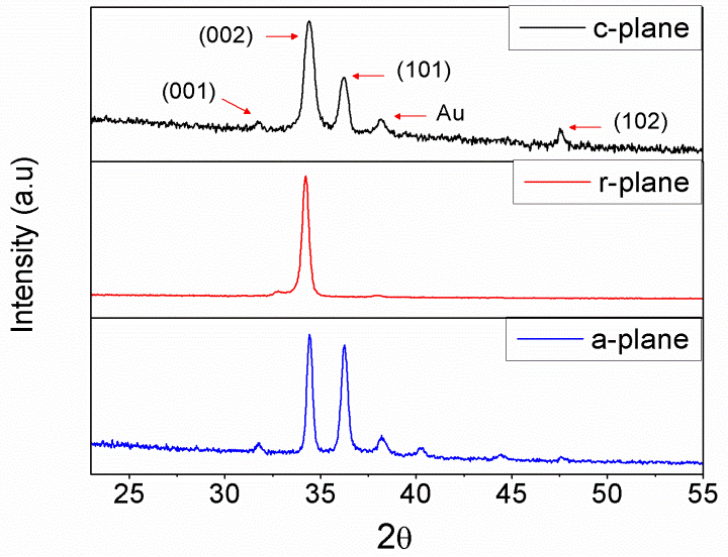

Figure 4-4: XRD pattern of the ZnO nanowires over the c-, r- and a- plane sapphire substrates.

4.2 In_2O_3 Octahedra

Nanostructured materials, such as ZnO nanowires obtained via VLS, have attracted attention over the past years, in an attempt to overcome some of the drawbacks found when sensing gases employing bulk materials. Nanomaterials show higher surface activity, superior responsiveness at lower operating temperatures (i.e. require lower power consumption) and superior long term stability than their bulk counterparts. Among all metal oxide semiconductors, indium oxide (In_2O_3) is one of the most important *n*-type, wide direct band-gap (around 3.6 eV at room temperature) semiconductor due to its excellent electronic and optical properties.

Many morphologies have been reported, including nanowires[15], nanofibers[16], nanotubes[17], nanoparticles, nanosheets, nano-flower like structures[18] among

many others. However, little has been reported about sensing properties of other polyhedral morphologies such as cubes, hexahedrons, octahedra and dodecahedrons[19]. The advantage of using morphologies like octahedra is that they possess sharp edges and tips, which will provide more active sites and smooth surfaces and unique and perfectly defined crystalline facets (i. e. (111)) exposed to the gas atmosphere.

Even though pure metal oxide sensors can be very responsive to some gases, they show often poor selectivity. To overcome this drawback, noble metal particles can be added to the surface of the metal oxide active layer, improving their sensitivity towards a given target gas. Noble metals such as Au[20], Pt[20] or Pd[21], are usually added to metal oxide nanostructures through a variety of methods, being RF sputtering one of the most commonly used. Its effectiveness has been demonstrated when used for functionalizing metal oxide nanomaterials[22,23].

4.2.1 Synthesis of In_2O_3 Octahedra

In_2O_3 octahedra were synthesized on top of Si/SiO_2 substrates via a vapor-phase transport method using a horizontal chemical vapour deposition (CVD) furnace. Si/SiO_2 substrates were previously cleaned by sonication. The cleaning process follows three steps of 5 minutes each in acetone, ethanol and deionized water, and then dried in synthetic air. In a typical experimental procedure, 0.3 g of high purity In metal (99.99%) were placed on an alumina boat. Next to it, at a distance of around 1 cm the Si/SiO_2 wafer was placed. Then, the alumina boat with the precursor and the wafer were placed at the

centre of the horizontal furnace. The temperature was raised to 1000ºC at a rate of 15ºC/min, and kept constant for 120 min. The reaction took place in a dynamic Ar atmosphere (300 mL/min). When the furnace was cooled down to room temperature, a pale green product was found on top of the Si/SiO_2 wafer. For TEM and HR-TEM analyses, a methanol dispersion of the sample was ultrasonicated for 20 minutes and a drop of it was deposited on a lacy carbon film supported by a nickel grid. For SEM analysis a product was scratched from the Si/SiO_2 substrate and placed on a carbon taped attached to an aluminum sample holder. Prior to the SEM investigation sample was coated with a 3 nm thick carbon layer.

In order to deposit Pt or Pd nanoparticles on In_2O_3 sensors, an RF sputtering system was used. For the Pt, 30 W and 8 s were used for the deposition and, for Pd, 50W and 8 s were used, both under 3.75 mTorr and room temperature. This process was conducted as a second step after the screen-printing of pure In_2O_3. The sputtering process parameters had been optimized previously for obtaining small and well dispersed Pt or Pd nanoparticles, avoiding coalescence of nanoparticles. It is not realistic to vary these parameters in view of altering the Pd or Pt loading, as that is not the only variable that changes: particle size changes as well. It has been shown previously that sensing performance in Pd/SnO_2 samples improves with decreasing Pd particle size[24]. The amount of metal loading employed in the In_2O_3 sensors was guided by the results showing that reducing the amount of metal sputtered reduced the size of metal nanoparticles.

The chemical characterization of the active layers was performed using X-ray photoelectron spectroscopy (XPS), the XPS analysis were carried out using a

Physical Electronics, VERSAPROBE PHI 5000 spectrometer equipped with a monochromatic AlKα radiation with 0.7 eV energy resolution and a dual-beam charge-compensation system. All the XPS data were elaborated using Casa XPS v.2.3 software and binding energies were referenced with respect to C 1s peak at 284.5 eV.

4.2.2 Characterization of In_2O_3 Octahedra

In_2O_3 nanostructures were synthesized via a vapor-solid mechanism, as indicated by the absence of metal catalyst on the substrate. After melting of In grains, In vapor reacts with residual oxygen present in the furnace, thus forming oxidized clusters. When the temperature further increases, the oxidized In clusters act as nucleation centers for the formation of In_2O_3 crystals. The formation of In_2O_3 nuclei will lead to the formation of the desired In_2O_3 morphology depending on the reaction temperature [25, 26]. At 700ºC, In_2O_3 triangular crystals are formed whereas at 800-1000ºC pyramids and octahedra can be obtained. The facets exposed correspond to the most energetically stable atomic planes in the lattice. Figure 4-5 shows FESEM images of the In_2O_3 octahedra synthesized at 1000ºC. As shown, the final product consists of a high density of octahedral shaped structures (figure 4-5, left). No other morphologies are observed, which indicates the uniformity of the process. A regular octahedron is composed of eight equilateral triangles, four of which meet at the same vertex. The side of each triangle is about 500 nm and all the faces are almost perfectly smooth and without any visible structural defects

(figure 4-5, right). Moreover, these structures possess sharp edges and vertexes.

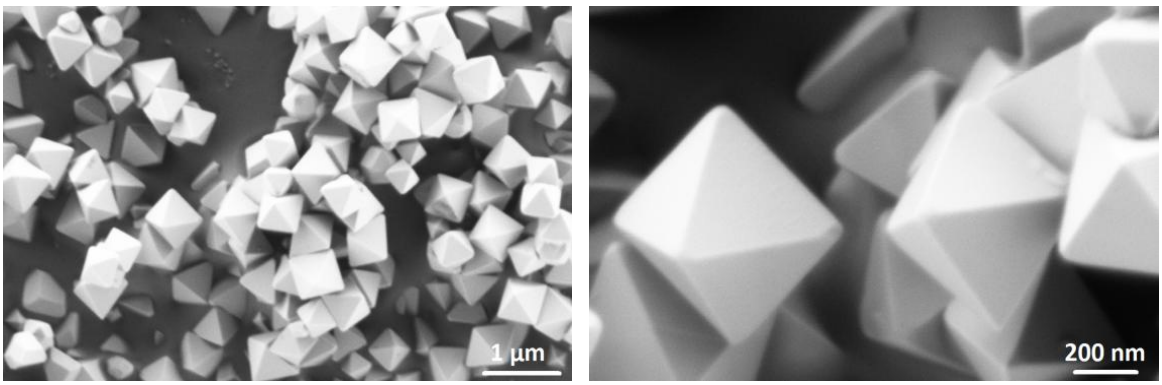

Figure 4-5: Low and high magnification ESEM images of the In_2O_3 octahedra.

Further characterization has been carried out using TEM and HRTEM. Figure 4-6 shows TEM and HRTEM images of the In_2O_3 octahedra. As observed, the side length of the octahedron is about 500 nm, which is consistent with what we observe in the FESEM images. The inset of figure 4-6 exhibits a HRTEM image of the edge of the ocahedron. It clearly exhibits the continuous lattice fringes of the structures, showing the crystalline nature of the In_2O_3 octahedra. The distance measured between two adjacent fringes is 0.29 nm, which corresponds to the {111}

interplanar distance of the cubic phase of In_2O_3 according to ICDD card nº 01-071-2194.

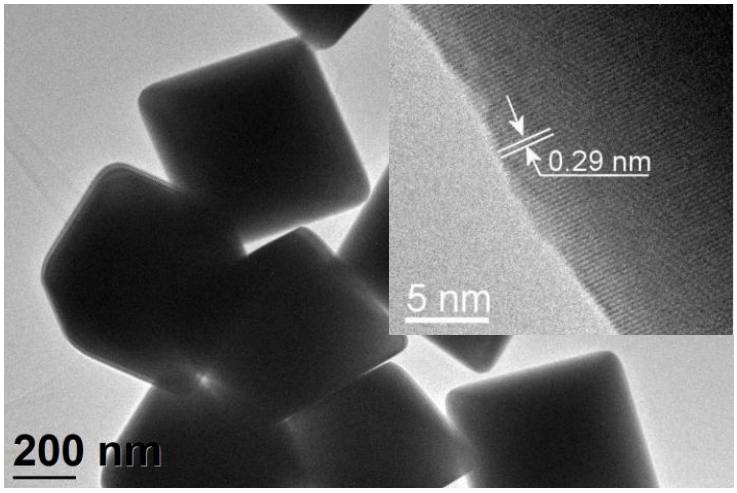

Figure 4-6: TEM and HR-TEM images of the In_2O_3 octahedra

An EDS taken over an area of several In_2O_3 octahedra confirms that there are no impurities present as no other peaks than those of indium and oxygen could be found (figure 4-7). The Ni and C peaks observed originate from the grid used to perform the EDS.

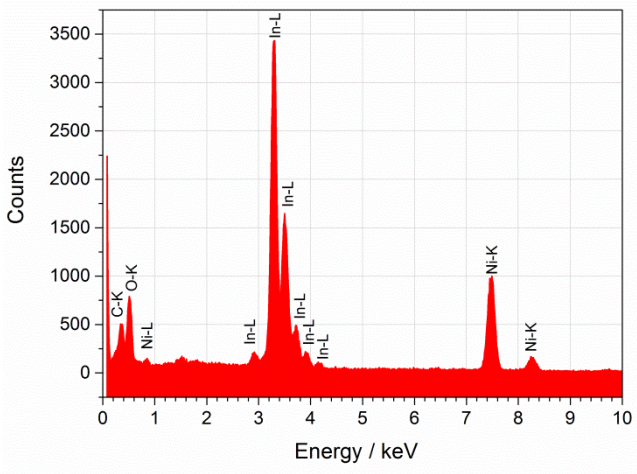

Figure 4-7: EDS taken on the In_2O_3 octahedra

Next, a characterization of the sputtering-deposited Pt and Pd nanoparticles on top of the In_2O_3 octahedra was carried out. HR-TEM images of the Pt and Pd nanoparticles are shown in figure 4-8 and 4-9 respectively. As shown, after the

deposition of Pt or Pd nanoparticles, the octahedral morphology was preserved. Furthermore, Pt nanoparticles appear homogenously distributed on the faces of the octahedra. The size of such nanoparticles is about 10–20 nm, as shown in figure 4-8. Closer inspection reveals that the measured interlayer distance is 0.26 thus corresponding to {111} interplanar spacing of PtO a cording to ICDD card nº 43-1100.

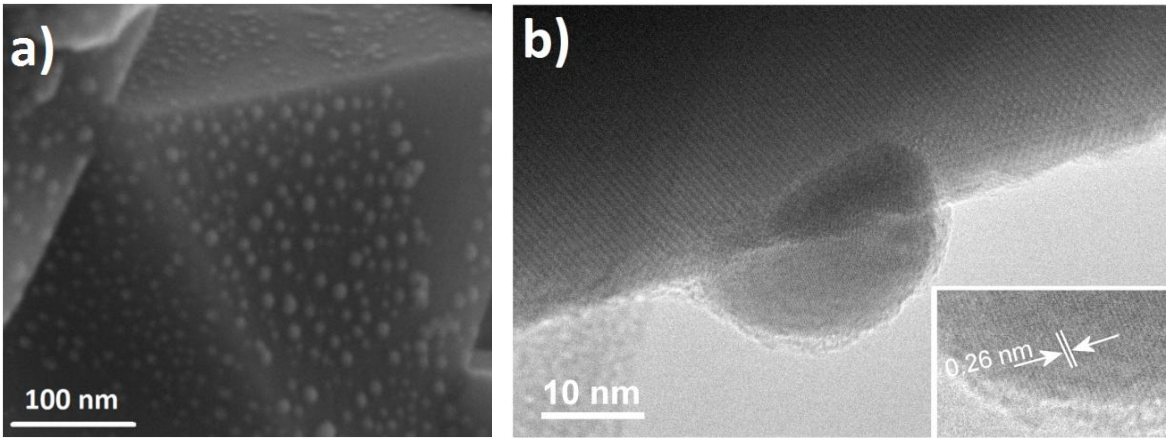

Figure 4-8: (a) FESEM image of the Pt/In_2O_3 octahedra, and (b) HR-TEM image a Pt nanoparticle attached to an In_2O_3 octahedron.

Analyzing the Pd decorated samples we can observe that the Pd nanoparticles are also homogeneously distributed along the faces of the In_2O_3 octahedra. In contrast to nanoparticles sputtered with a Pt target, these nanoparticles appear to be smaller, as their size ranges between 8 and 10 nm. Sch nanoparticles have an interplanar spacing of 0.259 and 0.263 nm. Such lattice parameters are close to the interplanar spacing of tetragonal PdO (d(111) = 0.263 nm and d(002) = 0.266 nm according to ICDD card nº 01-085-0624). In addtition, according to Kibis et al.[27] these values are characteristic for

highly oxidized palladium nanoparticles where palladium is mainly in the +2 oxidation state.

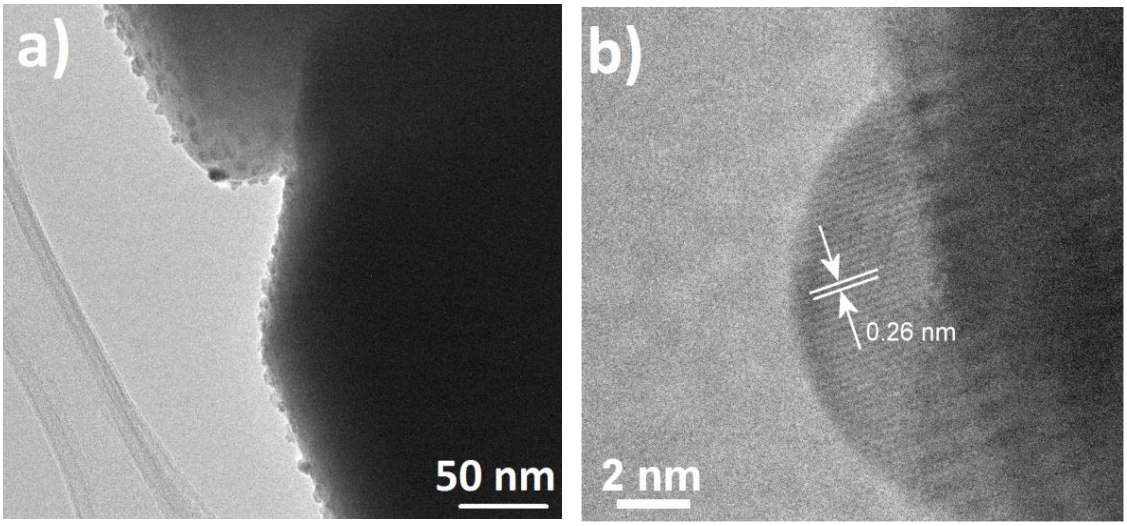

Figure 4-9: (a) HR-TEM image of the Pd/In_2O_3 octahedra, and (b) HR-TEM image a single Pd nanoparticle attached to an In_2O_3 octahedron.

The crystalline phase was confirmed by means of X-ray diffraction (XRD). As shown in figure 4-10, pure samples show the typical features of cubic In_2O_3. No peaks belonging to other materials or impurities could be found.

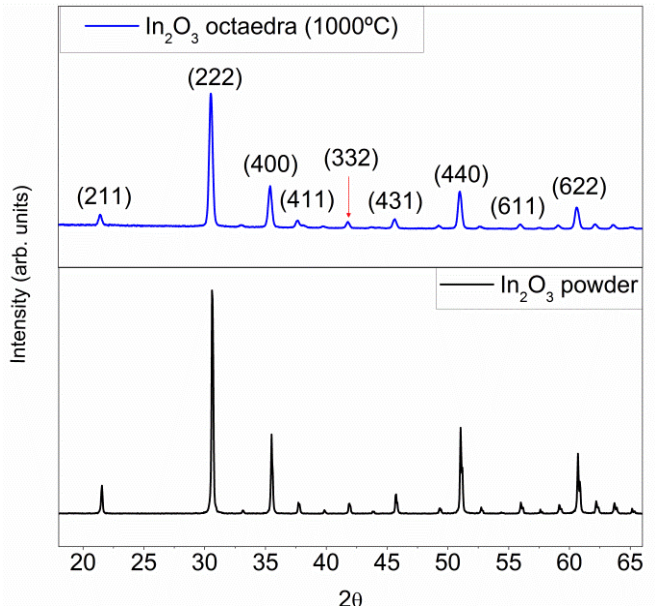

Figure 4-10: XRD pattern of the In_2O_3 octahedra compared to comercial In_2O_3

Additional XRD measurements for Pt and Pd-doped In_2O_3 samples were performed as shown in figure 4-11. These results confirm that metal decoration does not affect the crystallinity of In_2O_3 octahedra, which retain the cubic phase. Due to the low amount of metal loading, no peaks arising from Pt or Pd could be found. This is often the case for the typical amounts of metal loading used in gas sensing applications.[20, 28]

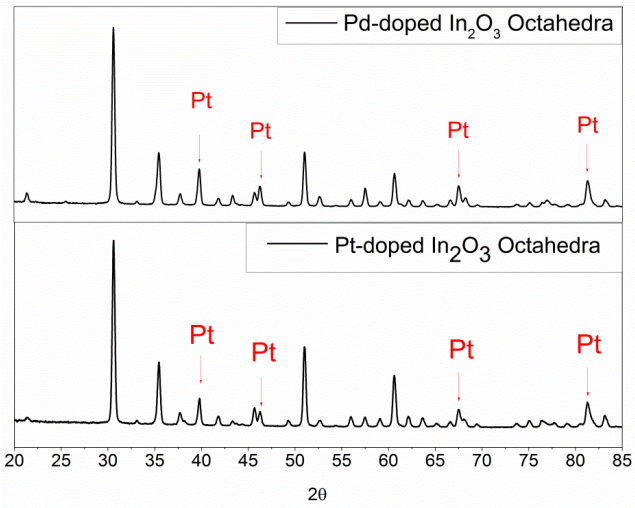

Figure 4-11: XRD pattern of the decorated samples with Pt and Pd

However, peaks arising from Pt can be found in both samples. However, these peaks do not come from the Pt nanoparticles. Their origin lies in the Pt electrodes of the substrates.

With the aim to identify the chemical state of elements in the indium oxide and in the catalyst particles (Pt, Pd), XPS analysis was carried out on the nanostructures deposited on the sensor substrates.

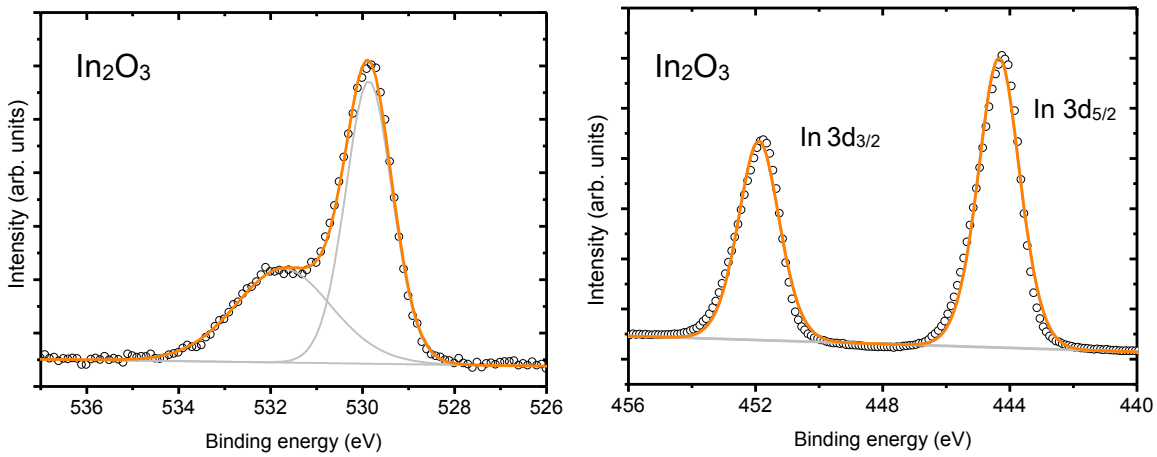

Figure 4-12: XP spectra of the pristine In_2O_3

The In 3d core level spectra of pristine In_2O_3 octahedra are shown in figure 4-12. As it is observed, it is composed of two components relative to the spin-orbit doublets ($3d_{5/2}$ and $3d_{3/2}$).

The In 3d core level spectra of the samples decorated with Pt and Pd nanoparticles are shown in figure 4-13. They are also composed of two components, relative to the spin-orbit doublets ($3d_{5/2}$ and $3d_{3/2}$) respectively at 444.2 eV and 451.8 eV indicating that In is mainly found in the +3 oxidation state, which corresponds to almost stoichiometric state[29]. If we compare the XP spectra of the pristine In_2O_3 octahedra and the decorated samples it can be observed no difference in the oxidation state of In.

The O 1s XP spectra are comprised of two intense peaks centred at 529.8 eV and 531.8 eV (figure 4-14). The more intense peak has been associated to oxygen bonds in In-O-In, while the high binding energy peak at 531.2 eV is possibly partially related to oxygen vacancies in the bulk of metal oxides[30].

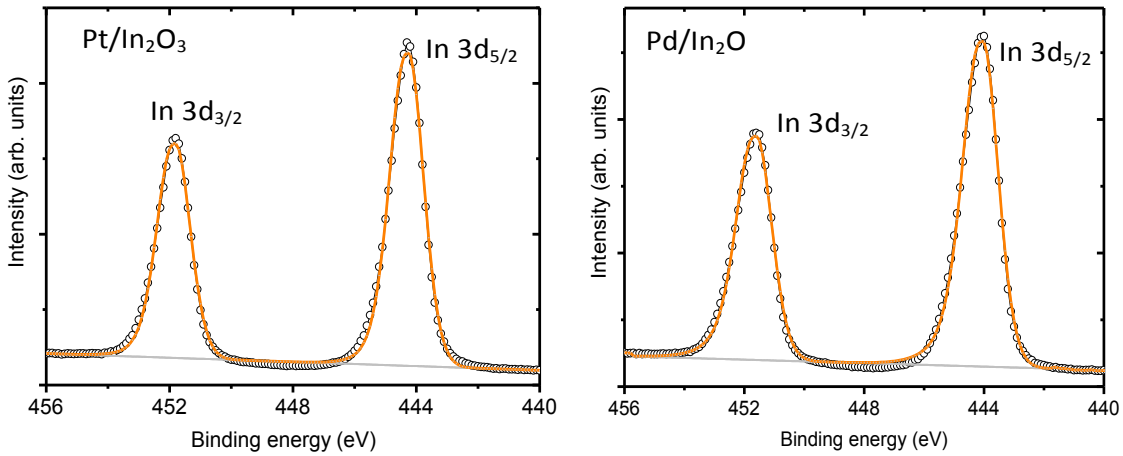

Figure 4-13: In 3d core level XP spectra of Pt/In_2O_3 and Pd/In_2O_3

Again, if we compare the peaks related to the O 1s of the pristine In2O3 octahedra (figure 4-12) and the decorated samples (figure 4-13), we see no difference whatsoever.

Inspecting the Pt 4f XP spectrum we observe two doublets (figure 4-15), one with the $4f_{7/2}$ component at 71.2 eV and the other at 72.5 eV. The existence of these two doublets suggests the presence of a core-shell structure with the low-binding energy doublet assigned to photoelectrons emitted from Pt atoms in the core of the particles, while the high-energy component is assigned to an oxidized shell. Assignment to a particular platinum oxide is complex as several intermediate oxidation states between PtO and PtO_2 have been reported to have peak positions in the range between PtO at 71.3 eV and PtO_2 at 74.1 eV[31].

Conversely, in figure 4-15 (right) the Pd $3d_{5/2}$ component at 336.2 eV clearly indicates the formation of PdO while the Pd $3d_{5/2}$ component at 335.1 eV indicates the presence of Pd0 [32]. Due to the small amount of Pt and Pd atoms deposited on the sample surface, the signal generated by photoelectrons

emitted from oxygen atoms bound to Pt appears in the background of the O 1s peak. If we compare the XPS results recorded on the metal decorated samples with the ones recorded on the pristine In_2O_3 samples (shown in figure 4-12), we observe that the decoration with metal nanoparticles has no influence in the oxidation state of the In_2O_3 octahedra.

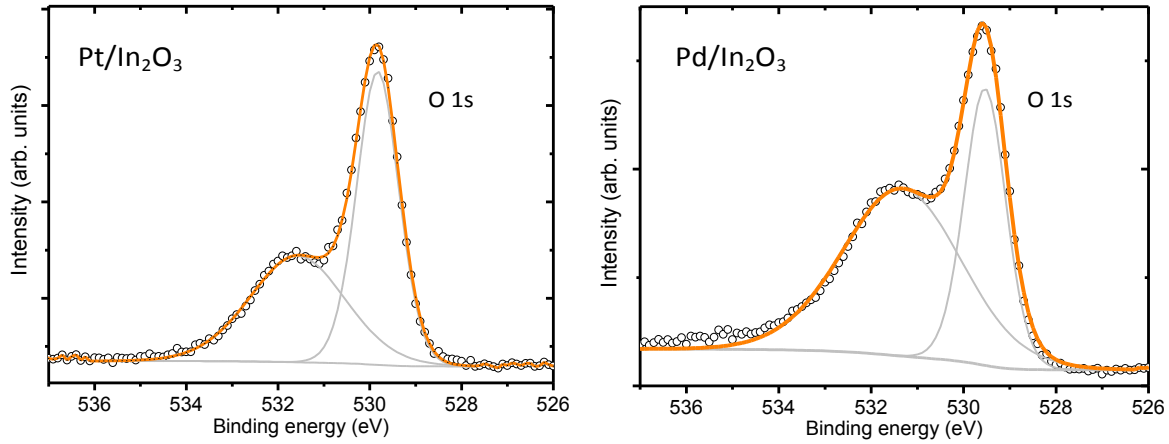

Figure 4-14: O 1s core level XP spectra of Pt/In_2O_3 and Pd/In_2O_3

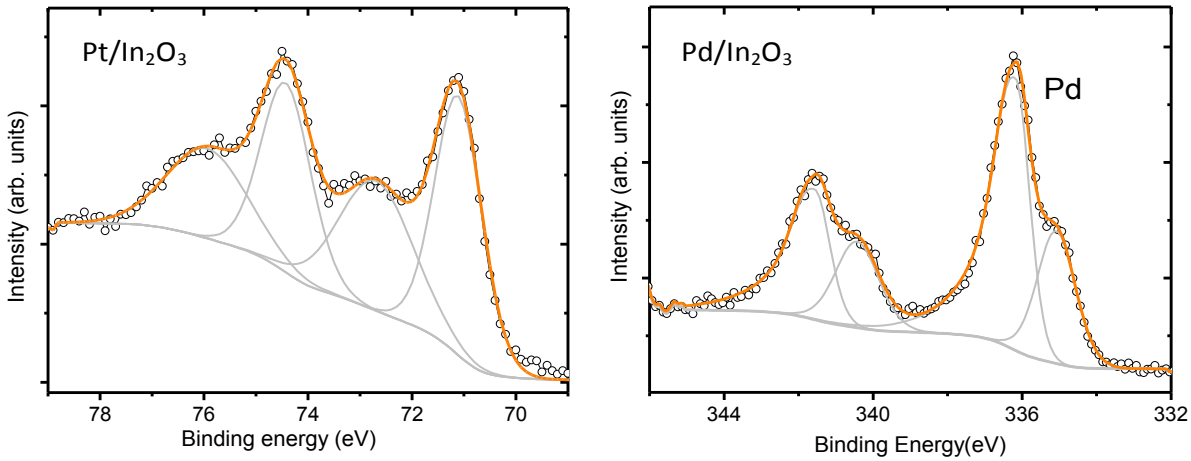

Figure 4-15: XP spectrum of Pt (4f) and Pd (3d) respectively

4.3 References

1. Wu, J. M.; Chen, Y.-R.; Lin, Y.-H., Rapidly synthesized ZnO nanowires by ultraviolet decomposition process in ambient air for flexible photodetector. *Nanoscale* 2011, *3* (3), 1053-1058.
2. Alenezi, M. R.; Henley, S. J.; Emerson, N. G.; Silva, S. R. P., From 1D and 2D ZnO nanostructures to 3D hierarchical structures with enhanced gas sensing properties. *Nanoscale* 2014, *6* (1), 235-247.
3. Law, M.; Greene, L. E.; Johnson, J. C.; Saykally, R.; Yang, P., Nanowire dye-sensitized solar cells. *Nat Mater* 2005, *4* (6), 455-459.
4. Fan, J.; Hao, Y.; Munuera, C.; García-Hernández, M.; Güell, F.; Johansson, E. M. J.; Boschloo, G.; Hagfeldt, A.; Cabot, A., Influence of the Annealing Atmosphere on the Performance of ZnO Nanowire Dye-Sensitized Solar Cells. *The Journal of Physical Chemistry C* 2013, *117* (32), 16349-16356.
5. Vanmaekelbergh, D.; van Vugt, L. K., ZnO nanowire lasers. *Nanoscale* 2011, *3* (7), 2783-2800.
6. Chu, S.; Wang, G.; Zhou, W.; Lin, Y.; Chernyak, L.; Zhao, J.; Kong, J.; Li, L.; Ren, J.; Liu, J., Electrically pumped waveguide lasing from ZnO nanowires. *Nat Nano* 2011, *6* (8), 506-510.
7. Cui, J., Zinc oxide nanowires. *Materials Characterization* 2012, *64* (0), 43-52.
8. Han, H. V.; Hieu, N. V.; Trung, T., A simple method for production of high aspect ratio ZnO nanowires with uniform structure for NO2 gas sensors. *Science of Advanced Materials* 2014, *6* (8), 1659-1667.
9. Jang, H.; Son, B.; Song, H.; Jung, G.; Ko, H., Controlled hydrothermal growth of multi-length-scale ZnO nanowires using liquid masking layers. *J Mater Sci* 2014, *49* (23), 8000-8009.
10. Güell, F.; Ossó, J. O.; Goñi, A. R.; Cornet, A.; Morante, J. R., Synthesis and optical spectroscopy of ZnO nanowires. *Superlattices and Microstructures* 2009, *45* (4–5), 271-276.
11. Weigand, C.; Tveit, J.; Ladam, C.; Holmestad, R.; Grepstad, J.; Weman, H., Epitaxial relationships of ZnO nanostructures grown by Au-assisted pulsed laser deposition on c- and a-plane sapphire. *Journal of Crystal Growth* 2012, *355* (1), 52-58.
12. Park, W. I.; Kim, D. H.; Jung, S.-W.; Yi, G.-C., Metalorganic vapor-phase epitaxial growth of vertically well-aligned ZnO nanorods. *Applied Physics Letters* 2002, *80* (22), 4232-4234.
13. Huang, M. H.; Mao, S.; Feick, H.; Yan, H.; Wu, Y.; Kind, H.; Weber, E.; Russo, R.; Yang, P., Room-Temperature Ultraviolet Nanowire Nanolasers. *Science* 2001, *292* (5523), 1897-1899.
14. Han, N.; Hu, P.; Zuo, A.; Zhang, D.; Tian, Y.; Chen, Y., Photoluminescence investigation on the gas sensing property of ZnO nanorods prepared by plasma-enhanced CVD method. *Sensors and Actuators B: Chemical* 2010, *145* (1), 114-119.

15. Wu, X. C.; Hong, J. M.; Han, Z. J.; Tao, Y. R., Fabrication and photoluminescence characteristics of single crystalline In2O3 nanowires. *Chemical Physics Letters* 2003, *373* (1–2), 28-32.
16. Liang, C. H.; Meng, G. W.; Lei, Y.; Phillipp, F.; Zhang, L. D., Catalytic Growth of Semiconducting In2O3 Nanofibers. *Advanced Materials* 2001, *13* (17), 1330-1333.
17. Shen, X.-P.; Liu, H.-J.; Fan, X.; Jiang, Y.; Hong, J.-M.; Xu, Z., Construction and photoluminescence of In2O3 nanotube array by CVD-template method. *Journal of Crystal Growth* 2005, *276* (3–4), 471-477.
18. Xu, X.; Wang, D.; Wang, W.; Sun, P.; Ma, J.; Liang, X.; Sun, Y.; Ma, Y.; Lu, G., Porous hierarchical In2O3 nanostructures: Hydrothermal preparation and gas sensing properties. *Sensors and Actuators B: Chemical* 2012, *171–172*, 1066-1072.
19. Shi, M.; Xu, F.; Yu, K.; Zhu, Z.; Fang, J., Controllable Synthesis of In2O3 Nanocubes, Truncated Nanocubes, and Symmetric Multipods. *The Journal of Physical Chemistry C* 2007, *111* (44), 16267-16271.
20. Yao, K.; Caruntu, D.; Wozny, S.; Huang, R.; Ikuhara, Y. H.; Cao, B.; O'Connor, C. J.; Zhou, W., Towards one key to one lock: catalyst modified indium oxide nanoparticle thin film sensor array for selective gas detection. *Journal of Materials Chemistry* 2012, *22* (15), 7308-7313.
21. Liu, L.; Zhang, T.; Li, S.; Wang, L.; Tian, Y., Preparation, characterization, and gas-sensing properties of Pd-doped In2O3 nanofibers. *Materials Letters* 2009, *63* (23), 1975-1977.
22. Vallejos, S.; Umek, P.; Stoycheva, T.; Annanouch, F.; Llobet, E.; Correig, X.; De Marco, P.; Bittencourt, C.; Blackman, C., Single-Step Deposition of Au- and Pt-Nanoparticle-Functionalized Tungsten Oxide Nanoneedles Synthesized Via Aerosol-Assisted CVD, and Used for Fabrication of Selective Gas Microsensor Arrays. *Advanced Functional Materials* 2013, *23* (10), 1313-1322.
23. Yamazoe, N.; Sakai, G.; Shimanoe, K., Oxide Semiconductor Gas Sensors. *Catalysis Surveys from Asia* 2003, *7* (1), 63-75.
24. Ma, N.; Suematsu, K.; Yuasa, M.; Shimanoe, K., Pd Size Effect on the Gas Sensing Properties of Pd-Loaded SnO2 in Humid Atmosphere. *ACS Applied Materials & Interfaces* 2015, *7* (28), 15618-15625.
25. Qurashi, A.; El-Maghraby, E. M.; Yamazaki, T.; Kikuta, T., Catalyst-free shape controlled synthesis of In2O3 pyramids and octahedron: Structural properties and growth mechanism. *Journal of Alloys and Compounds* 2009, *480* (2), L9-L12.
26. Gurlo, A., Nanosensors: towards morphological control of gas sensing activity. SnO2, In2O3, ZnO and WO3 case studies. *Nanoscale* 2011, *3* (1), 154-165.
27. Kibis, L. S.; Stadnichenko, A. I.; Koscheev, S. V.; Zaikovskii, V. I.; Boronin, A. I., Highly Oxidized Palladium Nanoparticles Comprising Pd4+ Species: Spectroscopic and Structural Aspects, Thermal Stability, and Reactivity. *The Journal of Physical Chemistry C* 2012, *116* (36), 19342-19348.
28. Annanouch, F. E.; Haddi, Z.; Vallejos, S.; Umek, P.; Guttmann, P.; Bittencourt, C.; Llobet, E., Aerosol-Assisted CVD-Grown WO3 Nanoneedles Decorated with Copper Oxide Nanoparticles for the Selective and Humidity-Resilient Detection of H2S. *ACS Applied Materials & Interfaces* 2015, *7* (12), 6842-6851.

29. Shinde, D. V.; Ahn, D. Y.; Jadhav, V. V.; Lee, D. Y.; Shrestha, N. K.; Lee, J. K.; Lee, H. Y.; Mane, R. S.; Han, S.-H., A coordination chemistry approach for shape controlled synthesis of indium oxide nanostructures and their photoelectrochemical properties. *Journal of Materials Chemistry A* 2014, *2* (15), 5490-5498.
30. Gan, J.; Lu, X.; Wu, J.; Xie, S.; Zhai, T.; Yu, M.; Zhang, Z.; Mao, Y.; Wang, S. C. I.; Shen, Y.; Tong, Y., Oxygen vacancies promoting photoelectrochemical performance of In(2)O(3) nanocubes. *Scientific Reports* 2013, *3*, 1021.
31. Blackstock, J. J.; Stewart, D. R.; Li, Z., Plasma-produced ultra-thin platinum-oxide films for nanoelectronics: physical characterization. *Appl. Phys. A* 2005, *80* (6), 1343-1353.
32. Hoflund, G. B.; Hagelin, H. A. E.; Weaver, J. F.; Salaita, G. N., ELS and XPS study of Pd/PdO methane oxidation catalysts. *Applied Surface Science* 2003, *205* (1–4), 102-112.

CHAPTER 5

Gas Sensing Measurements

In this chapter we report the results of the gas sensing measurements performed with the materials synthesized in the previous chapter that is ZnO nanowires and In_2O_3 octahedra. Several target gases have been measured including NO_2, H_2 and EtOH.

5.1 Gas Sensing Measurements of ZnO Nanowires

In order to measure the resistance of our sensors, silver (Heraeus, AD1688-06) parallel electrodes were deposited on top of the active layer. Substrates were glued to a hotplate in order to measure at different operating temperatures (i.e. sensors could be operated from room temperature up to 250°C).

Furthermore, these three ZnO NW samples were subject to gas sensing tests using an oxidizing gas (NO_2) and reducing vapour (EtOH) by means of DC resistance measurements at different operating temperatures (150-250°C). All sensors were exposed to 30 min of a given concentration of a species, followed by a 60 min cleaning phase in dry air. All sensors experienced an increase or decrease in resistance under exposure to oxidising or reducing gases, respectively. This implies that ZnO behaves as an n-type semiconductor. Figure 5-1 shows representative response/recovery cycles for the three sensors operated at 250°C against ethanol and nitrogen dioxide. The intensity of the response increased with gas concentration. Responses were reproducible in all cases. The baseline resistance could be fully recovered when cleaning in air after a sufficiently long time. The response time for all sensors is about 5 minutes and, even though the recovery time is longer, these times are still is in the same range than those reported for nanowire gas sensors[1,2]. Although

every sensor response does not reach complete stabilization (r-plane and c-plane), it is observed that the a-plane sensor does reach such stabilization. Taking this sensor as a reference the response and recover times have been calculated as the time that the sensor takes to achieve 90% of the total value of the response.

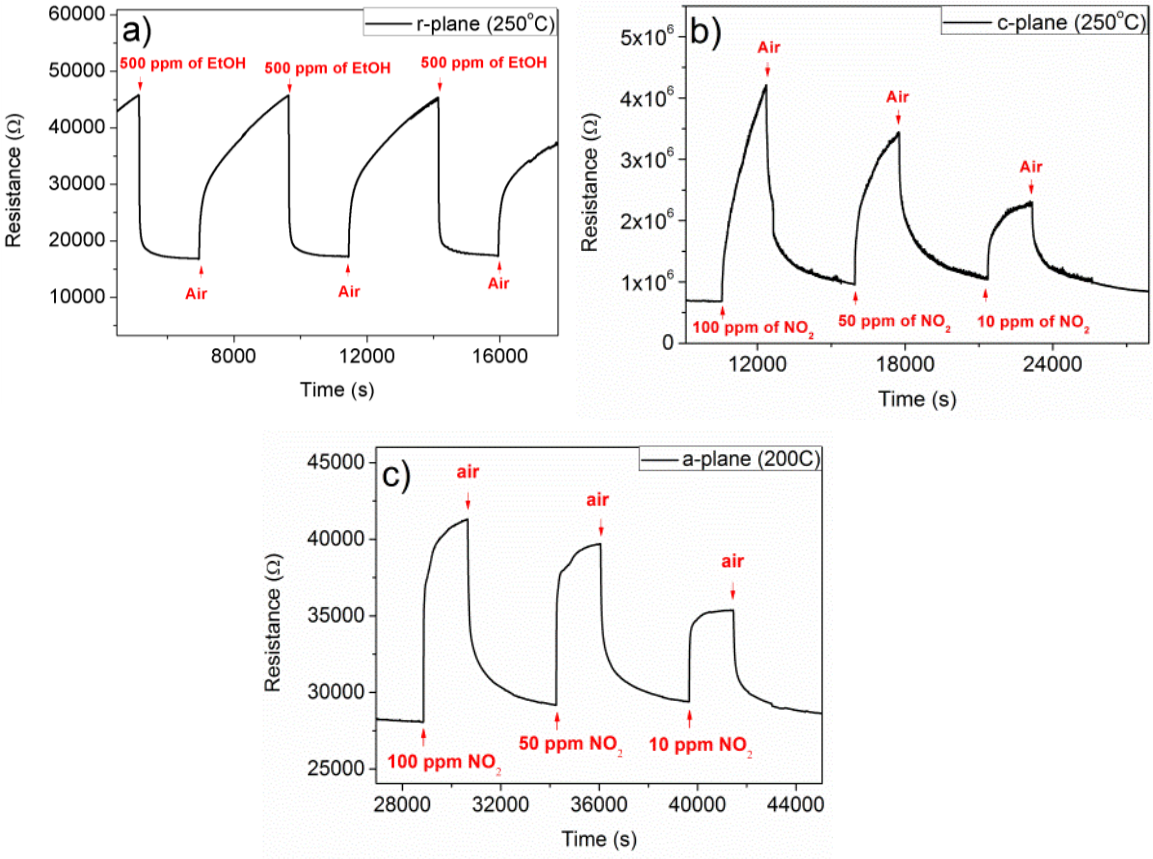

Figure 5-1: Responses of the three ZnO NW sensors to different gases: a) EtOH, b) and c) NO_2.

Figure 5-2 shows the dependence of sensor response as a function of the operating temperature at a fixed concentration of EtOH (500 ppm) and NO_2 (100 ppm). All three sensors showed the highest response when operated at 250ºC. Interestingly, for EtOH, the highest response was achieved by the a-plane sensor, whereas for NO_2 the highest response was that of the c-plane sensor.

Mechanistically, at first oxygen is physisorbed on the surface of the ZnO NW. Then, it becomes chemisorbed by attracting electrons of the conduction band, which forms a depletion region on the surface of the ZnO NWs and consequently a potential barrier between each nanowire, resulting in an increase in the resistance. It has been reported that EtOH can undergo various reactions such as dehydration and dehydrogenation. However, since ZnO is a basic oxide, dehydrogenation is favoured. In this case, the ethanol sensing mechanism is controlled by the change (i.e. lowering) in the equilibrium concentration of chemisorbed, negatively charged oxygen species, which results in a change in the width of the depletion region at the surface of the NWs[3].

In the case of NO_2 detection, either the equilibrium concentration of chemisorbed oxygen species is raised or NO_2 is directly chemisorbed on the surface of the n-type ZnO NWs [4]. These oxidizing molecules extract free electrons from the conduction band of ZnO and thus, the width of the depletion region is further extended, which increases the resistance of NWs.

According to the results presented in figure 5-2, the c-plane sensor presented the best response to NO_2 while the a-plane sensor exhibited the best response to EtOH vapours. In chemo-resistive sensors, there are many factors that influence sensor response. In addition to the morphology of the active surface structure, the presence of defects and their types can influence the electronic properties of materials and thus gas sensing properties. As a matter of fact, it is accepted that the overall response of gas sensors is a contribution both from the morphology of the material and the crystalline properties of the material itself[5]. Due to our set-up, we cannot increase the temperature further than

250ºC. Most likely at higher temperatures (i.e. >300ºC) the response will decrease. The reason behind such behaviour could be that the oxygen would not chemisorb on the active sites anymore and thus, the response of the sensor will dramatically decrease[6].

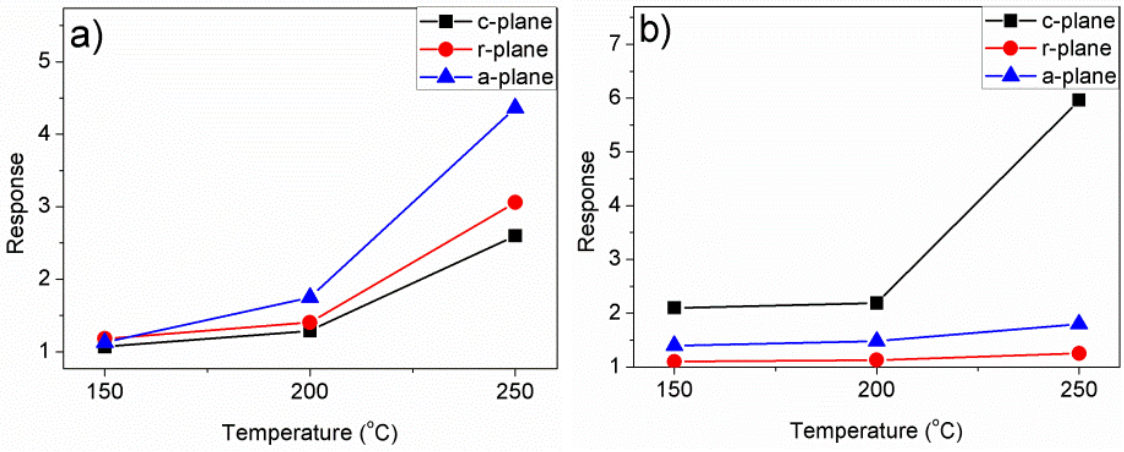

Figure 5-2: Temperature-dependent responses of the three sensors to a) EtOH and b) NO_2. Response was defined as R_{air}/R_{EtOH} and R_{NO2}/R_{air} respectively

5.1.1 Benzene Measurements with ZnO Nanowires

In addition to the NO_2 and EtOH measurements, some gas sensing tests have been performed with benzene (C_6H_6).

Benzene is a non-polar six-membered ring aromatic hydrocarbon with dimensions of ca. 6.0 x 3.5 Å and a volume of 120 Å^3. It is listed among the most harmful VOCs. It generates highly flammable and toxic vapours and it is recognized as a carcinogenic agent by the US Environmental Protection Agency and by the European Commission.

Benzene can be found in petrochemical industry, petroleum coke operations, and vehicle repair stations among others. Also, cigarette smoking is another source of exposure of benzene vapours.

The gas sensing measurements have been performed with the same conditions than those for NO_2 and EtOH. In figure 5-3 we can see an example of a response to the r- and c-plane samples to different concentrations of C6H6 at 150 and 200ºC respectively.

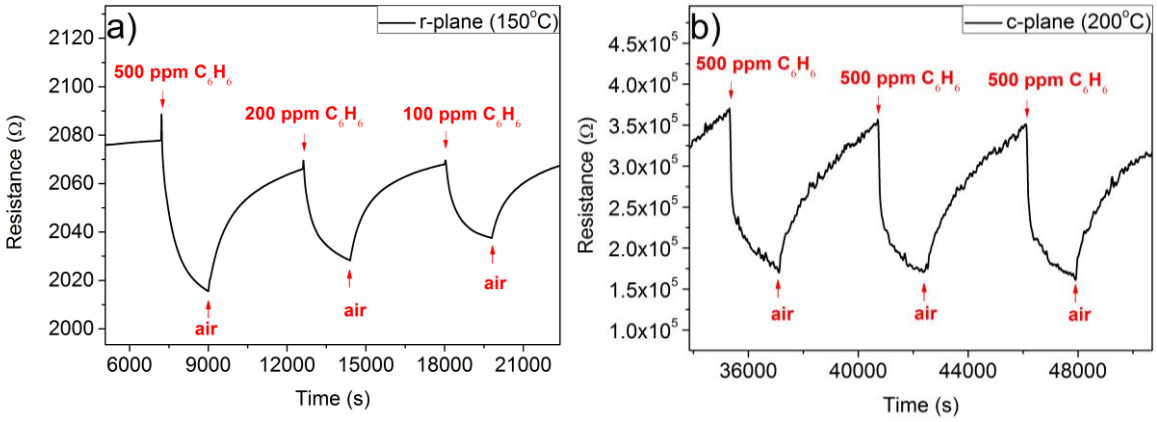

Figure 5-3: (a) Gas sensing measurements of the r-plane simple to different concentrations of C_6H_6 at 150ºC and (b) gas sensing measurements of the c-plane sample to 500 ppm of C_6H_6 at 200ºC

Figure 5-3 shows the response of the r- and c-plane sensors to different concentrations of benzene at 150 and 200ºC. As it can be seen, the signal to noise ratio is excellent.

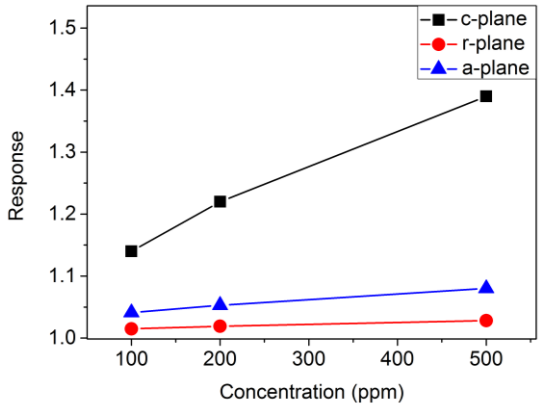

Figure 5-4: Concentration-dependent response of the three sensors to C_6H_6 at 150ºC

Figure 5-4 shows the calibration curves of the sensor for benzene when the operation temperature is set to 150ºC. Clearly the c-plane sample is the one which shows the highest response to benzene, the same that happened with NO_2.

Also, in figure 5-3b, it is shown the response of the c-plane sensor to 500 ppm of benzene.

These results show that our oriented ZnO nanowires could be a material that shows good potential for detecting benzene vapours in the ppm range.

5.2 Gas Sensing Measurements of In_2O_3 Octahedra

5.2.1 NO_2 Sensing Properties

After the material was scratched from the SiO_2 substrate in which it was growth and placed on top of an alumina substrate via screen printing, a 6 μm thick layer is obtained on top of the alumina substrate. A SEM micrograph (cross-sectional view) can be observed in figure 5-5.

Finally, the In_2O_3 octahedra samples were subject to gas sensing tests using oxidizing (NO_2) and reducing (H_2) gases by means of DC resistance measurements performed at different operating temperatures (100-250ºC). All sensors were exposed to 15 minutes of a given concentration of a species, followed by a 30 minutes cleaning phase in dry air. All sensors showed an increase or decrease in resistance under exposure to oxidizing or reducing gases, respectively. This implies that In_2O_3 behaves as an *n*-type semiconductor.

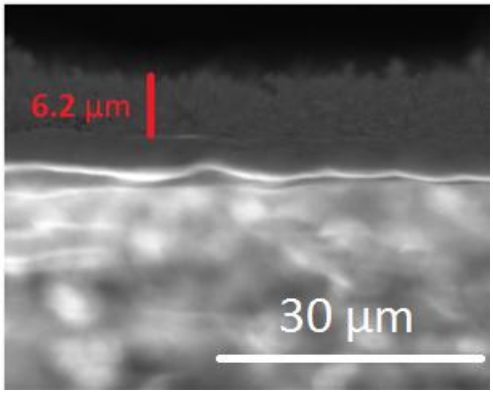

Figure 5-5: Cross-sectional image of the material layer on top of the alumina substrate

The typical response and recovery cycles of an In_2O_3 octahedra sensor toward increasing concentrations of NO_2 in dry air at 130ºC is presented in figure 5-6(a). It is well known that NO_2 is a very oxidizing gas and can be easily adsorbed on In_2O_3 structures, which leads to a decrease of the electron density of the In_2O_3 and thus, a decrease in the conductance.

The response and recovery time for all the concentrations is around 200 and 300 s respectively, which is in the range of the response and recovery time of other works of In_2O_3 material[7, 8]. Furthermore, the baseline resistance can be recovered after exposing the sensor to dry air, which shows that the sensor is completely reversible. Also, it is seen that the signal to noise ratio is excellent. Figure 5-6(b) shows the dependence of the In_2O_3 octahedra sensor as a function of different concentrations of NO_2 as a function of different operating temperatures.

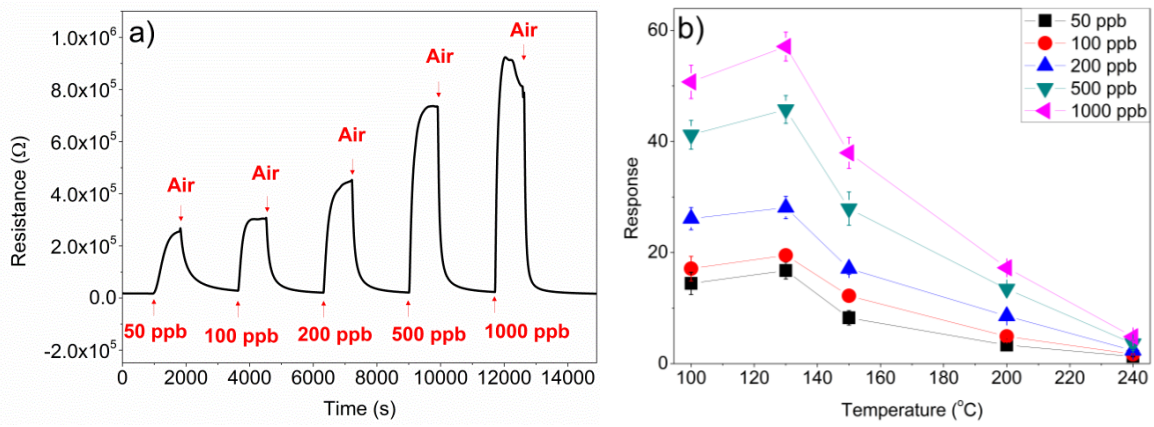

Figure 5-6: (a) Response of the In_2O_3 octahedra sensor at 130ºC and (b) performance of the sensor as a function of the temperature.

As shown in figure 5-6(b), sensors work at optimum when operated at a relatively low temperature of 130ºC. Comparing these results with those available in the literature for similar In_2O_3 structures, Mu et al.[9] reported a response that is 4 times lower with very slow response and recovery dynamics at room temperature for 100 ppb NO_2. Bloor et al.[10] reported a response that is 8 times lower at a much higher operating temperature (i.e. 400ºC). If we keep increasing the temperature, the performance sensors clearly worsen.

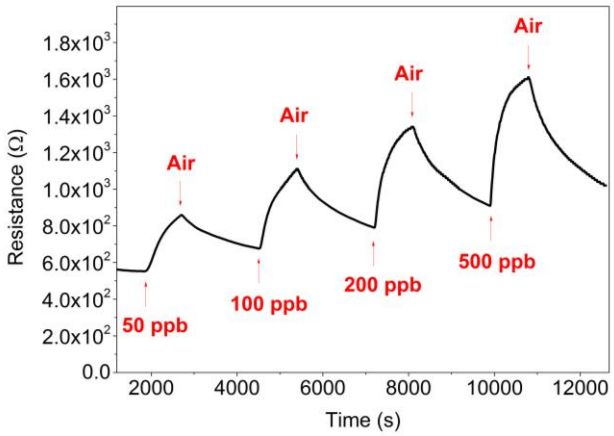

Figure 5-7: Response of the In_2O_3 octahedra sensor at room temperature

Moreover, gas sensing tests to low concentrations of NO_2 at room temperature have been performed. As shown in figure 5-7, the sensor achieves a response of R_{gas}/R_{air} = 2.46 when exposed to 200 ppb of NO_2 in air. This shows that our nanomaterials have potential for detecting oxidizing species even when operated at room temperature.

It is important to note that our sensors are able to detect NO_2 in the range of ppb with an excellent signal to noise ratio, which means that it is possible to detect even lower concentrations of this gas (the theoretical limit of detection can be estimated at units of ppb). A correlation between the logarithm of the sensor response and the concentration was easily obtained and it is shown in figure5-8(a). As observed, a linear fit can be obtained from the response as a function of the concentration of NO_2, with an r-square near 0.99 in all the cases.

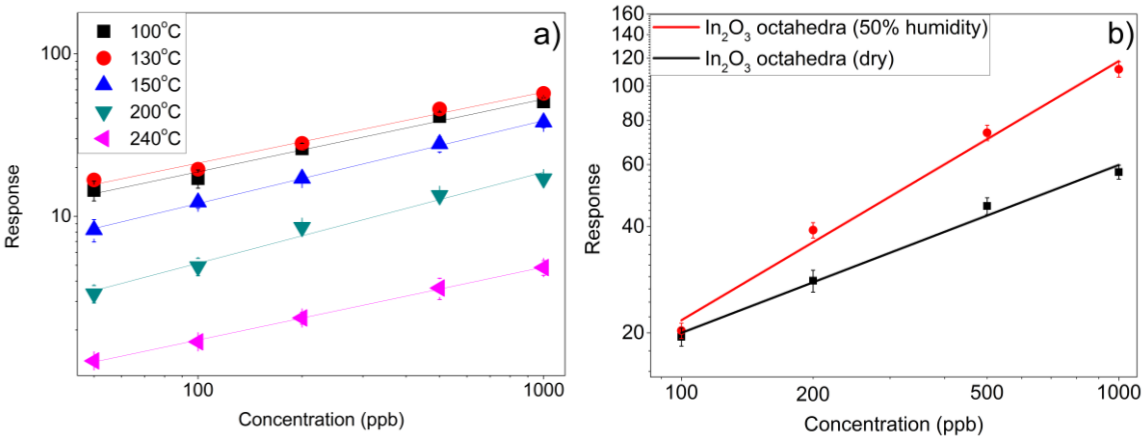

Figure 5-8: (a) Response of the In_2O_3 octahedra sensor as a function of NO_2 concentration and (b) performance of the sensor at 130ºC under humid conditions (50% R.H. at 22ºC).

Furthermore gas sensing performance of an In_2O_3 octahedra sensor under humid conditions was examined by exposing it to NO_2(g) in a background of air at 50% relative humidity (at 22ºC) and the response was compared to that

under dry conditions. The sensitivity towards NO_2 (the slope of the red curve in figure 5-8(b) under humid conditions is significantly higher than that under dry conditions (the slope of the black curve in figure 5-8 (b).

We can compare the performance of our sensor with the performance of a sensor made of commercial In_2O_3 (Sigma-Aldrich 99.99%). Sensor made of commercial In_2O_3 was fabricates in the same way than the In_2O_3 octahedra sensor, that is deposited by screen printing. The response of the commercial sensor to different concentrations of NO_2 and at different temperatures can be seen in figure 5-9.

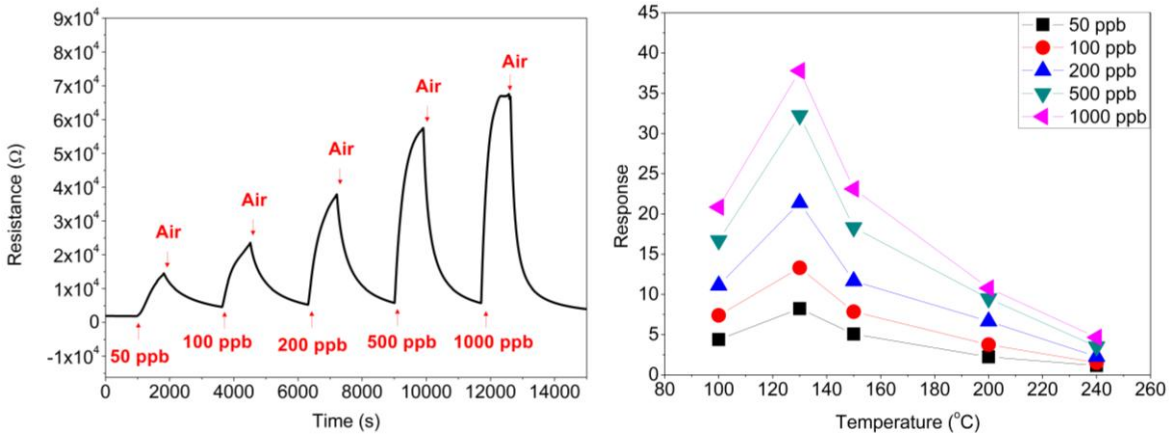

Figure 5-9: (a) Response of the commercial In_2O_3 sensor at 130ºC and (b) performance of the sensor as a function of the temperature.

As one can see the performance of the sensor is way better for the In_2O_3 octahedra sensor than for the commercial In_2O_3 sensor. Furthermore, the optimum working temperature of the commercial In_2O_3 is the same than for the In_2O_3 octahedra sensor i.e 130ºC. A direct comparison between these two sensors can be observed in figure 5-10.

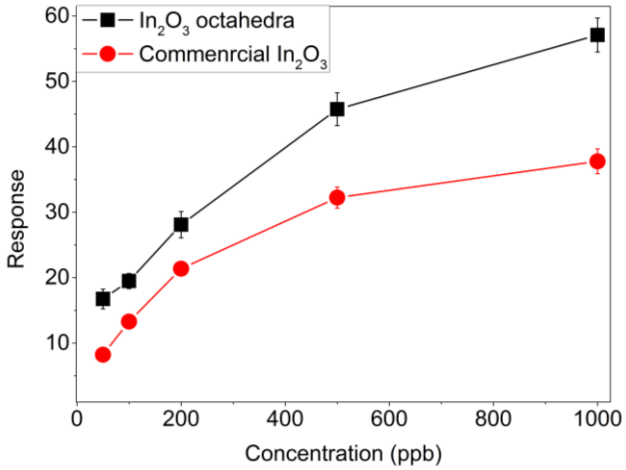

Figure 5-10: Comparison between In_2O_3 octahedra sensor and commercial In_2O_3 sensor

Also, the performance of Pt and Pd-doped In_2O_3 octahedra sensors were examined under dry conditions. The responses obtained were extremely low compared to the response of pure In_2O_3 octahedra sensors at the optimum working conditions as presented in Table 5-1.

Table 5-1: Comparison between the responses of pure, Pt and Pd-doped In_2O_3 octahedra towards 200 ppb of NO_2 at 130ºC. The response was calculated as $S = R_g/R_a$

Concentration of NO_2	Pure In_2O_3 octahedra	Pt-doped In_2O_3 octahedra	Pd-doped In_2O_3 octahedra
200 ppb	30	3.1	1.2

The sensing mechanism of semiconductor materials consists of two steps: The first one is the receptor function which involves the recognition of the species through a gas-solid interaction, and the second one is the transduction function which involves the change in the electrical resistance of the sensor[11]. At low operating temperatures (i.e., lower than 130ºC), when In_2O_3 octahedra are exposed to $NO_2(g)$, the gas becomes ionosorbed on the surface of the

material due to its high electrophilic properties, resulting in an increase of the overall resistance of the sensor:

$$NO_{2(gas)} + e^- \rightarrow NO^-_{2(ads)}$$

The rapid decrease in the response of the sensor at temperatures higher than 130ºC can be explained be the decreasing number of active sites for the adsorption of NO_2 molecules. At higher temperatures, the amount of oxygen molecules adsorbed is greatly increased and as a consequence, the number of free active sites suitable for the adsorption of NO_2 molecules is reduced. Therefore, the response of the sensor is sharply decreased. The presence of Pt or Pd nanoparticles on the surface of In_2O_3 favours, via a chemical sensitization, the increase in the number of adsorbed oxygen species at the surface of the metal oxide[11]. This, once more, significantly reduces the number of active sites for the adsorption of NO_2 and explains the dramatically reduced NO_2 response observed for metal decorated samples.

Regarding the measurements under humid conditions shown in figure 5-8(b), at moderate operating temperatures (i.e. ≤ 200ºC), the interaction of ambient moisture with different metal oxide surfaces can be summarized as follows. The interaction with water vapour results in an increase of bridging hydroxyls and the formation of terminal hydroxyl groups[12, 13]. Also, dissociative adsorption of water takes place on surface metal atoms (S_{lat}) giving rise to terminal OH groups. Assuming the dissociation of water molecules, hydroxyl surface groups are formed:

$$H_2O^{gas} + S_{lat} + O_{lat} \leftrightarrow \left({S_{lat}}^{+} - OH^{-}\right) + (O_{lat}H)^{+} + e^{-}$$

In addition to the ionosorption of NO_2 on the surface of the metal oxide, the following interaction mechanism might be possible between NO_2 and the terminal hydroxyl groups[14]:

$$NO_2^{gas} + \left({S_{lat}}^{+} - OH^{-}\right) + (O_{lat}H)^{+} + 2e^{-} \leftrightarrow (S_{lat} - NO_2^{-}) + H_2O^{gas} + {O_{lat}}^{-}$$

As a consequence, additional electrons are trapped via the conduction band of the metal oxide material, leading to an increase in NO_2 response under humid air conditions.

5.2.2 H_2 Sensing Properties

Furthermore, gas sensing properties of the In_2O_3 octahedra against a reducing gas such as H_2 were investigated. The experiments were performed in the same conditions as those previously described for NO_2. Figure 5-11(a) shows the response of a sensor to low concentrations of H_2 at 200ºC. The sensor resistance decreases with increasing H_2 concentration, which is in agreement with the behaviour of an *n*-type semiconductor exposed to a reducing gas. As in the case of NO_2 sensing, the signal to noise ratio is excellent for H_2 sensing, and the sensor will be able to detect concentrations in the ppb range (the theoretical limit of detection for hydrogen is in the tens of ppb range).

In contrast to NO_2 sensing, the optimal operating temperature is higher for H_2 sensing. The best performance of the sensor is found at the highest examined

temperature of 250ºC (figure 5-11(b)). This suggests that we can make the sensor more selective to a target gas by properly choosing an operating temperature; low temperatures (e.g. 130ºC) will be optimal for NO_2 detection, while higher temperatures (e.g. 250ºC) are suited for H_2 detection. When operated at 130ºC and in a humid background, the sensor is very selective to selective oxidizing species because its response to 1 ppm NO_2 is more than two orders of magnitude higher than its response to 1 ppm H_2. When operated at 250ºC, the sensor becomes responsive to hydrogen. However, its response to nitrogen dioxide, although significantly decreases, remains of the same order of magnitude than that of hydrogen.

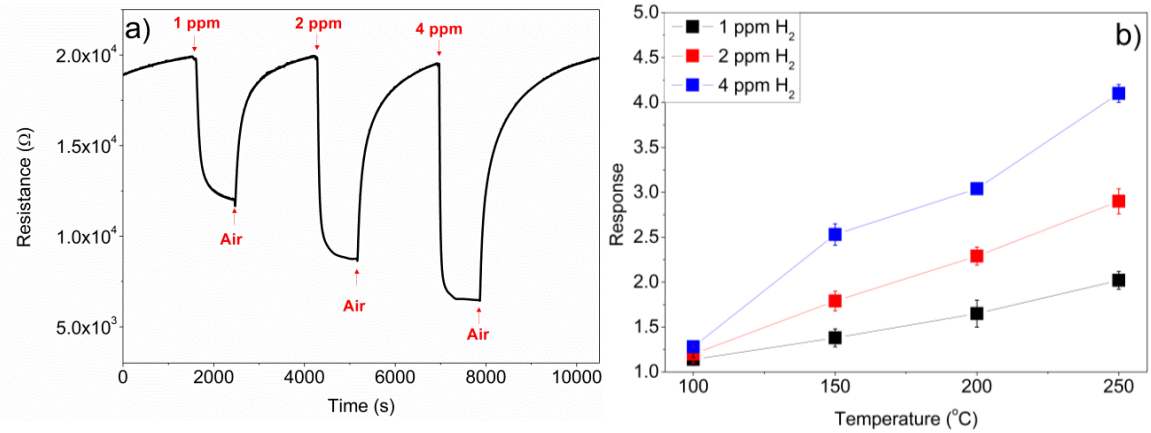

Figure 5-11: (a) Response of the In_2O_3 octahedra sensor to different concentrations of H_2 at 200ºC, and (b) response of the sensor as a function of the temperature.

A possible approach to increase the sensitivity of In_2O_3 octahedra sensors to reducing gases like H_2 is to load In_2O_3 with different noble metal nanoparticles. In this work, Pt and Pd nanoparticles have been chosen because they are well-known sensitizers for hydrogen detection in metal oxides.[20, 15]

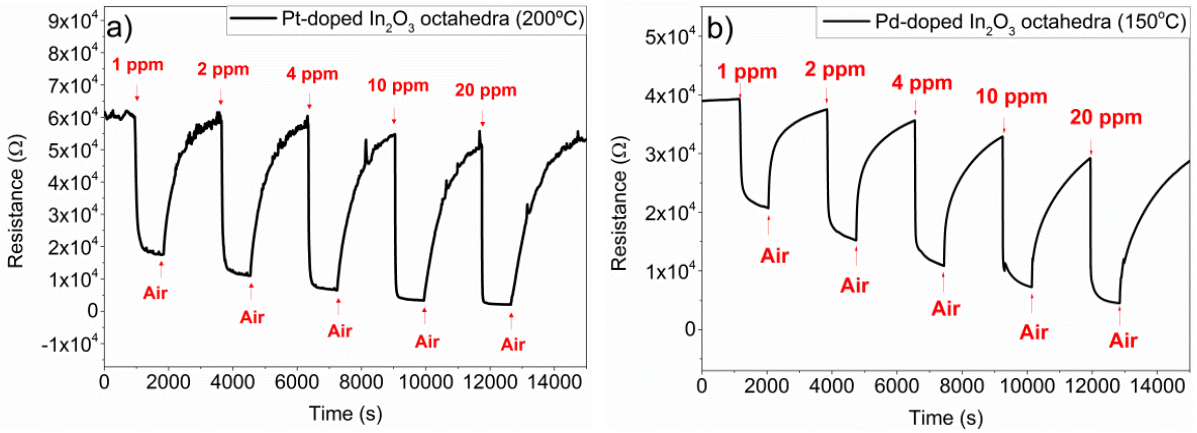

Figure 5-12: (a) Response of the Pt-doped In_2O_3 octahedra sensor to different concentrations of H_2 at 200ºC, and (b) response of the Pd-doped In_2O_3 octahedra to different concentrations of H_2 at 150ºC

Figure 5-12 shows the response of the decorated samples (with Pt and Pd) to several concentrations at 150 and 200ºC.

The lack of complete baseline recovery in both cases (worsens if the operating temperature is lowered) implies that the dynamics of sensor recovery are lower for H_2 than for NO_2.

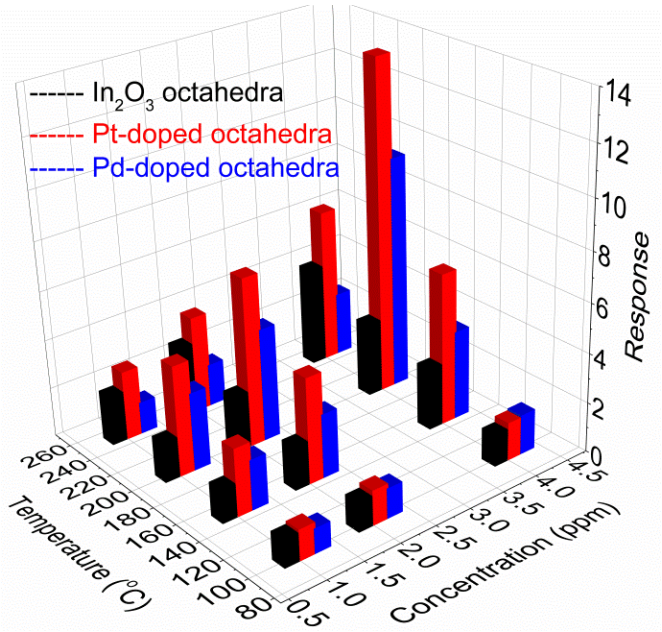

Figure 5-13: Performance of the undoped and Pt/Pd-doped In_2O_3 octahedra sensors as a function of the operating temperature for H_2.

Figure 5-13 shows the comparison between pure In_2O_3 octahedra and Pt/Pd-doped In_2O_3 octahedra for H_2 sensing. Both dopants improve the sensing characteristics of pure In_2O_3 octahedra. Particularly, it is easily observed that the best response in terms of H_2 sensing is achieved with the Pt-doped In_2O_3 octahedra with the optimum temperature of 200ºC, lower than that of pure In_2O_3 octahedra. Recalling that metal loading resulted in a very significant decrease in sensitivity to nitrogen dioxide Pt loading, in contrast, facilitates the selective detection of H_2.

Moreover, the performance of Pt-doped In_2O_3 sensors operating in a humid background has been tested. The sensors operated at 200ºC were exposed to different concentrations of H_2 gas (1, 2, 4, 10 and 20 ppm) in a background of air at 50% relative humidity (at 22ºC) as shown in figure 5-14. The sensor under 50% humidity conditions shows significantly lower sensitivity (0.44 ppm^{-1}) than that of the sensor in dry conditions (0.72 ppm^{-1}).

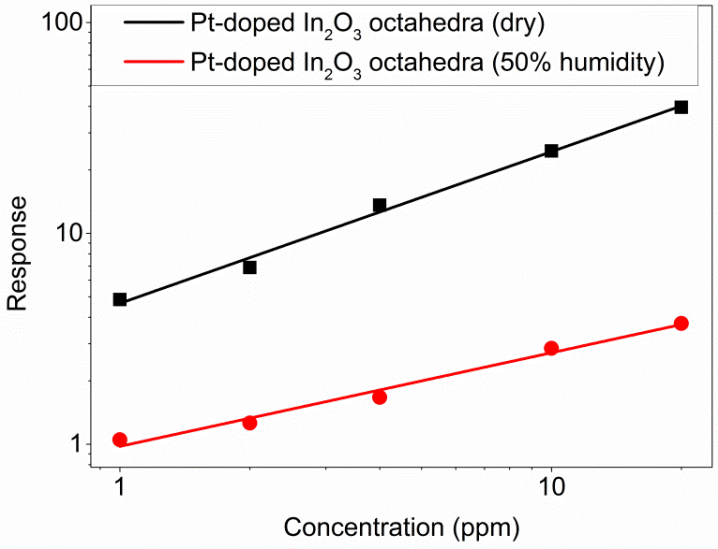

Figure 5-14: Comparison between the responses of the Pt-doped sensor in dry and humid conditions at 200ºC.

Also, the response to H_2 at 250ºC of Pt-In_2O_3 octahedra sensors is one order of magnitude higher than that of the same sensors to NO_2 gas, as it can be deduced from table 1. In other words, sensors become selective to reducing species (e. G. H_2) by increasing the operating temperature and decorating the material with noble metal nanoparticles such as Pt.

It is generally accepted that reducing gases change surface conductivity due to a change in the oxidation state of the material. The fact that there is a sharp decrease in the response of the Pt-doped In_2O_3 sensor when exposed to H_2 gas with a 50% of relative humidity can be explained as follows: At relatively low temperatures, both H_2 and H_2O vapours interact in the same way with the surface of the material; that is creating new OH groups and consuming the bridging oxygen atoms. As a consequence, the combined interaction of hydrogen and water vapours with the surface becomes competitive[12]. Therefore, the response of the sensor is greatly decreased as shown in figure 5-14.

As previously stated, the sensing mechanism of n-type sensors is based on the variation of the electrical resistance of the sensing element, which depends basically on the gas atmosphere, the operating temperature and morphology of the sensing material among other factors. When the sensor is exposed to dry air, oxygen molecules adsorb on the surface of the material, capturing electrons of the conduction band. This creates a depletion layer derived from the adsorbed oxygen. As H_2 is introduced in the measurement cell, the H_2 molecules react with the chemisorbed oxygen, releasing an electron back to the semiconductor and thus, reducing the resistance of the sensor[12]:

$$H_2 + O^- \rightarrow H_2O + e^-$$

However, we have experimentally seen that modifying the bare oxide with noble metal nanoparticles, greatly enhances the response towards reducing gases. In this case, the gas-solid interaction that involves the receptor function is the catalytic oxidation of the target gas over the grain surface. When H_2 molecules are in contact with the metal nanoparticles, they dissociate into H atoms that can spill-over to the semiconductor surface to react with the adsorbed oxygen. Therefore, the addition of the metal nanoparticle favours the reaction of the target gas with the semiconductor oxide via a catalytic oxidation (chemical sensitization). In that way, the metal additive facilitates the interaction between the gas species and the semiconductor oxide. This type of interaction occurs mainly in the Pt-doped sensors[11].

In a different mechanism, the metal additive in the oxidized state acts as a strong electron acceptor from the oxide creating a space charge layer. Then, when the additive is reduced when it makes contact with the target gas, it relaxes the space charge layer by giving back the electrons to the semiconductor oxide. This type of interaction is named electronic sensitization and it occurs with noble metals like Pd. When Pd is exposed to dry air, it forms a stable metal oxide (PdO) that interacts with the In_2O_3 octahedra. When in contact with H_2, they are converted back to the metallic state (Pd) resulting in the disappearance of the electronic interaction with the In_2O_3[15]. Results of the XPS analysis performed over the samples and shown in figure 4-15, confirm the presence of PtO and PdO on our sensors.

The reason why the response of the Pd-doped sensor is lower than the response of the Pt-doped one might be because the behaviour of the latter is a

combination of the chemical sensitization and the electronic sensitization stated above.

In addition to the above-discussed chemical and electronic sensitization mechanisms, sensor response is also influenced by the amount of metal loading. However, the sputtering process was conducted in order to obtain nanoparticles with near to optimal sizes, according to previous studies[16,15].

5.2.3 Selectivity Study of the Sensors

To further study the selectivity, all sensors were exposed to CO, EtOH, H_2S, H_2 and NO_2, as shown in figure 5-15.

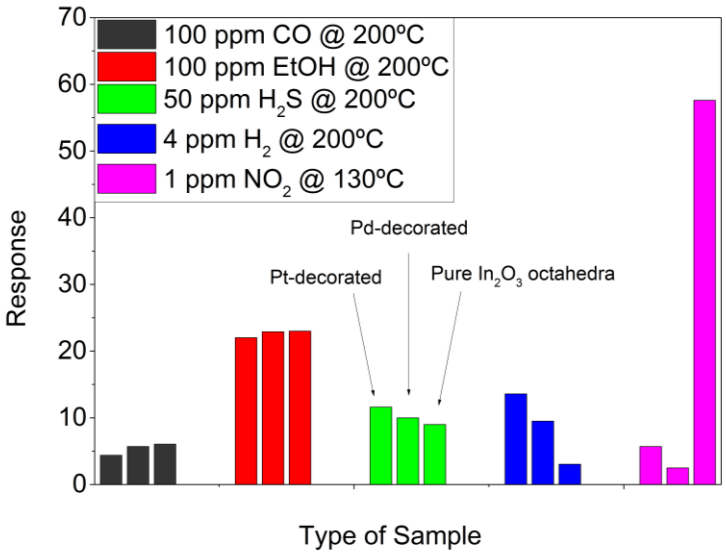

Figure 5-15: Comparison between the responses of the Pt-doped, Pd-doped and pure In_2O_3 octahedra to several gases. Each colour represents a different gas. For each set of columns, the left one represents Pt-decorated In_2O_3 octahedra, the middle one represents Pd-decorated In_2O_3 octahedra and the right one represents pure In_2O_3 octahedra

In figure 5-15, one can see the response of the three types of materials exposed to several gases/vapours at their optimum working conditions. As observed, the best response is obtained for the pure In_2O_3 octahedra exposed

to NO_2 at a relatively low temperature (130ºC). Furthermore, it is also observed a good response to ethanol vapours. However, the sensing temperature is much higher than that for NO_2 and the concentration is two orders of magnitude higher.

If we focus only on reducing species, we can see that at the same working temperature (200ºC), Pt-decorated sensors are able to detect 4 ppm of H_2 with a good response, if we take into account that hydrogen concentration is nearly two orders of magnitude lower than that of EtOH, CO and H_2S.

These significant differences revealed by this study suggest that engineering the morphology and the crystallinity of the material can be really useful and need for further research, since it may become an effective strategy to enhancing the sensitivity and selectivity of In_2O_3 sensors.

All in all, we can say that pure In_2O_3 octahedra are excellent for detecting NO_2 gas with an outstanding sensitivity (0.43 ppb^{-1}) at low temperatures (130ºC), while the response to H_2 remains two orders of magnitude lower under the same conditions. In addition, the presence of humidity increases the sensitivity to NO_2 and, at the same time, reduces the response to H_2, which results in an increased selectivity. This makes our sensor an excellent candidate to detect, in a selective way, oxidizing gases such as NO_2 at low operating temperatures, even showing potential for room temperature operation, with an excellent sensitivity even in the presence of humidity.

Furthermore, increasing the operating temperature and loading the octahedra with Pt, results in the quenching of the response to NO_2 and in an increase in the response towards H_2. In this way, one can make the sensor more selective

to reducing gases such as H_2. However, in this case the presence of ambient humidity negatively influences the response of the sensor.

As a consequence, our nanomaterial can be made selective to oxidizing or reducing gases by varying the operating temperature and by metal loading.

5.3 References

1. Hernandez-Ramirez, F.; Prades, J. D.; Tarancon, A.; Barth, S.; Casals, O.; Jimenez-Diaz, R.; Pellicer, E.; Rodriguez, J.; Morante, J. R.; Juli, M. A.; Mathur, S.; Romano-Rodriguez, A., Insight into the Role of Oxygen Diffusion in the Sensing Mechanisms of SnO2 Nanowires. *Advanced Functional Materials* 2008, *18* (19), 2990-2994.
2. Prades, J. D.; Jimenez-Diaz, R.; Hernandez-Ramirez, F.; Barth, S.; Cirera, A.; Romano-Rodriguez, A.; Mathur, S.; Morante, J. R., Ultralow power consumption gas sensors based on self-heated individual nanowires. *Applied Physics Letters* 2008, *93* (12), 123110.
3. Xu, J.; Han, J.; Zhang, Y.; Sun, Y. a.; Xie, B., Studies on alcohol sensing mechanism of ZnO based gas sensors. *Sensors and Actuators B: Chemical* 2008, *132* (1), 334-339.
4. Ahn, M.-W.; Park, K.-S.; Heo, J.-H.; Park, J.-G.; Kim, D.-W.; Choi, K. J.; Lee, J.-H.; Hong, S.-H., Gas sensing properties of defect-controlled ZnO-nanowire gas sensor. *Applied Physics Letters* 2008, *93* (26), 263103.
5. Navío, C.; Vallejos, S.; Stoycheva, T.; Llobet, E.; Correig, X.; Snyders, R.; Blackman, C.; Umek, P.; Ke, X.; Van Tendeloo, G.; Bittencourt, C., Gold clusters on WO3 nanoneedles grown via AACVD: XPS and TEM studies. *Materials Chemistry and Physics* 2012, *134* (2–3), 809-813.
6. Waclawik, E. R.; Chang, J.; Ponzoni, A.; Concina, I.; Zappa, D.; Comini, E.; Motta, N.; Faglia, G.; Sberveglieri, G., Functionalised zinc oxide nanowire gas sensors: Enhanced NO(2) gas sensor response by chemical modification of nanowire surfaces. *Beilstein Journal of Nanotechnology* 2012, *3*, 368-377.
7. Zheng, W.; Lu, X.; Wang, W.; Li, Z.; Zhang, H.; Wang, Z.; Xu, X.; Li, S.; Wang, C., Assembly of Pt nanoparticles on electrospun In2O3 nanofibers for H2S detection. *Journal of Colloid and Interface Science* 2009, *338* (2), 366-370.
8. Gurlo, A.; Ivanovskaya, M.; Bârsan, N.; Schweizer-Berberich, M.; Weimar, U.; Göpel, W.; Diéguez, A., Grain size control in nanocrystalline In2O3 semiconductor gas sensors. *Sensors and Actuators B: Chemical* 1997, *44* (1–3), 327-333.
9. Mu, X.; Chen, C.; Han, L.; Shao, B.; Wei, Y.; Liu, Q.; Zhu, P., Indium oxide octahedrons based on sol–gel process enhance room temperature gas sensing performance. *Journal of Alloys and Compounds* 2015, *637*, 55-61.

10. Bloor, L. G.; Manzi, J.; Binions, R.; Parkin, I. P.; Pugh, D.; Afonja, A.; Blackman, C. S.; Sathasivam, S.; Carmalt, C. J., Tantalum and Titanium doped In2O3 Thin Films by Aerosol-Assisted Chemical Vapor Deposition and their Gas Sensing Properties. *Chemistry of Materials* 2012, *24* (15), 2864-2871.
11. Yamazoe, N.; Sakai, G.; Shimanoe, K., Oxide Semiconductor Gas Sensors. *Catalysis Surveys from Asia* 2003, *7* (1), 63-75.
12. Pavelko, R. G.; Daly, H.; Hardacre, C.; Vasiliev, A. A.; Llobet, E., Interaction of water, hydrogen and their mixtures with SnO2 based materials: the role of surface hydroxyl groups in detection mechanisms. *Physical Chemistry Chemical Physics* 2010, *12* (11), 2639-2647.
13. Thiel, P. A.; Madey, T. E., The interaction of water with solid surfaces: Fundamental aspects. *Surface Science Reports* 1987, *7* (6), 211-385.
14. Stănoiu, A.; Simion, C. E.; Somăcescu, S., NO2 sensing mechanism of ZnO–Eu2O3 binary oxide under humid air conditions. *Sensors and Actuators B: Chemical* 2013, *186*, 687-694.
15. Annanouch, F. E.; Haddi, Z.; Ling, M.; Di Maggio, F.; Vallejos, S.; Vilic, T.; Zhu, Y.; Shujah, T.; Umek, P.; Bittencourt, C.; Blackman, C.; Llobet, E., Aerosol-Assisted CVD-Grown PdO Nanoparticle-Decorated Tungsten Oxide Nanoneedles Extremely Sensitive and Selective to Hydrogen. *ACS Applied Materials & Interfaces* 2016, *8* (16), 10413-10421.
16. Ma, N.; Suematsu, K.; Yuasa, M.; Shimanoe, K., Pd Size Effect on the Gas Sensing Properties of Pd-Loaded SnO2 in Humid Atmosphere. *ACS Applied Materials & Interfaces* 2015, *7* (28), 15618-15625.

CHAPTER 6

Operando Measurements

In this chapter we perform operand spectroscopy measurements in order to try to establish a hypothesis about the mechanisms of gas sensing. In-situ photoluminescence experiments have been performed over the ZnO and In_2O_3 samples and in-situ DRIFTS experiments have been performed over the commercial In_2O_3.

6.1 Photoluminescence over ZnO Nanowires

Regarding the photoluminescence spectra (PL spectra) of ZnO, there are different emission bands which are located in the ultraviolet and the visible (green, yellow and red/orange bands) regions. The first one is typically attributed to the characteristic emission of ZnO[1], whereas the visible part is normally attributed to a variety of donor defects such as oxygen vacancies, zinc interstitials and zinc vacancies[2].

In order to verify the results of the previous chapter regarding ZnO NW sensors, PL experiments were performed at room temperature (figure 6-1). Two different zones in the spectra can be clearly identified. The first one, which corresponds to the high peak located at the lower wavelength (around 380 nm), is associated to the near-band edge emission of the material. This strong emission corresponds to the recombination of electrons from the minimum of the conduction band with holes of the valence band of the semiconducting ZnO[3, 4]. Additionally, by zooming in the visible light region of the spectra (see the inset in figure 6-1), the presence of an emission band that ranges from 440 to nearly 820 nm is revealed, related to the large surface-to-volume ratio of the ZnO NWs. The exact origin of such a broad emission band has remained

controversial; nevertheless it has been generally attributed to defects and impurities referred to as a deep-level, trap-state or impurity-related radiative recombination process (such as oxygen vacancies, Zn interstitials, oxide antisite defect[5], and zinc vacancies). Therefore, the low intensity of this visible emission indicates the high crystalline quality of the different samples grown (i.e. NWs have a low density of defects).

The spectra also show a shift in the position of the maximum of the visible light emission. For the ZnO NWs grown over the c-plane the maximum is located at 550 nm (i.e., yellow luminescent band), while for those grown over a- and r- planes, the maximum is located near 520nm (i.e., green luminescent band).

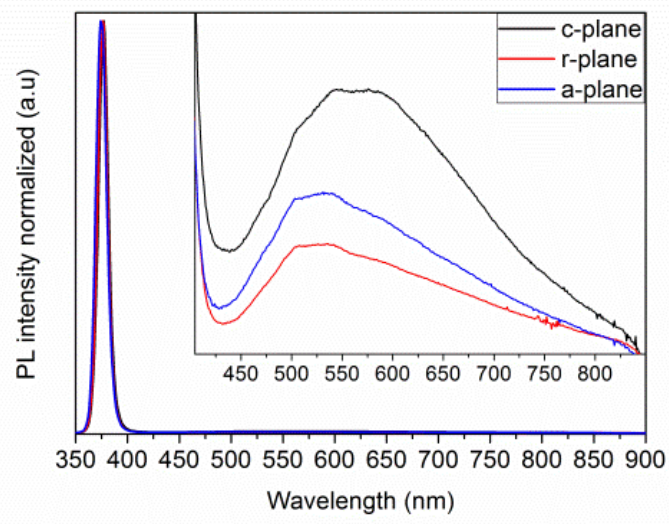

Figure 6-1: Room-temperature PL spectra of the three ZnO NW sample

Typically, defects responsible for the yellow luminescent band (YL) have been excess of oxygen and the presence of oxygen interstitials (Oi). Nevertheless, for the green luminescent band (GL), it has been reported to be

originated from oxygen vacancies (Vo). However, the presence of both GL and YL in the same samples suggests a common origin for them[6]. We will assume that the formation of such defects occurs during the growth process. Thereby, the initial Vo will form at the surface. Then, as Zn and O atoms are supplied, by adsorption, the ZnO layer will be created. By deposition of more atoms, the created defect will be overgrown and will become a Vo inside the lattice[7]. Consequently, if the orientation is different, the Vo will form from a different kind of surface.

If we correlate now the PL spectra to the gas response to NO_2, the c-plane sensor, i.e. the one that shows the highest response to NO_2, employs the material with the most intense visible emission band in its PL spectrum, centred at 550, which corresponds to the YL. This means that the sensor with the maximum number of oxygen interstitials is the most sensitive to NO_2. Sensor response to NO_2 can be explained as follows; NO_2 molecules adsorb on the material surface. Then, this adsorbed molecule acts as an acceptor according to the following reactions[8]:

$$NO_2(gas) \rightarrow NO_2(ads)$$
$$e^- + NO_2(ads) \rightarrow NO_2^-(ads)$$

Furthermore, the tilted morphology of ZnO NWs in the c-plane sensor favours the presence of many nanowire to nanowire junctions, the space charge regions of which are modulated upon NO_2 chemisorption. This further enhances the response towards nitrogen dioxide of the c-plane sensor as shown in figure 5-2(b).

However, this does not seem to be the case for EtOH sensing. Figure 5-2(a) shows that the most sensitive sensor for EtOH sensing is the a-plane sensor. In this particular case, as the maximum in the PL spectra corresponds to the GL, the origin for this visible band is related to oxygen vacancies. As mentioned above, oxygen vacancies are most likely responsible for the YL band. These vacant points would act as active sites in which oxygen will chemisorb during gas sensing[9]. The more numerous the active sites, the more oxygen will be chemisorbed and consequently, more molecules of target gas (EtOH in this case) will react and the sensor response will be dramatically affected.

This suggests that the engineering of defects in single crystalline metal oxides could be a viable approach to ameliorate selectivity.

In conclusion, for the detection of nitrogen dioxide, it was found that the response of ZnO NWs was directly correlated to the overall amount of defects. The higher the number of defects is (c-plane), the higher the response to nitrogen dioxide is. On the other hand, for the detection of ethanol, ZnO NWs with an intermediate number of defects (i.e. a-plane) in which surface defects were dominant led to the best results. These significant differences revealed by this study suggest that engineering the amount and nature of defects in metal oxide NWs deserves further research, since it may become an effective strategy for enhancing and tuning the selectivity of metal oxide sensors upon demands.

6.2 Photoluminescence over In_2O_3 Octahedra

In_2O_3 nanostructures show a strong photoluminescence (PL) emission in the visible range of the electromagnetic spectrum[10]. This broad emission located

mainly at around 580 nm is thought to be originated from different kind of defects present in the material. Among them, oxygen vacancies, oxygen interstitials, indium interstitials and oxygen antisite may be responsible for the broad emission observed by PL[11, 12]. These defects play a key role in the detection mechanism of semiconductor metal oxides. Therefore, PL studies can help to better understand the sensing mechanisms of indium oxide towards oxidizing and reducing agents.

In situ-PL experiments under air conditions have been performed on sensors employing pristine In_2O_3, Pt or Pd decorated In_2O_3 octahedra. PL spectra were obtained for sensors operated at 130ºC in a flow of dry air.

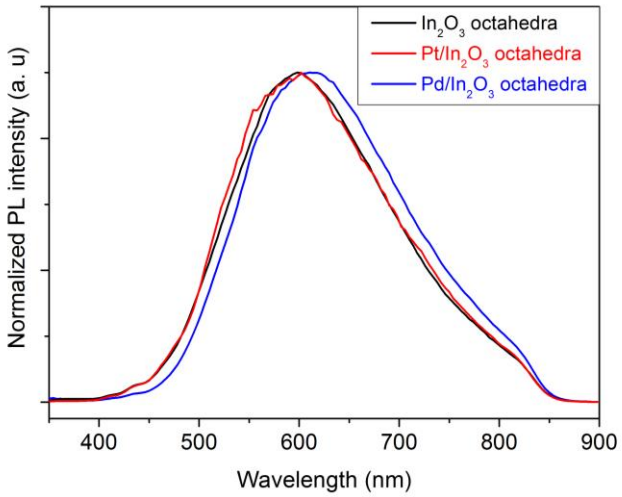

Figure 6-2: PL spectra of the three sensors under dry air conditions.

Figure 6-2 shows the normalized photoluminescence spectra of the different indium oxide sensors operated at 130ºC in dry air. As one can observe, for the pristine In_2O_3 and the Pt decorated In_2O_3 octaheda, there is a strong PL emission at 600 nm whereas for the Pd decorated In_2O_3 octahedra, the strong emission occurs at 610 nm. This indicates that a similar type of defects is

present in the three samples. Such orange emission band is thought to have its origin in deep In interstitials present in the nanomaterial[11].

Figure 6-3 shows the PL spectra for the different indium oxide sensors operated at 130ºC under the presence of 100 ppm of NO_2 in air. In this case, the strong PL emission is located at 600 nm for the three samples. This also suggests that the defects responsible for this emission are In interstitials.

As one can see, there is no significant difference between the normalized spectra under dry air shown in Fig. 8 and under NO_2 concentration. This implies that there is no change in the concentration of In interstitials on the nanomaterial upon the interaction with nitrogen dioxide. Also, the change in the number of oxygen vacancies caused by the presence of NO_2 does not substantially modify the PL.

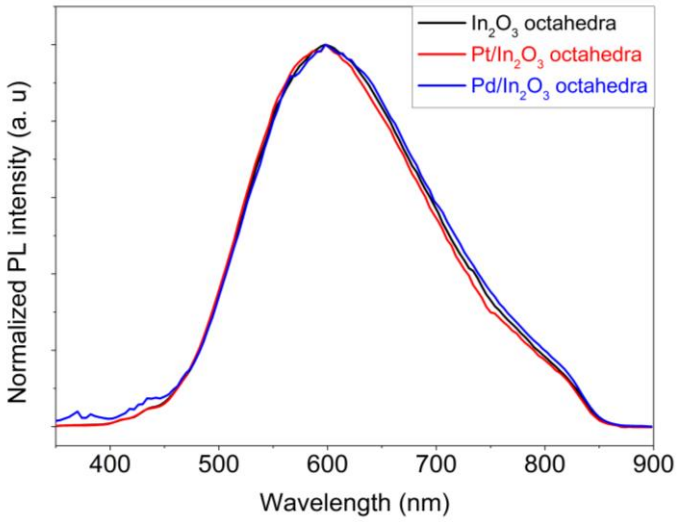

Figure 6-3: PL spectra of the sensors exposed to 100 ppm of NO_2

6.3 DRIFT spectroscopy on In_2O_3 material

In order to study in detail the sensing mechanism of the In_2O_3, a combination of empiric measurements and spectroscopic experiments, the so-called *operando* DRIFT spectroscopy can be used, which has been proven as an excellent technique to unravel the surface chemistry of several materials[13]. DRIFT spectroscopy possesses several advantages compared to other spectroscopic techniques: it is a non-destructive and fast method, since the sample is directly analyzed and it is suited for the analysis of materials that have a strong absorption, which generally results in a very low signal.

Until now, results on DRIFT spectroscopy for some semiconductor metal oxides such as SnO_2 towards reducing gases proposed a surface vacancy based reception model for the gas sensing with undoped SnO_2[14]. Additionally, some experiments have been carried out for WO_3[15] and Co_3O_4[15] towards NO and NO_2 gases that showed no clear differences in the oxidation state of the surfaces of these materials when exposed to NO or NO_2. However, to the best of our knowledge, nothing has been reported for DRIFT spectroscopy of In_2O_3 gas sensors exposed to oxidizing gases such as NO_2. As a result, making use of DRIFT spectroscopy will enable us to obtain more detailed information on the interaction of NO_2 with In_2O_3. Furthermore, a multivariate analysis which is suitable for large sets of complex spectroscopic data has been used in order to elucidate the spectral analysis by being able to detect subtle changes in the spectra. Particularly, Multivariate Curve Resolution (MCR) has been chosen for being a blind-source method, that is, there is no need for using a reference spectrum. MCR enables identifying the species involved in the detection

process and, furthermore, provides temporal information on the concentration profile of the different species present on the material surface.

Therefore, the aim of this work is to shed light, for the first time, in the sensing mechanism of In_2O_3 towards nitrogen dioxide (NO_2) at different temperatures. In order to do that, we have fabricated several In_2O_3 sensors via screen printing and we have performed simultaneously gas sensing experiments and *operando* DRIFT spectroscopy over the In_2O_3 sensors exposed to different concentrations of nitrogen dioxide and operated at different temperatures. By recording in parallel DRIFTS and standard response signals (resistance changes), one can correlate the change in the resistance with the creation of certain surface species. Upon exposure to nitrogen dioxide, several bands in the 4000-1000 cm^{-1} range appear or modify their intensity and this can be correlated to some specific surface species appearing or being modified. Having a better understanding of the surface chemistry involved during the response and recovery of indium oxide exposed to nitrogen dioxide has enabled us to introduce a more realistic sensing mechanism.

The sensors were produced as follows. First of all, commercial In_2O_3 (MaTeck 99.99%) powder was mixed with 1-2 propanediol and a printable ink was made. After that, such paste was printed onto an alumina substrate that contained a Pt electrode on one side and a Pt heater on the other side. The printed sensors were dried at 70ºC and annealed at 500ºC. A SEM image of the In_2O_3 material can be observed in figure 6-4.

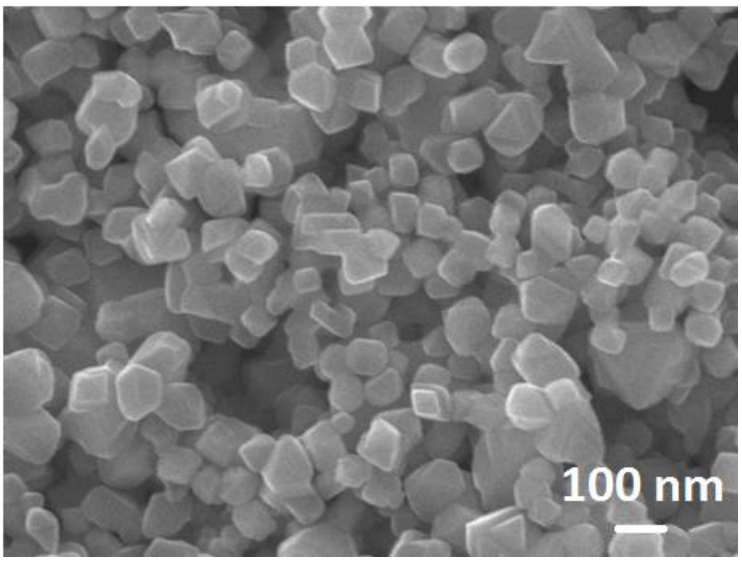

Figure 6-4: SEM image of the In_2O_3 deposited on the sensor

As observed in figure 6-4, the sensor is composed from small crystals whose size is about 100 nm.

Measurements (DRIFTS and electrical resistance) have been recorded at the same time over the In_2O_3 sensors. Always, the reference spectrum was recorded in dry air before any exposure to the gas. For the calculation of the absorbance spectra we have used:

$$absorbance = -log\left(\frac{single\ channel\ test\ gas}{single\ channel\ reference}\right)$$

6.3.1 Operando DRIFTS and sensing mechanism at 350ºC

First, we performed an *operando* DRIFTS study of the In_2O_3 sensor exposed to 1 ppm of NO_2 at 350 °C (Figure 6-5). The experiment consisted of three cycles of 3 h of NO_2 exposure followed by 6 h recovery in dry air. Figure 6-6(f) shows the electrical resistance of the In_2O_3 sensor under the periodic NO_2

exposure. Despite the relatively low response (ca. 1.28) as gas sensor, the electrical response was excellent with an outstanding signal-to-noise ratio. The time-resolved DRIFT spectra (2D plot) of the entire experiment (Figure 6-5) show the presence of the bands obviously responding to the NO_2 in the gas atmosphere (at ca. 1220, 1520 and 3630 cm^{-1}) and of those continuously growing (at ca. 1300 and 3630 cm^{-1}).

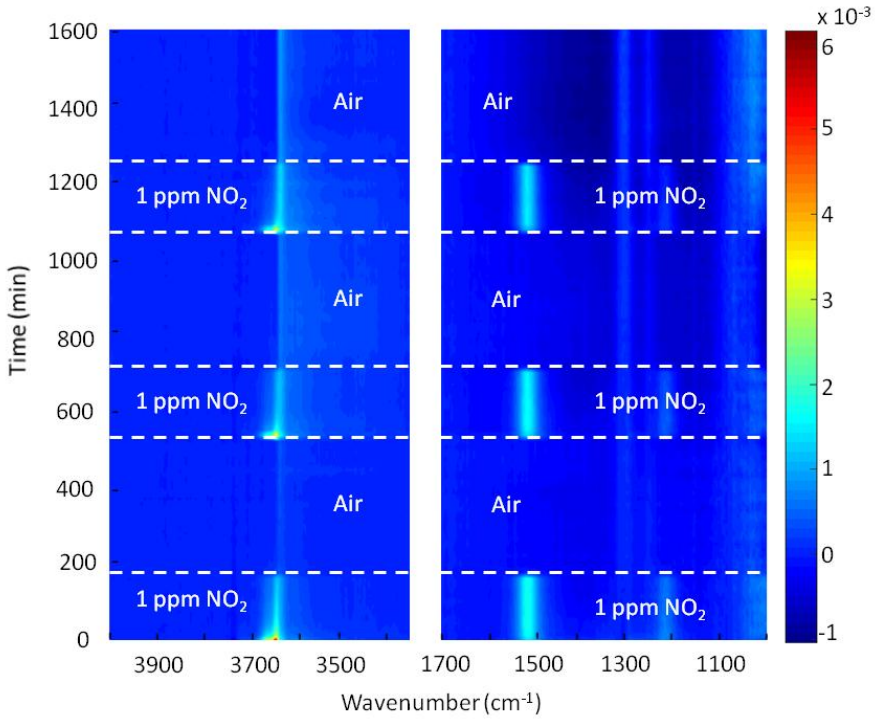

Figure 6-5: Time-resolved DRIFT spectra of the In_2O_3 gas sensor under alternating exposure to 1 ppm of NO_2 (3 h) and air (6 h) at 350 ºC. The scale is in the unit of absorbance and the spectra are shown taking the state of the sensor before the NO_2 exposure as the background.

These spectral changes clearly indicate that there are nitrites and/or nitrates and also hydroxyl groups on/near the In_2O_3 surface which are responding to NO_2. However, the common difficulty encountered in the analysis and interpretation is that the spectral features of some chemical species are overlapping, rendering them difficult or often impossible to correctly identify

them by the naked eye. Therefore, we have employed a multivariate analysis, particularly MCR, to disentangle the overlapping bands and to determine their concentration profiles based on the kinetic resolution of comprising bands[16].

The MCR analysis identified that the system comprises two surface chemical species (or states with multiple surface species) with varying concentrations under the NO_2 exposure and subsequent recovery phases. These chemical species are now called “components” and simply denoted as “C” with a label 1, 2, etc. (i.e. C1, C2 for 1000-2000 cm^{-1} and C1’ and C2’ for 2900-3800 cm^{-1}; the numbering has no meaning and there is no intended relation between CN and CN’ (N=1,2)).

Figures 6-6(a) and 6-6(b) present the *operando* DRIFT spectra of C1 and C2 and corresponding concentration profiles which are shown on the same time-scale as that of the gas sensing response (Figure 6-6(f)). It should be noted that MCR yielded the component spectra and concentration profiles directly from the time-resolved DRIFT spectra shown in Figure 6-5. Two prominent bands at 1221 and 1524 cm^{-1} were detected for C1, whereas for C2 clear bands were observed at ca. 1050, 1260 and 1313 cm^{-1}. Generally, asymmetric N-O stretching vibrations of nitrites and nitrates are reported to appear in the range of 1200-1500 cm^{-1}. Nitrates and nitrites adsorbed over various surfaces have been extensively studied and there is profound knowledge on their vibrational modes and frequencies. However, unfortunately, the assignments and observed frequencies are diverse; one can find almost any assignment one wishes to have in the literature. It has been reported that depending on the location of the nitrate ions, i.e. surface, sub-surface or bulk, the vibrational frequencies vary[17] and this factor besides potential intermolecular interactions among adsorbates

or with surface chemical groups (e.g. hydroxyl) may further complicate firm band assignments. For these reasons, herein we have attempted to assign the vibrational modes based mainly on the experimental observation and indications by quantum chemical calculations with minimal reference to available literature.

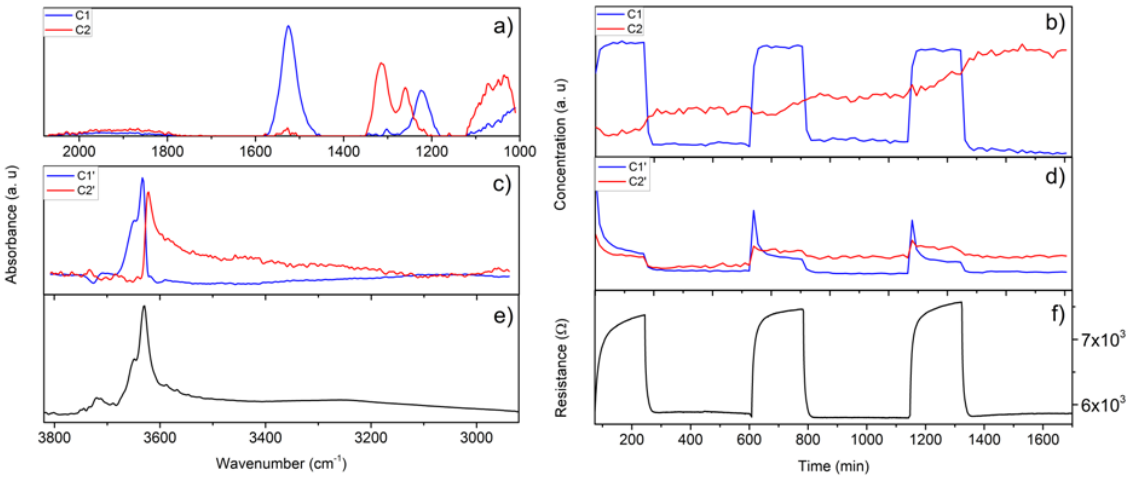

Figure 6-6: a) and c) Component spectra and b) and d) concentration profiles obtained after the MCR analysis of the time-resolved DRIFT spectra shown in Figure 1 for the In_2O_3 gas sensor exposed at 350 °C under periodic exposure to 1 ppm NO_2. e) Hydroxyl bands identified in the H_2O/D_2O exchange experiment (alternatingly passing 10% H_2O/D_2O vapour over the sensor). The spectrum is shown taking the sensor state in D_2O as the background. f) Response of the sensor towards 1 ppm of NO_2 gas at 350 ºC.

The main characteristic IR-active vibrations of isolated nitrate and nitrite ions are asymmetric stretching modes (Figure 6-7). Due to the symmetry of the ions, nitrate ion has the degenerate states for the vibrational mode at 1476 cm^{-1}, while nitrite ion has one state at 1374 cm^{-1} according to the quantum chemical calculation. In one literature, the frequencies of 1380 and 1260 cm^{-1} are reported for free nitrate and nitrite ions, respectively.[18] Despite the large difference in the numbers, it is consistent that the vibrational frequency of the stretching mode is about 100 cm^{-1} higher for nitrate. Based on this, it is

reasonable to conclude that the band at 1221 cm^{-1} of C1 is assigned to nitrite species and the two bands observed at 1260 and 1313 cm^{-1} of C2 are due to nitrate species with non-degenerated vibrational states because of a specific spatial orientation of the adsorbed ion on the surface. The prominent band at 1524 cm^{-1} could be assigned to nitrates or nitrites according to the literature[18] , but here we assign that the band is due to the surface hydroxyls directly interacting with nitrite species as discussed later.

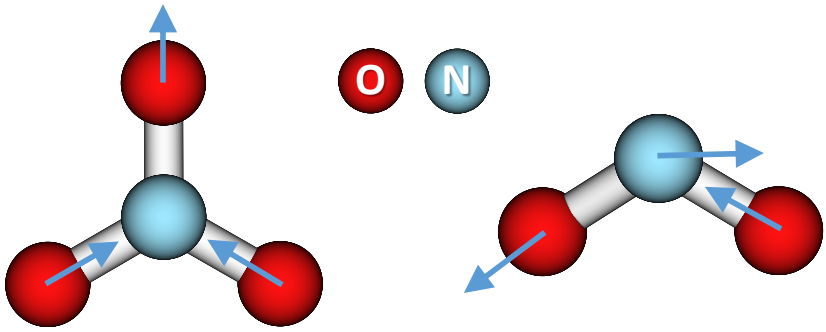

Unrestricted CCSD/aug-cc-pVTZ (without scaling)

1476 cm^{-1} (degenerate) **1374 cm^{-1}**

Figure 6-7: Asymmetric stretching modes and vibrational frequencies of nitrate (NO_3^-) and nitrite (NO_2^-) ions

The concentration profiles of C1 and C2 clarify important insights into the surface species involved during gas sensing. The concentration of C1, assigned to surface nitrite species, responds clearly and reversibly to the gaseous NO_2 concentration, matching well with the sensor response (Figure 6-6(f)). In contrast, the concentration of C2 responds irreversibly with a gradual, step-wise increase during the NO_2 pulse. These observations imply that the reversibly adsorbed surface nitrite species is responsible for the change in the resistance of the sensor, whereas nitrate species is formed gradually during the NO_2 pulse, likely due to slow oxidation of surface nitrites because of the low NO_2

concentration at 350 °C to form surface, sub-surface and bulk nitrates, which cannot be decomposed in air and, therefore, irreversibly accumulate over time.

Figures 6-6(c) and 6-6(d) show MCR-processed *operando* DRIFT spectra in the OH stretching region with two distinguishable hydroxyl species with distinct chemical nature (Figure 6-6(c)) with characteristic concentration profiles (Figure 6-6(d)). Generally, a presence of isolated hydroxyl groups is indicated by the sharp bands appearing in the 3500-3700 cm^{-1} while the presence of the bridging hydroxyls, via hydrogen-bonds, is clarified by the broad bands appearing in 2900-3500 cm^{-1}. The component spectra and concentration profiles of C1' and C2' show that when the In_2O_3 gas sensor becomes in contact with NO_2, at first there is a sharp rise in the population of C1', i.e. the terminal OH band located at higher frequency at 3632 cm^{-1} with a shoulder band at 3648 cm^{-1}. Subsequently the concentration of the species sharply drops and reaches a steady concentration (Figure 6-6(d), C1'). The other hydroxyl species (C2') possesses a prominent band at 3621 cm^{-1} with a broad band feature (appearing as a tail) down to 3000 cm^{-1}, which was absent for C1'. This indicates that in C2' an interaction of OH group with another molecular/structural entity in various configurations like hydrogen-bonds is present. Also, the concentration profile of C2' is very different from that of C1', exhibiting increase in the concentration upon the NO_2 pulse with an irreversible profile, i.e. accumulative increase over the multiple NO_2 pulses. It should be noted that the hydroxyl bands presented in Figure 6-6(c) is relative (difference spectra) compared to the initial state of In_2O_3 before the exposure to NO_2 pulses. Hence, the positive values in the concentration spectra indicate that the hydroxyl bands were newly formed and/or that their absorbance has been enhanced due to NO_2 interaction with the

In_2O_3 surface. With the diffuse reflection sampling configuration, it is not trivial to quantitatively discuss the amount of hydroxyl groups present initially, formed and interacting at the surface. In this study, the type of hydroxyl groups present at 350 °C in air was identified by exchanging the hydroxyl group from OH to OD. Figure 6-6(e) shows the IR spectrum of OH groups which could be exchanged to OD groups (and vice versa) by alternatingly passing 10% H_2O and D_2O vapour over the cell. The DRIFT spectrum shows that the hydroxyl groups responding to NO_2 pulses (C1' and C2') are already present without NO_2 pulses, mostly as isolated hydroxyls. This suggests that the changes are due to an increase in the absorption cross section of the hydroxyl groups, rather than to the formation of new hydroxyl groups upon NO_2 surface adsorption.

Assuming the constant concentration of surface hydroxyl groups during NO_2 sensing, we can suggest the roles of hydroxyls and surface chemical processes taking place as follows. Firstly, when NO_2 adsorbs over In_2O_3, terminal hydroxyl (C1') interacts with adsorbed NO_2 forming nitrite species (C1) and senses its presence (based on this the prominent band at 1524 cm^{-1} has been assigned to nitrites interacting with hydroxyls, *vide supra*). Subsequently a transformation of surface configuration of adsorbed NO_2 takes place as indicated by the decrease of C1', most likely by the formation of (subsurface or bulk) nitrate species by the oxidation of adsorbed nitrites as strongly suggested by the increase of C2 (nitrates) in the middle of NO_2 pulses (Figure 6-6(b), C2). The concentration of the hydroxyls present in multi-configurations with possible hydrogen-bonds (C2') seem influenced by that of the nitrate species as indicated by irreversible, step-wise increase of the concentration of C2' over NO_2 pulses at the expense of lowered initial peak height of C1' concentration (Figure 6-6(d)).

6.3.2 Operando DRIFTS and sensing mechanism at 130ºC

Importantly, the response of the In_2O_3 sensor against 1 ppm NO_2 is about 450 times higher at 130 °C than at 350 °C. Aiming at elucidating the origin of the high sensitivity, we have investigated the roles of surface species during NO_2 sensing by means of *operando* DRIFTS in combination with MCR. At 130 °C, MCR analysis found three components in both nitrite/nitrate and hydroxyl regions (Figures 6-7(a-d)). For this experiment, first cycle was a 7 h exposure to 1 ppm NO_2 followed by recovery in air for 12 h. The following two cycles were with 1 h NO_2 pulse and 2 h recovery in dry air. Similarly to Figure 6-6, the gas sensing response during the measurements and the DRIFT spectrum of exchangeable hydroxyl groups obtained by the H_2O/D_2O experiment at 130 °C are presented in Figures 6-7(f) and 6-7(e), respectively.

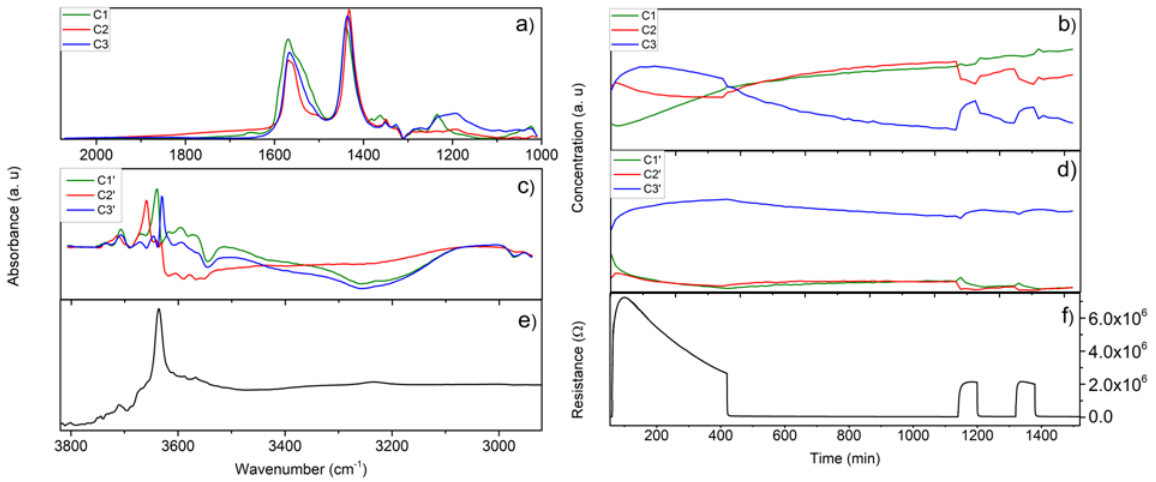

Figure 6-8: a) and c) Component spectra and b) and d) concentration profiles obtained after the MCR analysis of the time-resolved DRIFT spectra shown in Figure AII-1 (Annex II) for the In_2O_3 gas sensor exposed at 130 °C under periodic exposure to 1 ppm NO_2. e) Hydroxyl bands identified in the H_2O/D_2O exchange experiment (alternatingly passing 10% H_2O/D_2O vapour over the sensor). The spectrum is shown taking the sensor state in D_2O as the background. f) Response of the sensor towards 1 ppm of NO_2 gas at 130 ºC.

The broad band feature below 3500 cm^{-1} observed in Figure 6-8(e) clearly shows the presence of a significantly higher number of hydroxyls on the sample at 130 °C than 350 °C, interacting with other species, likely via hydrogen-bonding.

Notably, the spectral features of the obtained components in both regions at 130 °C were very different from those observed at 350 °C. Compared to the component spectra at 350 °C (Figure 6-6(a)), there were two new prominent bands at ca. 1430 and 1560 cm^{-1}, which were present for all three components. These bands arise from the interaction of surface hydroxyls and particularly adsorbed water with adsorbed NO_2 in a specific configuration as discussed further below. A careful look into the nitrite/nitrate spectral region allows categorizing the three component spectra into two families. The first family is C1 (Figure 6-8(a)) which shows a band at 1223 cm^{-1} and also a shoulder band at ca. 1530 cm^{-1}. These band positions are obviously identical to that formerly assigned to nitrites interacting with surface isolated hydroxyls (Figure 6-6(a), C1; Figure AII-1, Annex II). The species responsible for C1 increases gradually with time, more pronouncedly during the NO_2 pulse. The second family includes C2 and C3 where a very broad band at ca. 1200 cm^{-1} was observed. A noticeable difference between C2 and C3 is the higher absorbance of the band at ca. 1200 cm^{-1} and the broader feature of the band at ca. 1560 cm^{-1} for C3. The profile of C3 concentration is most closely matching with the response of the gas sensor. Interestingly, the concentration profiles of C2 and C3 are behaving oppositely and counter-acting (Figure 6-8(b)), which implies that there is a transition of the chemical states between C2 and C3 during the NO_2 pulse and recovery phase.

The characteristic frequency region of hydroxyls provides also unique insights into the chemistry during NO_2 sensing process at 130 °C (Figures 6-7(c) and 6-7(d)). In this region the identified three components can also be categorized into two families; ones with the strong hydrogen-bonding features (C1' and C3') and one without (C2'). These components show distinctly different isolated OH stretching frequencies in 3600-3700 cm^{-1}. The first family (C1' and C3') shows similar, largely negative bands in 3100-3550 cm^{-1} with a characteristic isolated hydroxyl at 3546 cm^{-1} with a broad band centered at ca. 3250 cm^{-1} characteristic of hydrogen-bonds. C1' and C3' mainly differs in the terminal hydroxyl stretching frequency at 3640 cm^{-1} for C1' and 3629 cm^{-1} for C3'. The concentration profiles of the components (Figure 6-8(d)) show that the concentration of C3' is dominating, but the degree of concentration change for C1' and C3' is on a similar level and the profiles are behaving in a counteracting manner. Closely looking at the period of NO_2 pulse, first the concentration of C1' then that of C3' increase. In practice, this means that the terminal hydroxyl band characteristic of C1' appears and then red-shifts to the frequency of C3' and by MCR this band shift is described by two components with distinct, varying concentrations.

On the other hand, the spectrum of C2' is markedly different without the feature of hydrogen-bonds but with the band of terminal hydroxyls with the high stretching frequency at 3658 cm^{-1}. According to the concentration profile of C2' (Figure 6-8(d)), C2' increases gradually during the recovery phase in dry air. This can be reasonably understood that the terminal hydroxyls of the In_2O_3 surface become more freely available during the recovery and they are highly isolated without strongly interacting species nearby, as implied by the high

vibrational frequency (i.e. less dragging interaction of the OH stretching mode) and the absence of hydrogen-bonds. In contrast, as discussed above, the water-like spectral features with isolated and hydrogen-bonded features are present for C1' and C3' and they appear as negative bands. This is a proof that the hydroxyl groups, most likely due to surface adsorbed water, are "consumed" when NO_2 adsorbs on the surface (thus appear negatively with respect to the initial state before the exposure to NO_2) in a way that the hydrogen-bonds are broken or rather that the IR absorption by the hydrogen-bonds is weakened. This also accompanies freeing the hydroxyls on the In_2O_3 surface as evident from the positive bands at ca. 3600-3700 cm^{-1}. This process takes a while to reach a stabilized state as suggested by the continuously changing sensor response for 7 h (Figure 6-8(f)). Based on these observations and interpretations, it can be concluded that C2 in the nitrite/nitrate region (Figure 6-8(a)) interacts with adsorbed NO_2 and reversibly forms C3, enhancing the bands at ca. 1200 and at ca. 1550 cm^{-1} (C2 vs. C3 in Figure 6-8(a)) ascribed to nitrites interacting with surface water and hydroxyls. The broad features of the two bands also indicate the highly flexible configuration of the surface nitrite and support the view of dissolved-in-water-like interaction of nitrites on the In_2O_3 surface. The surface hydroxyls of In_2O_3 seems also sensing the presence of adsorbed NO_2 as indicated by the red/blue shifts of the bands (C1' vs. C3').

Regarding the irreversible change and thus the deactivation of the gas sensor, 130 °C is too low for the oxidation of nitrite to nitrates to take place as in the case at 350 °C. However, there is another cause of deactivation at such low operating temperature. The gradual increase in C1 (Figures 6-7(a) and 6-7(b)) with two prominent features at 1223 and 1530 cm^{-1} was confirmed, indicating

the formation of nitrites irreversibly increasing in concentration and interacting with surface hydroxyls of In_2O_3. Although a similar chemical process was reversibly taking place at 350 °C (C1, Figures 6-6(a) and 6-6(b)), the desorption process is likely too slow at 130 °C and the nitrite cannot be desorbed during the recovery phase. This means that this NO_2 adsorption mode is mainly responsible for the changes in the electrical response at 350 °C, but at 130 °C the same mode is responsible for deactivation. This is well plausible because the magnitude of the electrical response is markedly different at the two temperatures and the factor responsible for resistance change at high temperature may cause poor response at low temperature. Further investigation at an intermediate temperature (250 °C) confirms that the behaviour of gas sensors and surface species lie between the two temperatures, supporting the temperature dependent sensing mechanisms suggested above (Figures AII-2 and AII-3, Annex II).

The facts that the absorbance of the bands in the nitrites/nitrates region is one order of magnitude higher at 130 °C (Figure AII-1, Annex II) than at 350 °C (Figure 6-5) and that the hydrogen-bonded hydroxyl groups are consumed when the sensor is exposed to NO_2 at 130 °C suggest the important roles of hydroxyl groups and water on the surface of In_2O_3 in the sensing mechanism via facilitated NO_2 adsorption. This view is also supported by the experimental observation where the presence of water vapour indeed improved the response of an In_2O_3 sensor at different concentrations of NO_2 at 130 °C.

6.4 References

1. Smith, J.; Akbari-Sharbaf, A.; Ward, M. J.; Murphy, M. W.; Fanchini, G.; Kong Sham, T., Luminescence properties of defects in nanocrystalline ZnO. *Journal of Applied Physics* 2013, *113* (9), 093104.
2. Zeng, H.; Duan, G.; Li, Y.; Yang, S.; Xu, X.; Cai, W., Blue Luminescence of ZnO Nanoparticles Based on Non-Equilibrium Processes: Defect Origins and Emission Controls. *Advanced Functional Materials* 2010, *20* (4), 561-572.
3. Reparaz, J. S.; Güell, F.; Wagner, M. R.; Hoffmann, A.; Cornet, A.; Morante, J. R., Size-dependent recombination dynamics in ZnO nanowires. *Applied Physics Letters* 2010, *96* (5), -.
4. Aad, R.; Simic, V.; Le Cunff, L.; Rocha, L.; Sallet, V.; Sartel, C.; Lusson, A.; Couteau, C.; Lerondel, G., ZnO nanowires as effective luminescent sensing materials for nitroaromatic derivatives. *Nanoscale* 2013, *5* (19), 9176-9180.
5. Lin, B.; Fu, Z.; Jia, Y., Green luminescent center in undoped zinc oxide films deposited on silicon substrates. *Applied Physics Letters* 2001, *79* (7), 943-945.
6. Marin, O.; Grinblat, G.; Gennaro, A. M.; Tirado, M.; Koropecki, R. R.; Comedi, D., On the origin of white photoluminescence from ZnO nanocones/porous silicon heterostructures at room temperature. *Superlattices and Microstructures* 2015, *79* (0), 29-37.
7. Subannajui, K.; Wongchoosuk, C.; Ramgir, N.; Wang, C.; Yang, Y.; Hartel, A.; Cimalla, V.; Zacharias, M., Photoluminescent and gas-sensing properties of ZnO nanowires prepared by an ionic liquid assisted vapor transfer approach. *Journal of Applied Physics* 2012, *112* (3), 034311.
8. Öztürk, S.; Kılınç, N.; Öztürk, Z. Z., Fabrication of ZnO nanorods for NO2 sensor applications: Effect of dimensions and electrode position. *Journal of Alloys and Compounds* 2013, *581*, 196-201.
9. Pati, S.; Majumder, S. B.; Banerji, P., Role of oxygen vacancy in optical and gas sensing characteristics of ZnO thin films. *Journal of Alloys and Compounds* 2012, *541* (0), 376-379.
10. Jean, S.-T.; Her, Y.-C., Growth Mechanism and Photoluminescence Properties of In2O3 Nanotowers. *Crystal Growth & Design* 2010, *10* (5), 2104-2110.
11. Kumar, M.; Singh, V. N.; Singh, F.; Lakshmi, K. V.; Mehta, B. R.; Singh, J. P., On the origin of photoluminescence in indium oxide octahedron structures. *Applied Physics Letters* 2008, *92* (17), 171907.
12. Yadav, K.; Mehta, B. R.; Singh, J. P., Presence of metal-oxide interface enhanced photoluminescence from In-In2O3 core-shell nanorods. *RSC Advances* 2015, *5* (2), 1581-1586.
13. Grossmann, K.; Pavelko, R. G.; Barsan, N.; Weimar, U., Interplay of H2, water vapor and oxygenat the surface of SnO2 based gas sensors – An operando investigation utilizing deuterated gases. *Sensors and Actuators B: Chemical* 2012, *166–167*, 787-793.

14. Degler, D.; Wicker, S.; Weimar, U.; Barsan, N., Identifying the Active Oxygen Species in SnO2 Based Gas Sensing Materials: An Operando IR Spectrsocopy Study. *The Journal of Physical Chemistry C* 2015, *119* (21), 11792-11799.
15. Akamatsu, T.; Itoh, T.; Izu, N.; Shin, W., NO and NO2 Sensing Properties of WO3 and Co3O4 Based Gas Sensors. *Sensors* 2013, *13* (9), 12467.
16. Jaumot, J.; Gargallo, R.; de Juan, A.; Tauler, R., A graphical user-friendly interface for MCR-ALS: a new tool for multivariate curve resolution in MATLAB. *Chemometrics and Intelligent Laboratory Systems* 2005, *76* (1), 101-110.
17. Hesske, H.; Urakawa, A.; VandeVondele, J.; Baiker, A., Insight into Fundamental, Overtone, and Combination IR Bands of Surface and Bulk Ba(NO3)2 by Ab Initio Molecular Dynamics. *The Journal of Physical Chemistry C* 2010, *114* (35), 15042-15048.
18. Hadjiivanov, K. I., Identification of Neutral and Charged N x O y Surface Species by IR Spectroscopy. *Catalysis Reviews* 2000, *42* (1-2), 71-144.

CHAPTER 7

Conclusions and Outlook

In this thesis, two types of semiconductor metal-oxide materials such as ZnO nanowires and In_2O_3 octahedra have been studied.

7.1 ZnO Nanowires

For ZnO nanowires it has been shown that the morphology and orientation of ZnO NWs, CVD-grown on sapphire substrates are highly dependent on the crystalline plane of the substrate. By employing room-temperature PL studies, it has been possible to establish that the crystalline plane of the substrate has also an impact in the number of defects and in the nature of these (i.e., defects located at the surface or deep-levels within the ZnO NWs). Sensors have been fabricated and tested employing ZnO NWs with different orientations. For the detection of nitrogen dioxide, it was found that the response of ZnO NWs was directly correlated to the overall amount of defects. The higher the number of defects is (c-plane), the higher the response to nitrogen dioxide is. On the other hand, for the detection of ethanol, ZnO NWs with an intermediate number of defects (i.e., a-plane) in which surface defects were dominant led to the best results. These significant differences revealed by this study suggest that engineering the amount and nature of defects in metal oxide NWs deserves further research, since it may become an effective strategy for enhancing and tuning the selectivity of metal oxide sensors upon demands.

7.2 In_2O_3 Octahedra

We have developed a facile method to synthesize highly crystalline In_2O_3 octahedra at high temperatures, whose face size is around 500 nm.

Furthermore, an easy way to decorate such nanostructures with noble metal nanoparticles has been shown. XPS measurements have shown that the metal nanoparticles have a core-shell structure which the core of the particle corresponds to the metal and the shell corresponds to the oxidized metal.

Additionally, we can say that pure In_2O_3 octahedra are excellent for detecting NO_2 gas with an outstanding sensitivity (0.43 ppb^{-1}) at low temperatures (130ºC), while the response to H_2 remains two orders of magnitude lower under the same conditions. In addition, the presence of humidity increases the sensitivity to NO_2 and, at the same time, reduces the response to H_2, which results in an increased selectivity. This makes our sensor an excellent candidate to detect, in a selective way, oxidizing gases such as NO_2 at low operating temperatures, even showing potential for room temperature operation, with an excellent sensitivity even in the presence of humidity.

Furthermore, increasing the operating temperature and loading the octahedra with Pt, results in the quenching of the response to NO_2 and in an increase in the response towards H_2. In this way, one can make the sensor more selective to reducing gases such as H_2. However, in this case the presence of ambient humidity negatively influences the response of the sensor.

As a consequence, our nanomaterial can be made selective to oxidizing or reducing gases by varying the operating temperature and by metal loading.

These significant differences revealed by this study suggest that engineering the morphology and the crystallinity of the material can be really useful and deserve further research, since it may become an effective strategy for enhancing the sensitivity and selectivity of In_2O_3 sensors.

7.3 *Operando* DRIFT Spectroscopic Measurements

By means of *operando* DRIFTS, we have elucidated the surface species responsible for NO_2 sensing using In_2O_3 material at different temperatures where gas-sensing characteristics remarkably alter. It has been shown that the actual sensing mechanism is more complicated than previously reported and, importantly, that distinct sensing mechanisms are active depending on the temperature of sensor.

At all temperatures, the electrical response originates from NO_2 sorption processes, although the NO_2 adsorption and thus sensing mechanisms differ due to the characteristic chemical nature of the In_2O_3 surface, especially of hydroxyls and adsorbed water, at different temperatures. At high temperature (350 °C), isolated hydroxyl groups sense the NO_2 adsorption and directly interact with adsorbed NO_2, inducing changes in electrical response. This NO_2 sorption process is reversible at 350 °C. At the same time, oxidation of surface nitrites to nitrates takes place at 350 °C and this can lead to deactivation of the surface for NO_2 sorption.

In contrast, at low temperature (130 °C), the gas sensing mechanism involves surface hydroxyls with and without hydrogen-bonds present over the In_2O_3 surface. This “wet” surface is obviously beneficial to adsorb larger amount of NO_2 and thus responsible for higher sensitivity in NO_2 sensing at the temperature. Interestingly, at 130 °C deactivation of the sensor surface is caused by the mechanism of the active gas sensing at 350 °C, i.e. surface nitrite formation and interaction with the isolated OH group of In_2O_3. This surface nitrate irreversibly increases in concentration, but the electrical

response due to this NO_2 adsorption is too low to impact on the overall response which is dominated by the "wet" NO_2 adsorption mechanism.

7.4 Future Work

However, lately, some authors have reported gas sensing using ultraviolet (UV) activated metal oxides as an efficient way to increase sensitivity and lower power consumption. These works employ UV light as an energy efficient alternative to heating for activating chemical reactions occurring at the surface of the metal oxide during the gas detection. This approach can cut power consumption in metal oxides and help re-considering the suitability of these materials for integrating wireless sensors.

UV light has often been used exclusively for promoting desorption of surface species from the sensing layer, rather than to modify its sensing properties. It is only recently that UV activation in addition to heating has been explored for improving sensitivity and selectivity for metal oxides.

As a result, further experiments have been carried out making use of UV irradiation in order to try to enhance the sensitivity and lowering power consumption of a resistive nitrogen dioxide sensor employing semiconducting In_2O_3 octahedra as a sensing nanomaterial.

Prior to employ UV activation for the detection of NO_2, the effect of a sudden irradiation of the oxide material with UV light was investigated. The evolution of the sensor resistance was monitored when a UV diode was switched on. When the UV LED is switched on, there is a significant drop in the resistance. This resistance change tails off over many hours indicating that sudden exposure to

UV light results in the triggering of changes in the nanomaterial that have slow dynamics. This decrease can be explained by several mechanisms:

- Electrons in the valence band of In_2O_3 absorb energy from the UV light to jump to the conduction band. Such transitions decrease the resistance of an n-type semiconductor film.
- UV light has been reported to act as a cleaner of the surface of the oxide by promoting desorption of adsorbed species. This will result in the lowering of the amount of oxygen and/or NO_2 adsorbates. Since In_2O_3 is an *n*-type semiconductor, desorption of oxidizing species from its surface translates into an increase of the free charge carriers and thus, a decrease in the DC resistance.
- Furthermore, the partial removal of oxygen adsorbates may trigger the diffusion of bulk oxygen towards the surface, especially when the UV irradiated metal oxide sensor is operated at temperatures well above room temperature.

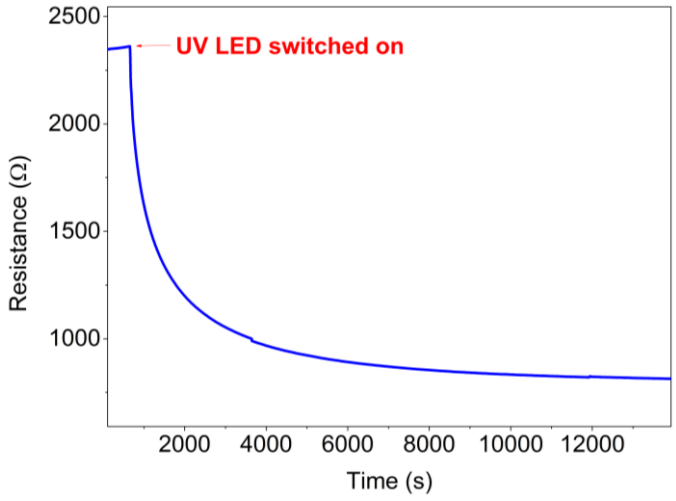

Figure 7-1: Resistance change of an In_2O_3 sensor suddenly exposed to UV light. The heating element of the sensor is not used in this test.

Afterwards, In_2O_3 octahedra have been exposed to several concentrations of NO_2 gas at room temperature with the UV LED switched on as shown on figure 7-2.

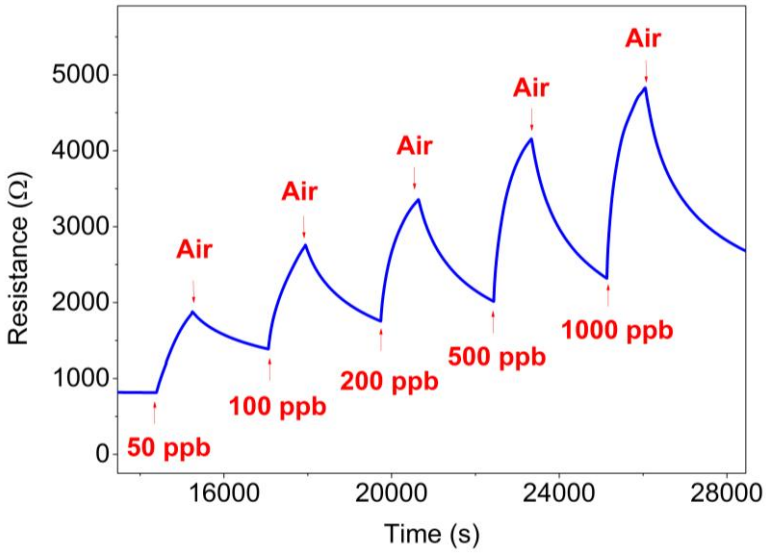

Figure 7-2: Response and recovery cycles of an In_2O_3 octahedra sensor exposed to different concentrations of nitrogen dioxide under constant UV light. The heating element of the sensor is not used in this test. The duration of exposure and recovery cycles was set to 15 and 30 minutes, respectively.

As shown in figure 7-2 and table 7-1, the response of the sensor to NO2 is smaller and the response and recovery dynamics are slower than when the sensor is operated at 130ºC without UV irradiation. As a matter of fact, the response and recovery times are not enough for the response and the baseline to fully recover. This can be explained as follows. UV light helps desorbing ionosorbed species from the surface of In_2O_3 octahedra. Therefore, during the cleaning phases in which the sensor is flushed with dry air, UV light helps desorbing NO_2 adsorbates, reducing In_2O_3 and decreasing the resistance of the sensor. The equilibrium concentration of NO_2 adsorbates depends on the

ambient concentration of NO_2, which results in increasing sensor resistance values for increasing concentration of this pollutant gas.

Table 7-1: Comparison of sensor response intensity, response and recovery times for an In_2O_3 octahedra sensor under two different operating conditions

	Response to 500 ppb of NO_2 (R_{NO2}/R_{air})	Response Time (min)	Recovery Time (min)
Sensor operated at 130ºC (UV diode off)	47	4.5	5.3
Sensor operated under constant UV light, heating element off	1.8	≈15	>30

Nevertheless, from the results presented in table 7-1, it can be derived that operating the sensor at 130ºC is more favourable than operating it under constant UV light irradiation for detecting NO_2.

Additionally, the effect of UV irradiation on senor response can be further studied under a dynamic operation mode. In this case, during the response and recovery cycles, the UV diode is periodically switched on and off by employing a square driving current signal while the sensor is operated at a constant temperature. Both in the presence of NO_2 and pure air the sensor resistance increases while the UV LED is off and decreases while the UV LED is on. This, results in the overall sensor response presenting a ripple that appears because UV light reduces the material which tends to re-oxidize when the UV light is off. The dynamics of UV pulsed operation can be studied by computing the

evolution of reduction and oxidation rates. For instance, the instantaneous reduction rate can be computed as the local derivative of the resistance response curve during a semi-period in which the UV diode is switched on. Similarly, the instantaneous oxidation rate can be the local derivative of the response curve during a semi-period in which the diode is switched off. In this way, and combining pulsed UV irradiation and thermal heating of the sensor one can try to improve the sensitivity of the In_2O_3 octahedra sensor towards NO_2 gas with the possibility of making significant savings in the power consumption in comparison to standard heated operation. However, while it is true that the integration of gas sensors with UV LEDs would increase overall cost, it could be a fraction of those incurred when producing a standard MOX sensor, provided that UV-activated sensors were produced in big numbers. This could be the case if such sensors were to integrate widespread personal or indoor air monitors.

Annex I

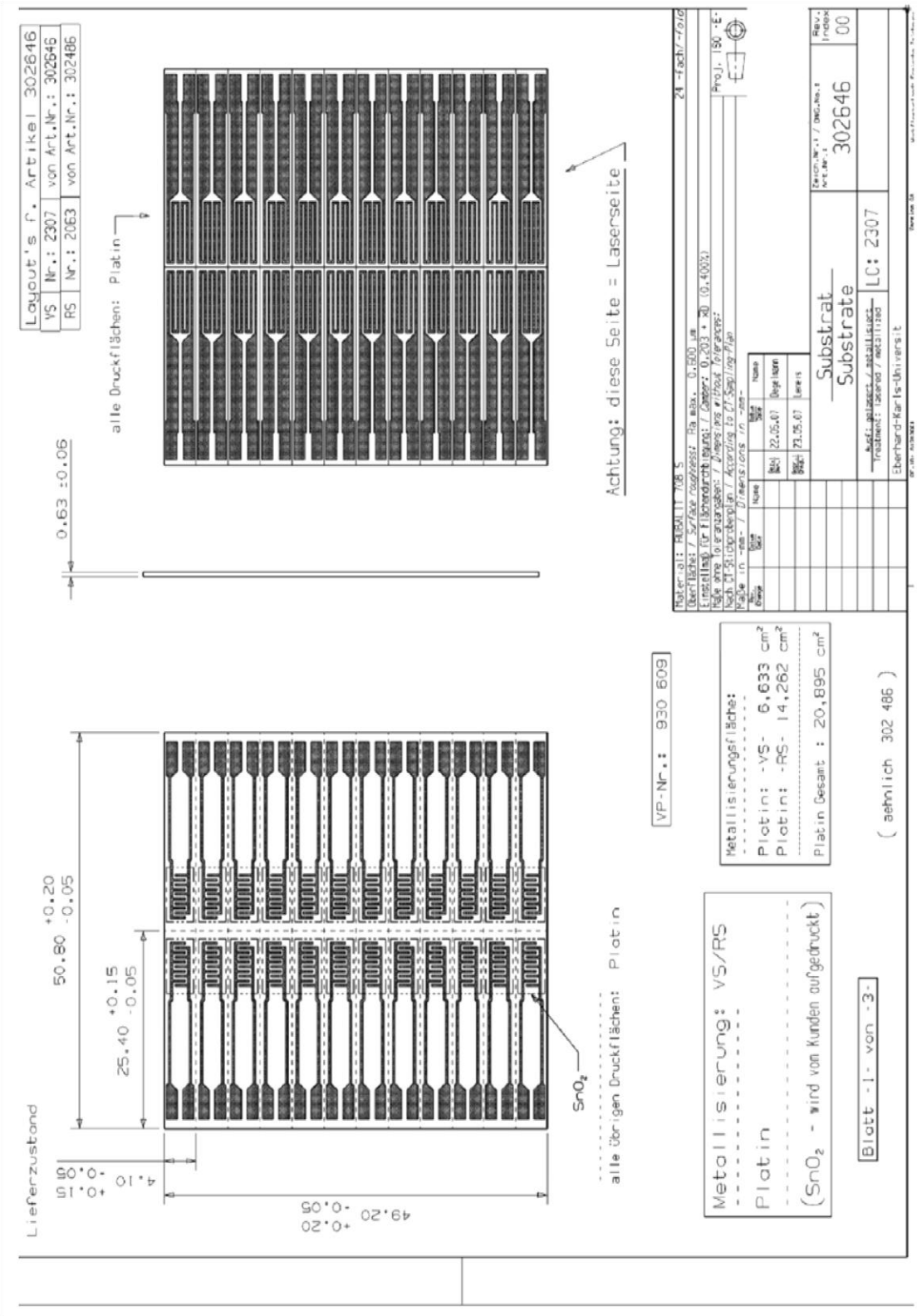
Layout's f. Artikel 302646
VS Nr.: 2307 von Art.Nr.: 302646
RS Nr.: 2063 von Art.Nr.: 302486
alle Druckflächen: Platin
0.63 ±0.06
Achtung: diese Seite = Laserseite
24 -fach/-fold
Substrat
Substrate
LC: 2307
302646
00
VP-Nr.: 930 609
Metallisierungsfläche:
Platin: -VS- 6,633 cm²
Platin: -RS- 14,262 cm²
Platin Gesamt : 20,895 cm²
Metallisierung: VS/RS
Platin
(SnO2 - wird von Kunden aufgedruckt)
(ähnlich 302 486)
Blatt -1- von -3-
Lieferzustand
50.80 +0.20 -0.05
25.40 +0.15 -0.05
4.10 +0.15 -0.05
49.20 +0.20 -0.05
SnO2
alle übrigen Druckflächen: Platin

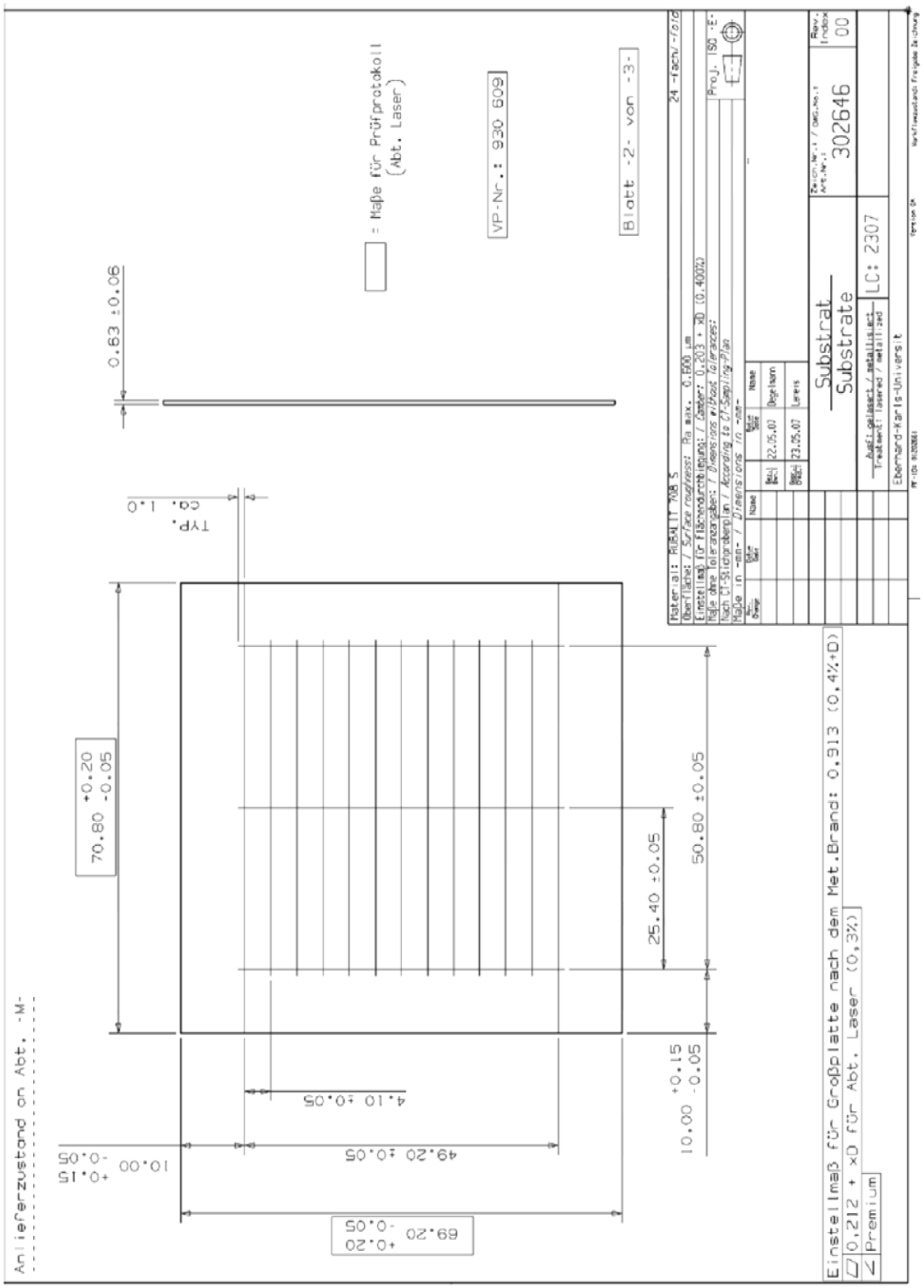
Substrat
Substrate
302646
00
LC: 2307
Ebernand-Karls-Universität
Material: ROBALIT 708 S
Einstellmaß für Großplatte nach dem Met.Brand: 0,913 (0,4%+D)
0,212 + xD für Abt. Laser (0,3%)
Premium
Anlieferzustand on Abt. -M-
= Maße für Prüfprotokoll (Abt. Laser)
VP-Nr.: 930 609
Blatt -2- von -3-
0.63 ±0.06
TYP. ca. 1.0
70.80 +0.20 -0.05
50.80 ±0.05
25.40 ±0.05
10.00 +0.15 -0.05
4.10 ±0.05
49.20 ±0.05
69.20 +0.20 -0.05

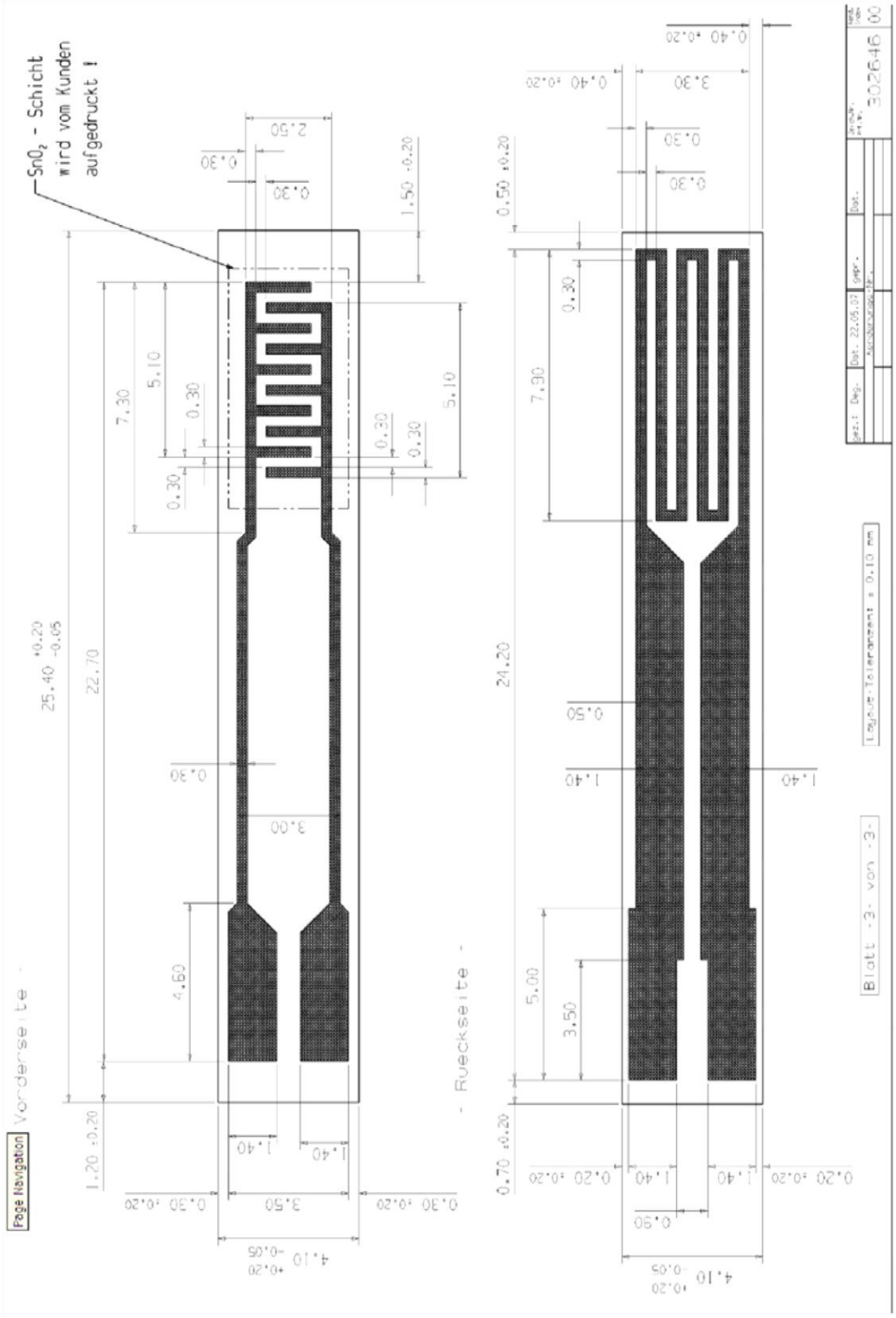
SnO2 - Schicht
wird vom Kunden
aufgedruckt !
Page Navigation
Vorderseite
- Rueckseite -
Blatt -3- von -3-
302646

Annex II

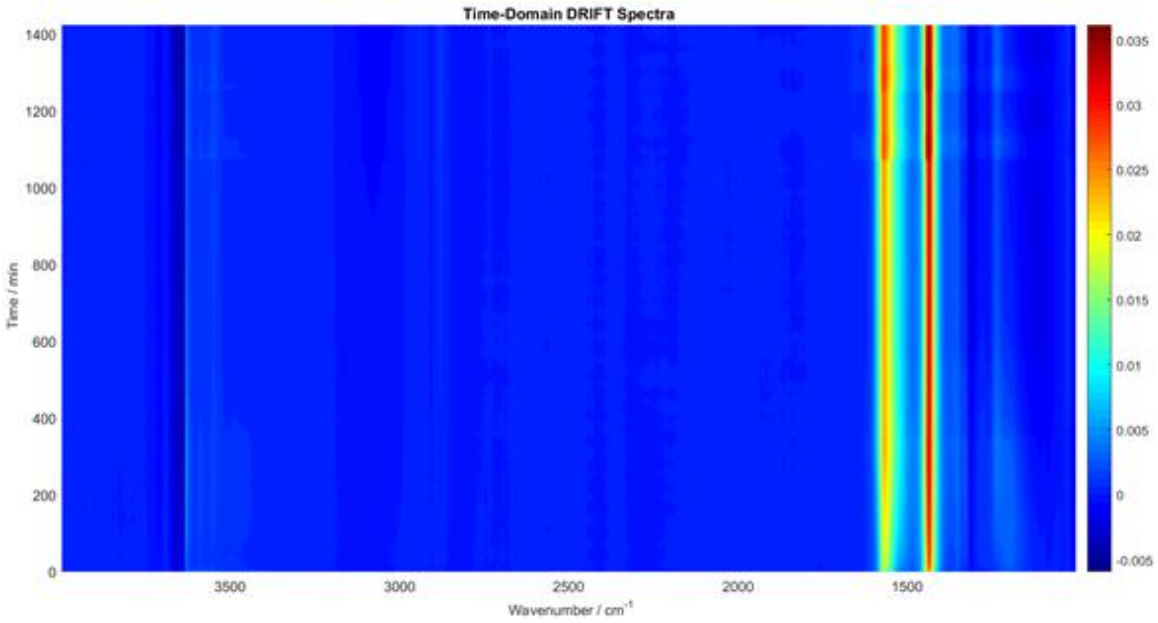

Figure AII- 1: Time-domain DRIFT spectra of exposure to several cycles of 1 ppm of NO_2 at 130ºC

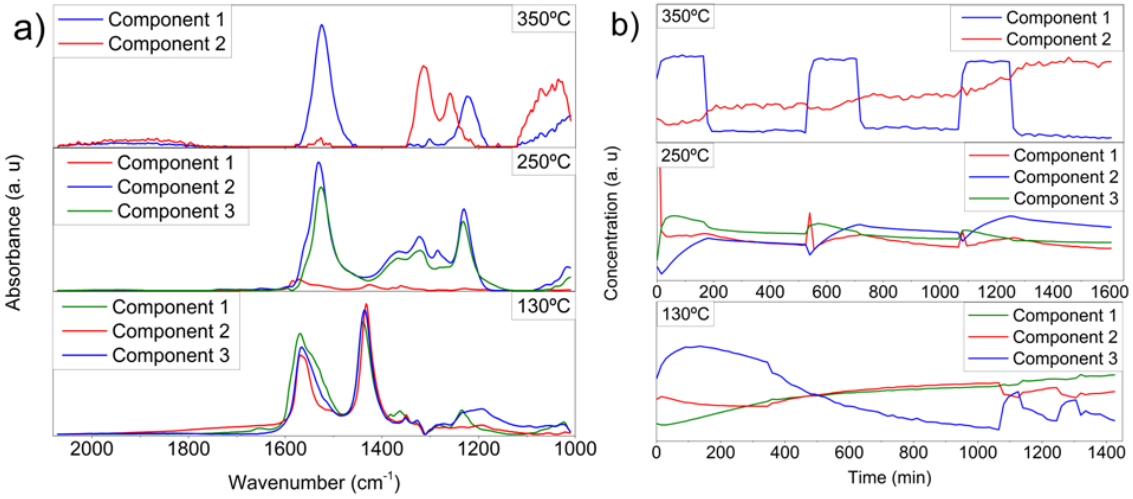

Figure AII- 2: MCR absorbance and concentration spectra of the nitrite/nitrate region of the DRIFT spectra for the three temperatures

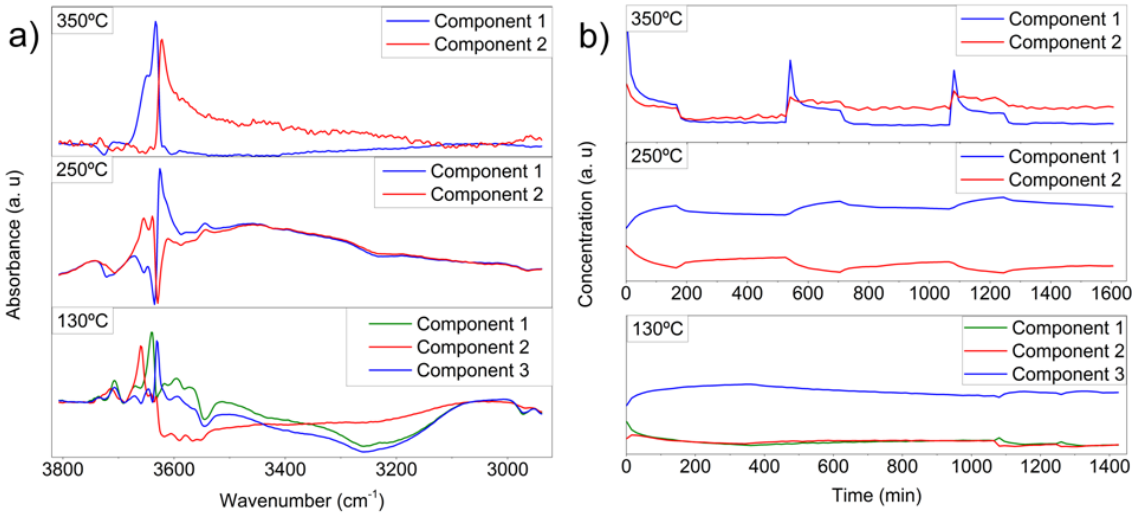

Figure AII- 3: MCR absorbance and concentration spectra of the OH region of the DRIFT spectra for the three temperatures

Publications in International Journals

- *"Synthesis of ZnO nanowires and impacts of their orientation and defects on their gas sensing properties"*
  Sergio Roso, Frank Güell, Paulina R. Martínez-Alanis, Atsushi Urakawa, Eduard Llobet.
  Sensors and Actuators B 230 (2016) 109-114

- *"Plasma versus thermal annealing for the Au-catalyst growth of ZnO nanocones and nanowires on Al-doped ZnO buffer layers"*
  Frank Güell, Paulina R. Martínez-Alanis, Sergio Roso, Carlos I. Salas-Pérez, Mario F. García-Sánchez, Guillermo Santana, B Marel Monroy
  Materials Research Express 3 (2016) 065013

- *"Synthesis of Single Crystalline In_2O_3 Octahedra for the Selective Detection of NO_2 and H_2 at Trace Levles"*
  Sergio Roso, Carla Bittencourt, Polona Umek, Oriol González, Frank Güell, Atsushi Urakawa, Eduard Llobet.
  Journal of Materials Chemistry C, 2016, Advance Article

- "*p-Type PdO nanoparticles supported on n-type WO_3 nanoneedles for hydrogen sensing*"
  F. E. Annanouch, S. Roso, Z. Haddi, P. Umek, C. Bittencourt, C. Blackman, T. Vilic, E. Llobet
  Thin Solid Films 618 (2016) 238-245

- "*Enhanced detection of nitrogen dioxide via combined heating and pulsed UV operation of indium oxide nano-octahedra*"
  Oriol González, Sergio Roso, Xavier Vilanova, Eduard Llobet
  Beilstein Journal of Nanotechnology 2016, 7 1507-1518

- "*Operando DRIFTS study of indium oxide gas sensors*"

  Sergio Roso, David Degler, Eduard Llobet, Nicolae Barsan, Atsushi Urakawa

  Manuscript in progress

Contribution in Conferences and Seminars

- International Meeting on Chemical Sensors 2014, (16th March-19th March), Buenos Aires (Argentina)
    - Oral Contribution: *Hydrogen Sensing Properties of ZnO and WO3 nanowires*

      Sergio Roso, Fatima Ezahra Annanouch, Frank Güell, Stella Vallejos, Atsushi Urakawa, Eduard Llobet

- E-MRS 2014 Spring Meeting 2014, (26th May-30th May) Lille (France)
    - Poster Presentation: *Gas Sensing Properties of ZnO Nanowires Grown via the Vapor-Liquid-Solid Method over Sapphire Substrates*

      Sergio Roso, Frank Güell, Eduard Llobet

- Gas sensors based on semiconducting metal oxides: basic understanding & application fields (GSSMO) 2015 (7th June-9th June) Tübingen (Germany)
    - Oral Contribution: *Synthesis of In_2O_3 octahedra for detection of very-low concentrations of oxidizing and reducing gases*

      Sergio Roso, Atsushi Urakawa, Eduard Llobet

- Eurosensors 2015 (6th September-9th September) Freiburg (Germany)
    - Poster Presentation: *NO_2 sensing properties of thermally or UV activated In_2O_3 nano-octahedra*

      Oriol González, Sergio Roso, Eduard Lobet, Xavier Vilanova

- IBERNAM 2015 (10th-11th December) Zaragoza (Spain)
  - Poster Presentation: Synthesis of single crystalline In_2O_3 octahedra for detecting oxidizing and reducing gases at trace levels
    Sergio Roso, Atsushi Urakawa and Eduard Llobet

- IX International Workshop on Semiconductor Gas Sensors (SGS) 2015 (13th December-16th December) Zakopane (Poland)
  - Oral Presentation: *Synthesis of single crystalline In_2O_3 octahedra for detecting oxidizing and reducing gases at trace levels*
    Sergio Roso, Atsushi Urakawa, Eduard Llobet

- Eurosensors 2016 (4th September-7th September) Budapest (Hungary)
  - Poster Presentation: *Gas sensing properties of In_2O_3 cubes prepared by a hydrothermal method*
    Sergio Roso, Toni Vilic, Atsushi Urakawa, Eduard Llobet

UNIVERSITAT ROVIRA I VIRGILI
SYNTHESIS AND GAS SENSING PROPERTIES OF SINGLE CRYSTALLINE METAL-OXIDE NANOSTRUCTURES
Sergio Roso Casares

UNIVERSITAT ROVIRA I VIRGILI
SYNTHESIS AND GAS SENSING PROPERTIES OF SINGLE CRYSTALLINE METAL-OXIDE NANOSTRUCTURES
Sergio Roso Casares

UNIVERSITAT ROVIRA I VIRGILI
SYNTHESIS AND GAS SENSING PROPERTIES OF SINGLE CRYSTALLINE METAL-OXIDE NANOSTRUCTURES
Sergio Roso Casares

UNIVERSITAT
ROVIRA i VIRGILI

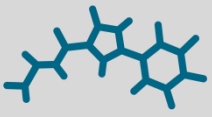

ICIQ

Institut
Català
d'Investigació
Química